PROGRESSIVE ALTERATIONS IN MICROSTRUCTURAL ORGANIZATION AND BIOMECHANICAL RESPONSE IN THE APOE MOUSE MODEL OF ANEURYSM AND THE UNDERLYING CHANGES IN BIOCHEMISTRY

by

Darren Haskett

A Dissertation Submitted to the Faculty of the

GRADUATE INTERDISCIPLINARY PROGRAM IN BIOMEDICAL ENGINEERING

In Partial Fulfillment of the Requirements

For the Degree of

DOCTOR OF PHILOSOPHY

In the Graduate College

THE UNIVERSITY OF ARIZONA

2015

THE UNIVERSITY OF ARIZONA
GRADUATE COLLEGE

As members of the Dissertation Committee, we certify that we have read the dissertation prepared by Darren Haskett, titled Progressive Alterations in Microstructural Organization and Biomechanical Response in the ApoE Mouse Model of Aneurysm and the Underlying Changes in Biochemistry and recommend that it be accepted as fulfilling the dissertation requirement for the Degree of Doctor of Philosophy.

_____ Date: (06/29/2015)
Jonathan Vande Geest

_____ Date: (06/29/2015)
Urs Utzinger

_____ Date: (06/29/2015)
Dominic McGrath

_____ Date: (06/29/2015)
Julia Indick

Final approval and acceptance of this dissertation is contingent upon the candidate's submission of the final copies of the dissertation to the Graduate College.

I hereby certify that I have read this dissertation prepared under my direction and recommend that it be accepted as fulfilling the dissertation requirement.

_____ Date: (06/29/2015)
Dissertation Director: Jonathan P Vande Geest

STATEMENT BY AUTHOR

This dissertation has been submitted in partial fulfillment of requirements for an advanced degree at the University of Arizona and is deposited in the University Library to be made available to borrowers under rules of the Library.

Brief quotations from this dissertation are allowable without special permission, provided that accurate acknowledgment of source is made. Requests for permission for extended quotation from or reproduction of this manuscript in whole or in part may be granted by the head of the major department or the Dean of the Graduate College when in his or her judgment the proposed use of the material is in the interests of scholarship. In all other instances, however, permission must be obtained from the author.

SIGNED: __Darren Haskett_____

ACKNOWLEDGEMENTS

I would like to thank my advisor Jonathan Vande Geest for all of his help and motivation he has offered me throughout my studies here. Without him taking a chance and believing in me I would not be where I am today. I would also like to thank my doctoral committee for their help both professionally and personally, and all the past and present members of the Soft Tissue Biomechanics Laboratory.

TABLE OF CONTENTS

LIST OF TABLES AND FIGURES

TABLES

FIGURES

ABSTRACT

Abdominal Aortic Aneurysm (AAA) is a complex disease that leads to a localized dilation of the infrarenal aorta that develops over years. Longitudinal information in humans has been difficult to obtain for this disease, therefore mouse models have become increasingly used to study the development of AAAs. The objective of this study was to determine any changes that occur in the biomechanical response and fiber microstructure in the apolipoprotein E difficient ($ApoE^{-/-}$) angiotensin II (AngII) infused mouse model of aneurysm during disease progression, as well as determine some of the underlying changes in biochemistry, and demonstrate a novel method of reducing any pathogenic protease activity. Using a Microbiaxial Opto-Mechanical Device (MOD), ex vivo studies included adult aortas of $ApoE^{-/-}$ AngII infused mice excised and tested for mechanical response simultaneously imaged using two-photon microscopy to assess the microstructure at multiple time points. *In vitro* and *ex vivo* studies have shown changes in protease concentrations with the use of FRET based proteolytic beacons able to provide a non-destructive method to quantify protease activity measured against mechanical and microstructural changes. *In vitro* studies have demonstrated protease activity can be reduced using a molecule providing a positive feedback mechanism for protease inhibition and possibly provide a reduction in aneurysm progression.

CHAPTER 1: LONGITUDINAL DEVELOPMENT OF ANEURYSM AND THE ROLE OF MATRIX METALOPROTEASES AND METHODS FOR TREATMENT

1.1. Introduction

Abdominal aortic aneurysms (AAAs) are a local weakening and dilation of the infrarenal aorta [1, 2]. Continued growth of AAA without treatment can lead to rupture, an event that has a reported mortality rate as high as 90% [3-5]. Once diagnosed, smaller AAAs (typically < 5.5cm in diameter) are monitored prospectively until the risk of rupture outweighs the morbidity/mortality risks associated with either open surgical repair (OSR) or endovascular repair (EVAR). There are estimated to be 2 million people in the United States with AAA, and somewhere between 6,000 to 10,000 deaths occur each year due to AAA rupture [3, 4, 6-8]. The rate of AAA diagnosis is also expected to increase over the next several decades due to the aging of the population [3]. In 2000, the total per patient hospital costs for EVAR and OSR were estimated to be $21,250 and $12,342, respectively [9]. Even if the 40,000 estimated total annual AAA repairs were entirely OSRs, the conservative estimate of total hospital costs for repair of AAA in the United states would be 45,000 x $12,342 = $555M/yr. These costs do not include the ongoing surveillance costs for patients with small AAA. Thus, there is an increasing need to study the initiation and progression of AAA as these aspects of the disease are still poorly understood, as well as to develop new pharmaceutical treatments for patients with AAA and potentially reduce US health care costs significantly.

Much of the difficulty in studying AAA initiation and progression is that the formation of AAA is a complex and multifactorial disease that develops over years. Also, data on AAA samples is often limited to a single time point when it can be collected during an elective OSR at which point the tissue has been severely remodeled greatly altering the biomechanics and biochemistry. Additionally, with the increased improvement and use of EVAR, even the availability of tissue from OSR is on the decline making mechanistic studies on the pathogenesis of AAA even more difficult.

Due to the inherent difficulty in studying human AAA, animal models have taken a prominent role in how the disease is studied. The number of animal models for aneurysm is quite large and can be broken down between large and small animal models. Large animal models often rely on autologous grafts in order to generate saccular regions within the aorta to mimic AAA. However, these methods do not follow the true initiation and progression of the disease and their usefulness in study is consigned to the development of novel treatment options and the determine efficacy of new stents grafts. Small animal models on the other hand, especially those that rely on genetic predisposition, do offer the chance to study in depth both the mechanobiology and biochemistry as aneurysms initiate and progress.

1.2. The ApoE Mouse Model of Aneurysm

Recently the apolipoprotein E deficient ($ApoE^{-/-}$) angiotensin II (AngII) infused mouse model has come to the forefront in the study of AAA. It has proven to be an excellent test bed as it displays many of the same histological and biological characteristics as native human AAA such as atherosclerotic plaque formation, medial degeneration, thrombus formation, and an increase in matrix-metalloproteinase (MMP) activity [10-13].

In the AngII infused $ApoE^{-/-}$ model changes in aortic physiology were observed nearly immediately. Within 1 to 4 days after initiation of AngII infusion, medial accumulation of macrophages occurred in areas where aneurysms are known to develop [14]. Disruption of elastin fibers was also frequently observed at sites of macrophage accumulation, however it is unknown whether elastin degradation is the event that leads to macrophage accumulation or whether macrophage accumulation leads to degradation of elastin [11].

The 4-10 days following AngII infusion found vascular hematomas in the majority of $ApoE^{-/-}$ mice and aortic dissections contained from rupture by the adventitia; during this time period 10% of mice died [11, 14]. Deaths during this period were found to be caused by AAA rupture with subsequent exsanguinations into the abdominal cavity.

For those mice that survived the disruption of elastic lamina and medial dissection, formation of thrombus occurred and was thought to be a strong stimulus for inflammation [11]. After thrombus development, macrophages were found accumulated in areas near the thrombus in both intact and disrupted media and were even found within the thrombus. During this time period, remodeling of the aortic tissue began in the aneurismal arterial segments. This is one of the few animal models that describe macrophage infiltration into the thrombotic clot which is characteristic of human AAA [2].

Beyond 14 days of AngII infusion, aneurismal tissue was found to mature with increased deposition of extracellular matrix and inclusion of T and B lymphocytes, however, disruption of medial elastin fibers was still present even after 14 days of AngII infusion. By 28 days of AngII infusion, the aorta had completely re-endothelialized over the areas of medial disruption, and neovascularization occurred throughout the aneurismal tissue. Remodeling in this manner could then lead to a permanently enlarged aorta with all three arterial layers [11]. Only after 28 days of AngII infusion were atherosclerotic lesions observed in regions of aneurismal development [14]. Finally, Daugherty et al. [15] have also reported thoracic aortic aneurysms in AngII infused ApoE$^{-/-}$ mice (**Figure 1.1**). This has broadened the utility of chemically-induced genetic mouse models to investigate the pathogenic mechanisms of both AAA and thoracic aortic aneurysms.

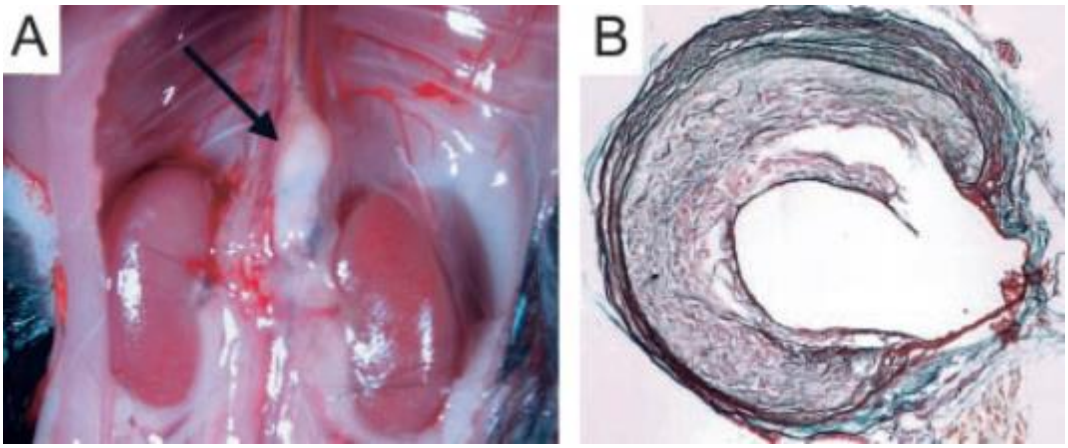

Figure 1.1: Development of AAA in ApoE$^{-/-}$ mice. Tile A demonstrates the presence of an AAA in the suprarenal region of the aorta of an aged ApoE$^{-/-}$ mouse. Tile B shows a cross-section stained with Gomori trichrome strain for muscle tissue demonstrating the dilation of the aorta and the thrombus formation in ApoE$^{-/-}$ mice that mimics human disease – Figure taken from Daugherty and Cassis, 2004 [12].

1.3. Studies into the Role of MMPs in Aneurysm

MMPs were first discovered in 1962, and through the 1960s and 1970s were found to be associated in many human diseases [16, 17]. Since then more than 20 different MMPs have been identified in humans (**Table 1.1**). Although MMPs are essential for human and other multicellular life, dysregulation of MMPs plays a central role in disease including tumor growth, vascularization and metastasis, rheumatoid arthritis, pulmonary disease, and many forms of cardiovascular disease. In the case of AAA, in both the human disease and in animal models, studies have shown several MMPs to be upregulated including MMP 2, 9, and 14 – which are of interest in this study [18].

The common structural component that all MMPs contain is a metal ion (typically zinc) in the active site of the enzyme that is able to react and hydrolyze a peptide bond often specific to the individual MMP. MMPs are found in two different forms, that of the inactive and active form. Initially synthesized in the inactive form, the pro-MMP contains a cysteine switch connected to the C-terminus of the protease that interacts with the zinc ion of the active site and must be removed before the MMP can bind to its respective substrate.

Gene:	Type	Location	Substrates	Citations
MMP1	Collagenase	Secreted	-Substrates include Col I, II, III, VII, VIII, X, gelatin. -Breaks down interstitial collagens I, II, and III.	[19-22]
MMP2	Gelatinase	Secreted	-Substrates include Gelatin, Col I, II, III, IV, Vii, X	[23-25]

MMP3	Stromelysin	secreted	-Substrates include Col II, IV, IX, X, XI, gelatin -Degrades collagen types II, III, IV, IX, and X, proteoglycans, fibronectin, laminin, and elastin. -Activates other MMPs such as MMP-1, MMP-7, and MMP-9	[26-28]
MMP7	Matrilysin	secreted	- fibronectin, laminin, Col IV, gelatin -Mediated by transformation growth factor β (TGF-β).TGF-β stimulates ECM and suppresses the steady-state level of MMP7, stromelysin mRNAs, and secretion of zymogens.	[29-31]
MMP8	Collagenase	secreted	-Substrates include Col I, II, III, VII, VIII, X, aggrecan, gelatin	[32-34]
MMP9	Gelatinase	secreted	-Substrates include Gelatin, Col IV, V -Degrades type IV and V collagens and other extracellular matrix proteins.	[35-37]
MMP10	Stromelysin	secreted	- Col IV, laminin, fibronectin, elastin - Degrades proteoglycans and fibronectin. The gene is part of a cluster of MMP genes which localize to chromosome 11q22.3	[38-42]
MMP11	Stromelysin	secreted	- Col IV, fibronectin, laminin, aggrecan - Cleaves alpha 1-proteinase inhibitor but weakly degrades structural proteins of the extracellular matrix	[43-45]
MMP12	Metalloelastase	secreted	-Elastin, fibronectin, Col IV -The enzyme degrades soluble and insoluble elastin.	[41, 46, 47]
MMP13	Collagenase	secreted	-Substrates include Col I, II, III, IV, IX, X, XIV, gelatin -Expressed in the skeleton as required for restructuring the collagen matrix for bone mineralization.	[41, 48, 49]

MMP14	Membrane-Type MMP	membrane	-Type-I transmembrane MMP; substrates include gelatin, fibronectin, laminin -Activates MMP2 protein, and this activity may be involved in tumor invasion.	[50-54]
MMP15	Membrane-Type MMP	membrane	-Type-I transmembrane MMP; substrates include gelatin, fibronectin, laminin	[50, 55, 56]
MMP16	Membrane-Type MMP	membrane	-Type-I transmembrane MMP; substrates include gelatin, fibronectin, laminin -Both forms of the protein activate MMP2 by cleavage. This gene was once referred to as MT-MMP2, but was renamed as MT-MMP3 or MMP16.	[55, 57]
MMP17	Membrane-Type MMP	membrane	-Glycosyl phosphatidylinositol-attached; substrates include fibrinogen, fibrin -The protein activates MMP2 by cleavage.	[58-60]
MMP18	Not Designated	-	No known human orthologue	[55, 58, 61]
MMP19	“Other”	-	-It has a role in cellular proliferation, migration, angiogenesis and adhesion.	[62-65]
MMP20	Enamelysin	secreted	-Appears to be the only MMP that is tooth-specific and it is expressed by cells of different developmental origin (i.e. epithelial ameloblasts and mesenchymal odontoblasts).	[55, 66, 67]
MMP21	“Other”	secreted	-The encoded protein may play an important role in embryogenesis, particularly in neuronal cells, as well as in lymphocyte development and survival.	[68-71]
MMP23A	“Other”	membrane	-Type-II transmembrane cysteine array	[72-74]
MMP23B	“Other”	membrane	-Type-II transmembrane cysteine array	[72-75]

MMP24	Membrane-Type MMP	membrane	-Type-I transmembrane MMP -This protein activates MMP2 by cleavage.	[76-78]
MMP25	Membrane-Type MMP	membrane	-In response to bacterial infection or inflammation, the encoded protein is thought to inactivate alpha-1 proteinase inhibitor, a major tissue protectant against proteolytic enzymes released by activated neutrophils, facilitating the transendothelial migration of neutrophils to inflammatory sites. -The encoded protein may also play a role in tumor invasion and metastasis through activation of MMP2.	[60, 79-81]
MMP26		-	-The encoded protein degrades type IV collagen, fibronectin, fibrinogen, casein, vitronectin, alpha 1-antitrypsin (A1AT), alpha 2-macroglobulin (A2M), and insulin-like growth factor-binding protein 1 (IGFBP), and activates MMP9 by cleavage.	[82-85]
MMP27	"Other"	-	- It has been demonstrated that MMP-27 is an unusual protease that is not secreted and is efficiently retained in the endoplasmic reticulum in three mammaliancell lines.	[86-88]
MMP28	Epilysin	secreted	-Unlike other MMPs this enzyme is constitutively expressed in many tissues (Highly expressed in testis and at lower levels in lung, heart, brain, colon, intestine, placenta, salivary glands, uterus, skin). A threonine replaces proline in its cysteine switch (PRCGVTD).	[83, 89-91]

Table 1.1 List of known MMPs, types, location, substrates (if known), and citations.

1.4 Methods for Reducing Protease Activity

The discovery that aneurysm development was associated with increased local MMP production in aneurismal tissue [46, 92-95], and that MMPs were potentially the

cause of extracellular matrix degradation has initiated research into compounds able to suppress MMP activity. Specifically MMP-2, -9, and -12 have been found associated with human AAA disease [7, 96]. The family of antibiotics known as tetracyclines is known to be inhibitory of MMPs when used at levels lower than antimicrobial doses [97-100]. One tetracycline in particular, doxycycline, has been found to be a non-selective inhibitor of MMPs through either a transcriptional or direct method [13], and is readily available.

The first animal models of AAA to incorporate doxycycline in order to suppress aneurysm formation used elastase-induced aortic injury in the rat [101, 102]. Petrinec et al. found that doxycycline did have an aneurysm-suppressing effect *in vivo* with a dosage of 25 mg/day administered via drinking water [101]. Curci et al. also found doxycycline inhibited aortic dilation was most likely dose dependent with effects starting at 6 mg/kg/day and maximal effects at 30 mg/kg/day again administered via drinking water [102]. Mouse models of AAA that also utilize doxcycline in aneurismal suppression include Manning et al., Pyo et al., and Vihn et al. [103-105]. While Manning et al. again used elastase infusion; both Pyo et al. and Vihn et al. used AngII infused *ApoE*$^{-/-}$ mice. All used a dosage of 30 mg/kg/day administer via drinking water, and all found doxycycline to greatly reduce the incidence of AAA formation as well as severity of the aneurysm.

Success in mice and rat studies has spurred human trials of doxycycline for the suppression of AAA [106-108]. Manning and Baxter conducted one of the first clinical trials that treated patients undergoing elective AAA repair for 7 days prior with 100 mg by mouth twice daily docycycline [108]. Examination of the tissue obtained from surgery found a great reduction in MMP-2, and -9 activities in treated patients compared to those who were not. A phase two study conducted by Baxter et al. observed 36 patients with AAA to evaluate treatment with 100 mg twice daily for 6 months [106]. Results from this study found no significant change in AAA diameter and substantially decreased MMP activity after 6 months, and that such doses were well tolerated. A placebo-controlled pilot study conducted by Mosorin et al. found that over 18 months, treatment with 150

mg/day doxycycline significantly reduced AAA expansion compared to the placebo group [107].

Another study conducted by Bartoli et al. compared wild type elastase perfused mice dosed with 100 mg/kg/day oral doxycycline with localized continuous injection of 0.75 to 1.0 mg/kg/day via osmotic minipumps [109]. This study found that localized infusion suppressed AAA formation equivalent to or even greater than that of oral administration, while plasma levels of doxycycline in the mice receiving infusion were undetectable.

In order to address the questions of whether the doxycycline serum levels needed for AAA inhibition achieved in animal models can be safely achieved in humans with standard dosages, Prall et al. conducted a controlled study [110]. Wild type mice with elastase perfusion were dosed with 0, 10, 50, and 100 mg/kg doxycycline, while human patients were given 100 mg twice daily. AAA reduction was observed in mice at 10 mg/kg and reduction increased with increased dosage, and the study was able to show that circulating doxycycline values in mice were found to be similar to plasma levels of doxycycline in human patients.

1.5. Summary and Conclusion

Over the past sixty years there has been significant effort devoted to using experimental animal models of aneurysm in order to understand and treat the human disease. The means of induction as well as the choice of approach is governed primarily by the questions being investigated by the researcher. Chemical and/or genetic models of aneurismal disease have arisen more recently. As our understanding of the mechanisms and pathways involved in aneurysm formation has improved, these new genetic models have become available to investigate potential causes for aneurysm and possible therapeutic targets. The chemically and/or genetically induced animal models are attractive from a biomechanical point of view, since these can be used to investigate how the mechanical properties of aneurysms alter during disease development. In addition, longitudinal studies based on the biomechanical analysis of mouse models that are

susceptible to aneurysm formation will inform about the process of aneurysm formation. Such future research will provide a meaningful link between the matrix degradation and inflammatory response known to be present in human AAA and how such changes eventually lead to the mechanical failure of ruptured AAA. In summary, there are potential applications of prognostic utility of assessment of aortic wall biomechanics and microstructure in prevention and medical treatment of aortic aneurysms and sudden aortic rupture.

CHAPTER 2: PRESENT STUDY UNDERLYING CHANGES IN MICROSTRUCTURE, MECHANICAL RESPONSE AND BIOCHEMESTRY IN THE APOE MOUSE MODEL OF ANEURYSM

2.1: Summary of Published Works

Additional methods, results, and conclusions of this study are presented in the papers appended to this dissertation (**Appendices A & B**). The following is a summary of the most important findings in those studies.

The $ApoE^{-/-}$ mouse model of aneurysm was chosen for this study and used to investigate the microstructural and biomechanical behavior of aortic tissues and any changes that occur as the disease develops and progresses within the animals. First the effect of AngII in C57BL/6 wildtype mice was investigated as a first step towards coupling changes in microstructure with altered mechanical behavior before looking into how such changes occur in the established $ApoE^{-/-}$ AngII infused mouse model of AAA. The objective of both studies also included utilizing the microbiaxial optomechanical device (MOD) in conjunction with the advanced intravital microscope (AIM) to determine how the microstructural and biomechanical properties are altered in the AAA model.

Methods included infusing $ApoE^{-/-}$ and wildtype mice with either saline or AngII for 14 and 28 days. Aortas were excised, cleaned of any connective tissue (**Figure 2.1**), and tested in a manner that simultaneously characterized the biaxial mechanical response of unfixed and unfrozen tissue and load-dependent extracellular matrix organization through multiphoton microscopy (**Figure 2.2**). From the mechanical test, each dataset was fit to a Fung-type constitutive model and the metrics of peak strains and stiffness values were compared across experimental groups. The mean mode and full width at half maximum of fiber histograms from two photon microscopy were also quantified in order to assess the preferred fiber distribution and degree of fiber splay, respectively based on the direction of increased load.

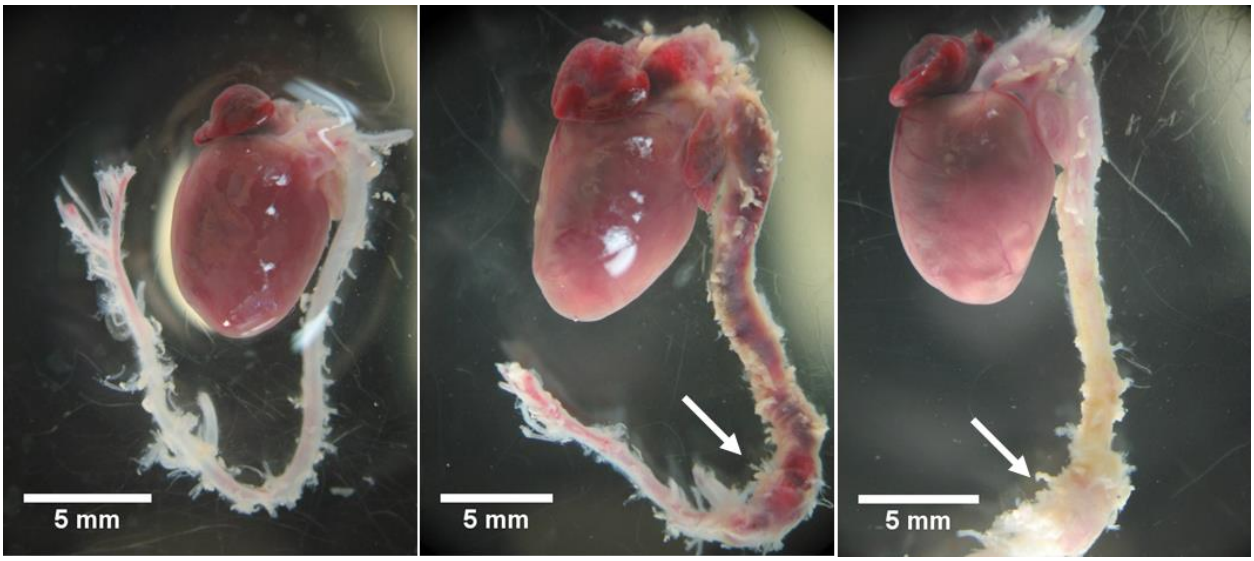

Figure 2.1: Representative aortas that have been removed and cleaned of excess connective tissue from a control mouse (Left), a 14 day ApoE$^{-/-}$ AngII infused aneurysmal mouse (Middle), and a 28 day ApoE$^{-/-}$ AngII infused aneurysmal mouse (Right). Arrows indicate an aneurysm in the suprarenal aortic region of the ApoE$^{-/-}$ AngII infused mouse that is absent in the wild-type saline infused mouse. Figure taken from Haskett et al, 2013 [111].

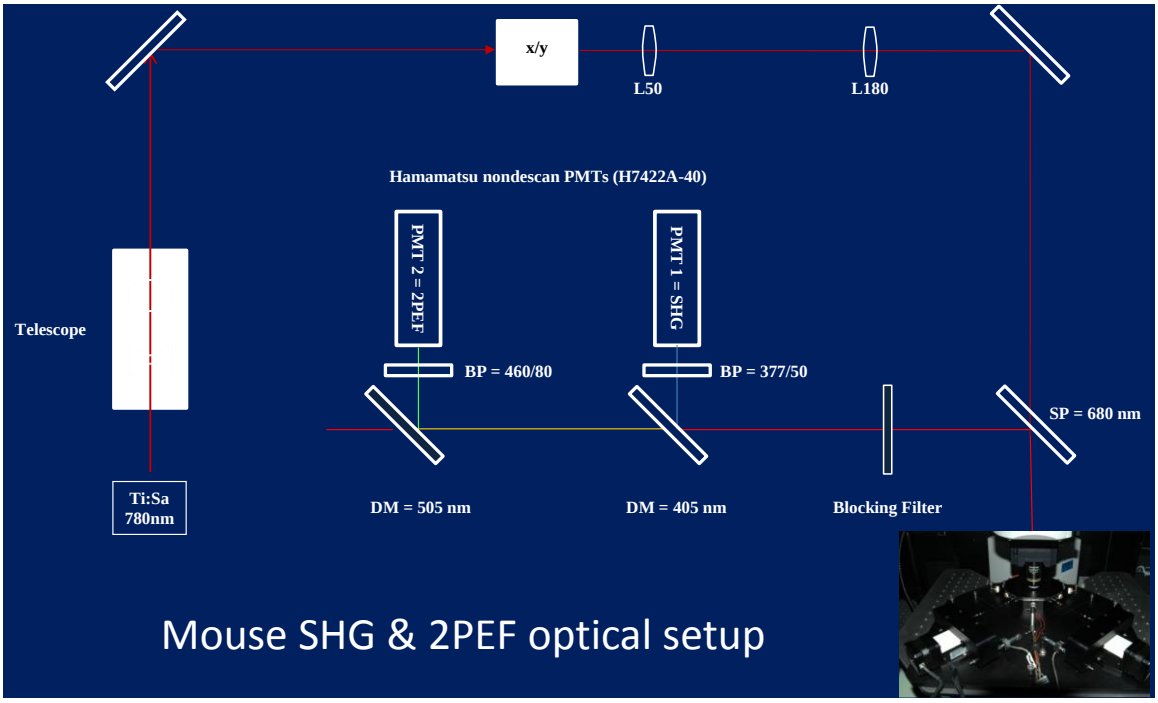

Figure 2.2: Optical path of TiSa laser used for 2-photon imaging along with the filters used for the each channel in conjunction with the MOD placed upon the AIM.

Important results from the studies showed that the axial stiffness of wildtype mice aortas was an order of magnitude larger than the circumferential stiffness. It was found that there was a significant decrease in circumferential strain in the ApoE$^{-/-}$ AngII infused aneurysmal model at both time points, and this decrease in circumferential strain was accompanied by an increase in circumferential stiffness, however, the circumferential stiffness of the aneurysmal model was not found to be significantly different from the controls or AngII infused wild-type mice due to the high variability (**Figure 2.3 A&B**). Additionally, biomechanical results found significant differences that were present at 14 days had returned to values closer to those of control mice by 28 days (**Figure 2.3 C**).

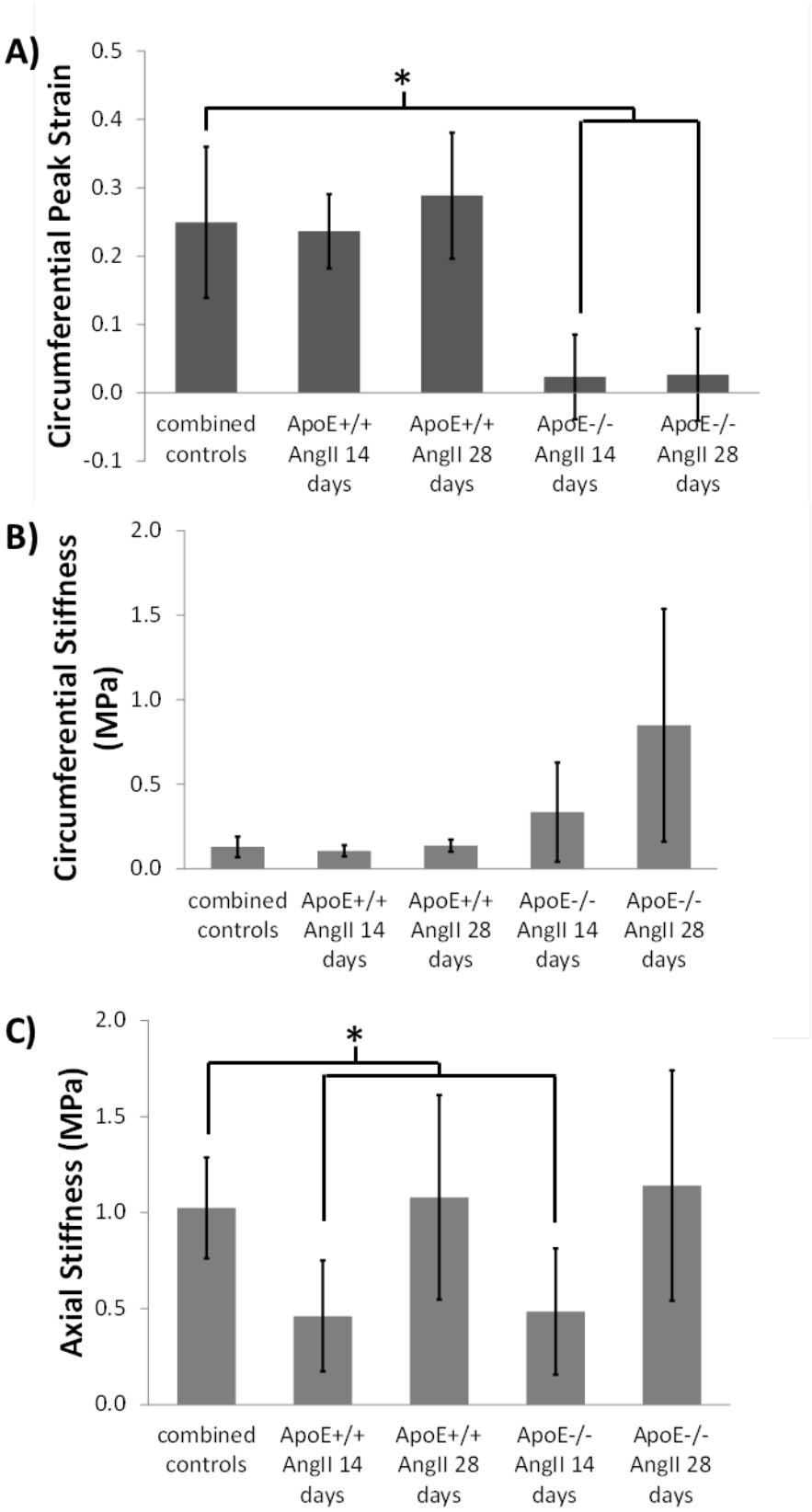
A)
Circumferential Peak Strain
0.5
0.4
0.3
0.2
0.1
0.0
-0.1
*
combined controls
ApoE+/+ AngII 14 days
ApoE+/+ AngII 28 days
ApoE-/- AngII 14 days
ApoE-/- AngII 28 days
B)
Circumferential Stiffness (MPa)
2.0
1.5
1.0
0.5
0.0
combined controls
ApoE+/+ AngII 14 days
ApoE+/+ AngII 28 days
ApoE-/- AngII 14 days
ApoE-/- AngII 28 days
C)
Axial Stiffness (MPa)
2.0
1.5
1.0
0.5
0.0
*
combined controls
ApoE+/+ AngII 14 days
ApoE+/+ AngII 28 days
ApoE-/- AngII 14 days
ApoE-/- AngII 28 days

Figure 2.3: A) The circumferential peak strain taken at the physiologic axial strain and pressurized to 100 mmHg. B and C) The circumferential stiffness and axial stiffness, respectively, defined as ∂S/∂E in the circumferential and axial directions at the physiologic axial strain and peak circumferential strain. Error bars shown are standard deviation (* P<0.05). Figure taken from Haskett et al, 2013 [111].

Findings also included that collagen fibers comprising the aortic microstructure were able to reorient in the direction of increased load in wildtype control mice, but this ability was diminished in remodeled AngII infused wildtype mice and completely lost in the $ApoE^{-/-}$ AngII infused aneurysmal. Collagen fibers found in the aneurysm model also exhibited a loss of the characteristic crimp seen in collagen fiber bundles of wildtype mice mice (**Figure 2.4**). Both metrics of fiber angle mean mode and FWHM showed gross changes between control and $ApoE^{-/-}$ AngII infused aneurysmal mice. This was likely due to the increased deposition of collagen fibers in a disorganized manner within the aneurysmal wall.

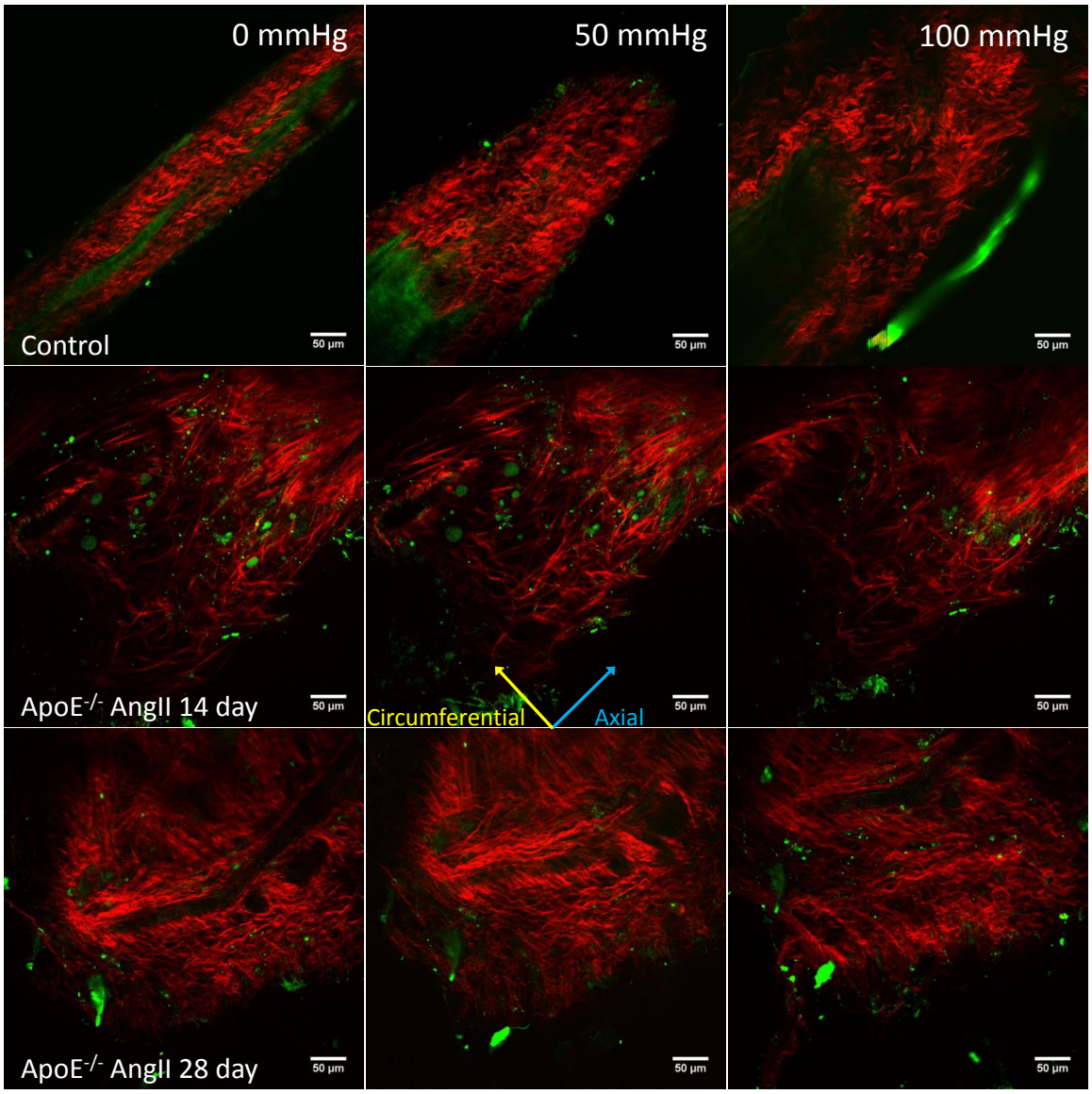

Figure 2.4: Representative multiphoton images of a control mouse aorta (Top), an ApoE-/- AngII mouse at 14 days (Middle), and ApoE-/- AngII infused mouse at 28 days pulled to the in vivo axial strain at both 0 mmHg (Left), 50 mmHg (Middle), and 100 mmHg (RIght). SHG channel (Red) represents the collagen content of the aorta, while NADH channel (Green) represents primarily the elastin content or lipid deposits. While some of elastin bands of the media are observable in the control images, these images are taken approximately in the adventitial layer of the aorta, which was observed to be thicker in both the AngII infused wild-type mouse and the

ApoE-/- AngII infused model. Blue and yellow arrows correspond to axial and circumferential directions respectively. In the saline mouse aorta the expected waviness of the collagen fiber bundles is evident in both unpressurized and pressurized states, while both the AngII infused wild-type mouse and the ApoE-/- AngII infused model aortas do not exhibit the expected waviness indicating collagen crimp Figure taken from Haskett et al, 2013 [111].

In conclusion of these studies, the return of some of the normal biomechanical function between 14 days and 28 days, in addition to the continuing changes that occur in the microstructure, suggests that a restorative response occurs in the $ApoE^{-/-}$ AngII infused model after the initial aneurysm formation. Such a finding, not know to be present in the human disease, may suggest that the $ApoE^{-/-}$ mouse model of aneurysm is not as similar as previously believed; though work looking towards understanding and promoting such remodeling could be advantageous. Additionally, the resulting biomechanical material parameters and fiber analysis from the studies is able to provide a basis for continued work into the modeling of aneurysmal progression the $ApoE^{-/-}$ AngII infused model of AAA.

2.2 2-Photon Characterization of Optical Proteolytic Beacons for Imaging Changes in MMP Activity in a Mouse Model of Aneurysm

Darren Haskett[1] MS, Tyler Smith[2] BS, Catalina Ardilia[1] MS, Tom Doetschman[3,4] PhD, Urs Utzinger[1,4,5] PhD, Dominic McGrath[1,2,4] PhD, Oliver McIntyre PhD[6], Jonathan Vande Geest[1,4,5,7] PhD

*1. Graduate Interdisciplinary Program of Biomedical Engineering**

*2. Department of Chemistry and Biochemistry**

*3. Department of Cellular and Molecular Medicine**

*4. Bio5 Institute**

*5. Department of Biomedical Engineering**

6. Departments of Radiology and Radiological Sciences and Cancer Biology, Vanderbilt University

*7. Department of Aerospace and Mechanical Engineering**

**The University of Arizona*

Tucson, AZ

Corresponding Author

Jonathan P. Vande Geest, PhD

The University of Arizona

Department of Aerospace and Mechanical Engineering

Department of Biomedical Engineering

Bio5 Institute

Graduate Interdisciplinary Program in Biomedical Engineering

1130 N. Mountain

PO Box 210119

Tucson, AZ 85721-0119

Phone: (520) 621-2514

Fax: (520) 621-8191

Email: jpv1@email.arizona.edu

2.2.1 Introduction

AAA has become an increasingly prevalent disease in elderly patients over 65 years of age in the United States with over 12% of men and 5% of women affected by the disease [4]. While rates of AAA have declined in some European and other nations [112], rates have stayed constant in the US at about 45,000 cases a year, with 10,000 people annually [113]. Furthermore, though mortality rates have fallen in recent years, AAAs still have a mortality rate that can be up to 85% and can be over 50% even in a medical setting when rupture occurs. In addition, AAAs have been an extenuating factor in over 35,000 deaths in the past two years and are responsible for nearly 150,000 hospitalizations each costing on average nearly $60,000 on average in the same time period [4, 113-116].

While a definitive cause for AAA remains unknown, it is generally accepted that the pathogenesis of AAA is combinatorial in nature involving several factors including atherosclerosis, inflammation, hemodynamics, smoking status, gender, age, and genetic predisposition [1, 2]. One of the reasons that so little is known about the initiation and progression of AAA disease is that data on the mechanobiology of the disease is limited to that collected at one time point, typically from a sample acquired during an OSR of an already mature (large) AAA.

In order to overcome the challenges of studying AAA initiation and progression in humans, an $ApoE^{-/-}$ AngII infused mouse model has been developed. This animal model has become prominent for the study of AAA as it displays many of the same histological and biological characteristics as native human AAA, including atherosclerotic plaque formation, medial degeneration, thrombus formation, and an increase in MMP activity [15, 117]. This model has allowed recent work to focus on understanding the underlying mechanisms of disease initiation and development, specifically the role of increased MMP production in aneurysmal tissue that appears to be associated with extensive remodeling of the extracellular matrix (ECM) and is implicated in the development of aneurysms [46, 92-95].

While MMPs are known to be up-regulated in both animal and human AAA [1, 2, 11, 12, 46, 94, 102, 106, 108, 109, 118-120], the temporal distribution of their activity and how these correlate with AAA initiation and progression has yet to be quantified. In order to solve this problem, recent work has begun exploring molecular imaging agents to study the temporal distribution of biological events in mouse AAA [121-123]. One novel imaging technique that has the potential to provide temporal *in vivo* imaging of MMP activity, developed for imaging matastases in a mouse model, involves the use of Foerster Resonance Energy Transfer (FRET) based proteolytic beacons (PBs) [124-127]. However, this modality has yet to be used in a model of AAA, nor combined with 2-photon (2P) imaging which would also provide spatial determination of fluorescence of the PB and its activation *in situ*, as well as imaging of the ECM (e.g., using second harmonic gerneration (SHG) and 2P excited fluorescence (2PEF)). 2P imaging also has the benefits of superior image quality, deeper optical sectioning, and reduced photo damage to tissue.

The temporal distribution of MMP activity in the $ApoE^{-/-}$ AngII infused mouse model of AAA has yet to be coupled to the resulting functional tissue damage, and as such the link between the time-course of protease activity, load-dependent ECM remodeling, mechanical wall stress, and aortic dilation remain unclear [103, 128]. In order to generate a basis for further studies into AAA disease progression, the objective of this work is to determine the feasibility of using novel PBs combined with 2P imaging techniques to assess both temporal and spatial alterations in MMP activity, as well as simultaneous collagen and elastin imaging, in the $ApoE^{-/-}$ AngII infused mouse model of aneurysm. The results reported here show significantly enhanced activation of PB in aneurysmal aortic tissue as compared with controls,demonstrating the feasibility of using PBs in combination with 2P imaging to assess the temporal and spatial distribution of MMP activity within developing aortic aneurysms.

2.2.2 Materials and Methods

2.2.2.1 Beacon synthesis and characterization

PBs employed for this study with MMP cleavable specific peptide linkers were synthesized at the Vanderbuilt University Institute of Imaging Science based on previous protocols [124-127, 129]. These PBs used for *in vitro* and *ex vivo* optical imaging of MMP activity had in particular, a fluorescein (FL) labeled peptide sequence (BR2) cleavable by MMP2 and MMP9 (that show selectivity either for gelatin and collagen) attached to a generation 4 polyamidoamine (G4-PAMAM) dendrimer scaffold that previously had the addition of PEG to increase solubility. The highly branched (FL-BR2)-PAMAM-PEG was then labeled with tetramethylrhodamine (TMR) to generate the completed PB using methodology established by the McIntyre laboratory [124, 125, 127]. The advantages of using dendrimers are controlled assembly, size, biocompatibility, long circulation time due to decreased vehicle uptake, and the multivalency of the dendrimer allowing for the addition of multiple sensor and reference fluorophores. Additionally, PAMAM dendrimer backbones with either FL or TMR attached were used for initial imaging calibrations (**Figure 2.5**).

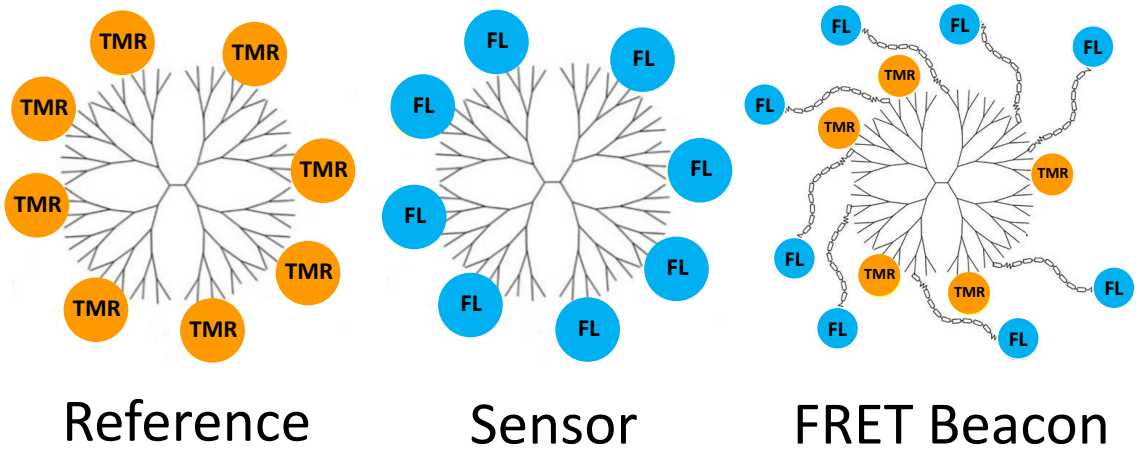

Figure 2.5: PAMAM dendrimer backbone with reference TMR fluorophores, sensor FL fluorophores, and the FRET-based PB with sensor attached using a peptide linker.

2.2.2.2 Quantitative fluorescence imaging of proteolytic beacons using single-photon and two-photon microscopy

Initial single-photon characterization of the PBs was done on a Synergy H1 plate reader from BioTek®, with excitation for the fluorophores FL and TMR between 480 and 490 nm and 520 and 530 nm respectively. Characterization of the newly synthesized PBs was done by first confirming the desired proteolytic cleavage using known activator trypsin (25200-056, Life Technologies™, USA), and confirmation of selective cleavage in the presence of specific MMPs was demonstrated *in vitro* using active MMP-2 and -9 (Enzo® Life Sciences BLM-SE360 & BLM-SE237) in a reaction buffer containing 0.05 M Tris-HCL, 0.15 M NaCl, 5 mM $CaCl_2$, 0.2 mM sodium azide pH 7.6 (E12055, Life Technologies™, USA) through setting up a number of assays that varied both concentration and time.

Sensor and reference fluorescence of each beacon were also measured using two-photon excitation conducted on the AIM, an NIH sponsored shared device [130-132]. The AIM uses a pulsed Titanium-Sapphire laser (680-1060nm) for simultaneous two-photon excitation and second harmonic imaging. For this study imaging was done using an Olympus XLUMPLFL 20x water immersion objective with a numerical aperture of 0.9. Multiple channels were used with band-pass filters set to capture the sensor (FL – 525/50 nm) and reference (TMR – 607/70 nm) emissions. Work into preparing modifications to the AIM imaging system were done by calibrating both *in vitro* and *ex vivo* testing with appropriate fluorescence standards and phantoms [127] in preparation for quantitative fluorescence imaging studies. In two-photon imaging, proteolytic cleavage of the PB was evident by an increase in the sensor/reference fluorescence ratio of the PB as compared to the uncleaved control using known protease concentrations used for quantitative assessment [127].

2.2.2.3 VSMCs acquisition and culture and characterization

In order to attempt to recreate an *in vitro* model of the $ApoE^{-/-}$ AngII infused model of AAA, the culture of murine vascular smooth muscle cells (VSMCs) isolated from individual $ApoE^{-/-}$ and control mouse aortas was done using a method adapted from Ray et al. 2001 [133]. All animal use and experimental procedures for mouse testing were

performed according to the approved protocol (#06–045) of the University of Arizona Institutional Animal Care and Use Committee (IACUC) and Animal Welfare Assurance Number (A3248–01). ApoE$^{-/-}$ mutant mice were obtained from Jackson Lab (Bar Harbor, ME) (Stock#:002052) [134]. ApoE$^{-/-}$ mice on C57BL/6J background were maintained as a colony of heterozygous animals and fed a standard diet and provided water *ad libitum*. Briefly, fully grown adult mice (4 to 6 months old) were euthanized and secured in supine position. The thorax was opened and viscera removed to expose the heart and aorta, which was then removed from the spinal column and dissected from the heart to the diaphragm. Under a dissecting microscope the aorta was cleaned and the adventitia was removed. After being transferred to a culture hood, the aorta was cut into 1-2 mm^2 pieces in a Petri dish with culture medium, aortic pieces were placed in a small tissue culture tube containing a collagenase enzyme solution in an incubator for 4-6 hours. The tissue pieces were then resuspended in VSMC culture medium (Dulbecco's Modified Eagle Medium (Life Technologies^{TM}, USA) supplemented with 10% Fetal Bovine Serum (GemCell^{TM}), 100U/ml of penicillin, 100 μg/ml of streptomycin, 5 μg/ml of amphotericin B (Fungizone), and 25 mM HEPES (Life technologiesTM, USA)) and centrifuged repeatedly and transferred to a single well of a 48-well plate and placed in incubator undisturbed for 5 days. Cells were near confluence after 10 days at which time they are transferred to new well plates. Cell identity was confirmed by immunocytochemistry (ICC) on cells cultured onto glass coverslips after the third passage, using double immunostaining by primary polyclonal antibodies goat anti-alpha smooth muscle actin (ab21027; Abcam, USA) conjugated with secondary antibody donkey anti-goat FITC (ab6566; Abcam, USA) and primary polyclonal antibodies rabbit anti-calponin (ab46794; Abcam, USA) conjugated with secondary antibody goat anti-rabbit Cy5 (ab6564; Abcam, USA) in that order to prevent cross-conjugation. Cell nuclei were counterstained using VECTSHIELD® mounting media containing 4',6-diamidino-2-phenylindole (DAPI) from Vector Laboratories , USA. For all other experiments performed, cells from passages 4-6 were used.

2.2.2.4 FRET imaging of altered MMP expression in vitro through the addition of AngII and doxycycline

Assays of murine VSMCs were used to assess the stability and MM-dependent cleavage of the PBs used in these studies, i.e. their utility for detecting and quantifying differences in MMP expression. VSMCs in culture were plated and allowed to proliferate until 60% confluence, at which point the standard culture media was removed and replaced with culture media lacking fetal bovine serum and incubated for 24 hours. $ApoE^{-/-}$ and wildtype VSMC assays were then injected with either AngII (0.5 ug/ml) in order to increase MMP expression and activation [95, 135-137], or doxycycline (high = 50 μg/ml) in order to decrease MMP expression and activation [138, 139] for 24 hours. The aspirate was then removed and used to determine any quantifiable differences in MMP expression and activity between wild type control VSMCs and $ApoE^{-/-}$ VSMCs using both a Synergy H1 plate reader and the AIM.

Michaelis-menten kinetic studies were not conducted to determine substrate affinity as the product of MMP cleavage can then again act as the substrate and does not follow the simple model. Instead, single photon *in vitro* assays were conducted modeled after an EnzChek® Gelatinase/Colagenase FRET based Assay Kit from (Molecular Probes®, Invetrogen, Carlsbad, CA). For single photon imaging using the plate reader, aliquots of 100 μl of aspirate taken from *in vitro* culture of each group (AngII – control, low, high and doxycycline – control, low, high) were placed in a 96 well plate and PBs were added at a concentration of 0.144 nmol/ml, excited at a wavelength of 480 nm, and then read at a wavelength of 520 nm at the times indicated. After 2 hours of incubation and single-photon imaging, two-photon measurements were conducted using 50-100 μl of aspirate suspended through surface tension between the objective and the slide with the column illuminated. PBs were excited at a wavelength of 780 nm using the configuration described in section 2.2. Differential expression of MMPs activity measured in 2P mode was compared to single-photon measurements and to MMP protein expression assessed using gelatin zymography [140] (section 2.5).

2.2.2.5 Measured change in MMP activity compared to gelatin zymography

All PB assays were compared to gelatin zymography, which has been used previously as a standard measurement for detecting MMP expression [141-143]. Briefly, aliquots of cell aspirate were electrophoresed on a 10% Criterion™ Zymogram Ready Gel® (#345-0080, Bio-Rad, USA) according to the manufacturer's instructions and based off a protocol described by Troeberg and Nagase [143]. After electrophoresis, the gel apparatus was disassembled and the gel was placed in zymogram renaturing buffer (#161-0765, Bio-Rad, USA) for one hour at room temperature, after which the gel was placed in zymogram development solution (#161-0766, Bio-Rad, USA) and incubated at 37^0C overnight. The gel was then stained with Coomassie Brilliant Blue R-250 (#161-0400, Bio-Rad, USA) staining solution for 1 hour and distained using a distaining solution until clear bands appeared. The resulting bands were then imaged on an Epson Perfection V750-M Pro Scanner and analyzed via densitometry using the open source software ImageJ by densitometry.

2.2.2.6 Ex vivo imaging of MMP activity in the AngII infused ApoE$^{-/-}$ mouse model of aneurysm (In situ zymography)

The AngII infused ApoE$^{-/-}$ mouse model of aneurysm has been used in our lab previously [111], and all experimental procedures were performed according to the approved protocols of University of Arizona IACUC. Briefly, Using the colony described in *section 2.3*, four to six month old adult ApoE$^{-/-}$ mice were administered with either saline or AngII (1000 ng/min/kg, A9525 Sigma-Aldrich, St. Louis, MO USA) through a subcutaneously implanted Azlet® mini-osmotic pump (Durect Corp) for 14 days and placed on a high fat diet as described in the literature [10, 144].

AngII infused ApoE$^{-/-}$ mice exhibiting aneurysm (defined as a >50% increase in aortic diameter or the onset of dissection) and ApoE$^{-/-}$ saline infused control mice had their aorta isolated and surgically excised from the ascending aorta to the iliac bifurcation and cleaned of perivascular tissue as described previously [111, 144]. The aorta was then trimmed leaving the suprarenal segment of the aorta and immersed in a PB solution

(0.144 nmol/ml) and incubated at 37° C overnight to allow for diffusion through the tissue and then cannulated on custom-pulled micropipette capillary tubes and secured using cyanoacrylate adhesive gel and placed in the microbiaxial optomechanical device (MOD) [145]. The abdominal aortas were then imaged on the AIM (configured for MOD imaging) using PBs (section 2.2) at and excitation wavelength of 780 nm with a laser power on the sample of 25 mW. A third collection channel was added to collect SHG, a non-linear optical technique for imaging collagen fibers of the adventitia (SHG bandpass filter– 377/50 nm). *En face* image stacks were taken at 40mW power using a 500 x 500 μm field of view at 4 μm steps from 100 μm to 200 μm in depth based on thickness of the sample and signal loss. The aorta was then immersed in 5% low melting temp agarose and cross-sectional sections 200 μm in thickness were cut using a vibratome (model 5100mz-Plus, Lafayette Instrument Ltd.). The cross-sectional slices were then imaged as described above.

2.2.2.7 Statistics

A one way ANOVA was used to compare across treatments and imaging tests to determine any statistical differences in MMP activity between groups eachof which contained 6 wells a peace (n=6). A Student's t-test was used to determine differences in MMP activity between aneurysmal and non-aneurysmal aortas in ex vivo 2P imaging using PBs based on mean intensities. All statistical analyses were performed in SigmaPlot (v. 13.0, SPSS, Chicago, IL).

2.2.3 Results

2.2.3.1 VSMCs acquisition and culture and characterization

Identity of the isolated SMCs used in the *in vitro* model of ApoE$^{-/-}$ AngII infused model of AAA was confirmed through ICC. The cells expressed both alpha-smooth muscle actin and calponin and mark them as VSMCs (**Figure 2.6**). However, the expected long filament markers specific to VSMCs expressing a contractile phenotype [146] were not present suggesting the cells may have become quiescent. No

morphological differences were observed between ApoE$^{-/-}$ VSMCs dosed with AngII, doxy, or controls.

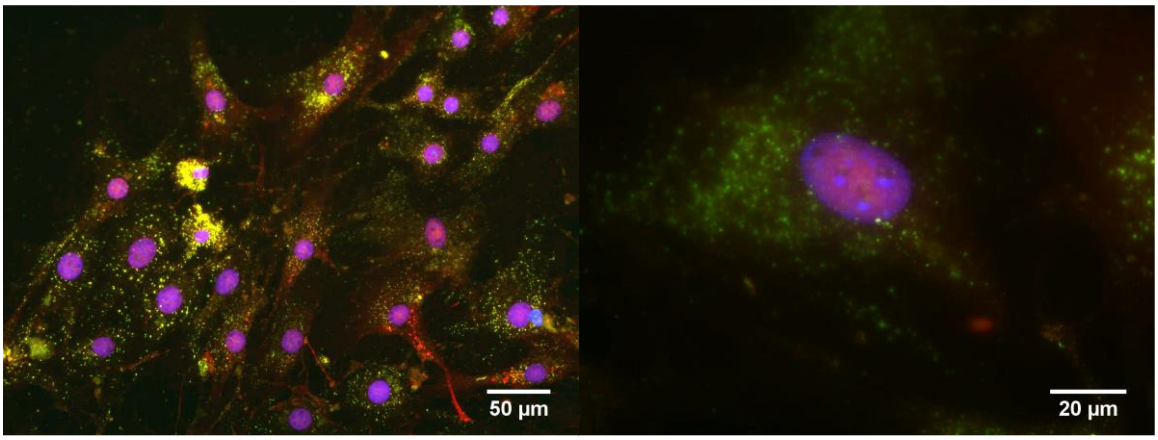

Figure 2.6: Immunofluorescence images of mouse VSMCs at 20x (left) and 60x (right). Smooth Muscle Alpha Actin (FITC), Calponin (TexasRed), and DAPI used for staining of nuclear membranes.

2.2.3.2 PB Characterization through single photon and two-photon spectra with cleavage

Initial single photon emission sweeps (485 excitation) found the sensor (FL-PAMAM) gave a strong peak at 520 nm and a reference (TMR-PAMAM) showed almost no emission with a small emission peak around 580 nm (**Figure 2.7, left**). However, uncleaved PBs containing both sensor and reference molecules give a strong emission peak at 580 nm when excited between 480 and 490 nm, signifying FRET activity. Emission spectra were also gathered from *in vitro* assays using trypsin, which is also capable of cleaving the peptide linkers, in order to demonstrate the increase the sensor/reference fluorescence ratio of the PBs and distinguish increases in enzymatic levels (**Figure 2.7, right**). Note that the increase in Sensor fluorescence is also accompanied by a slight increase in reference fluorescence. This is due to the energy loss that can occur with FRET. When the fluorophores are separated through cleavage of the peptide bond, the sensor is still able to be excited and will emit. However, this increase in reference fluorescence is not nearly as much as the sensor so the sensor/reference ratio will increase dramatically.

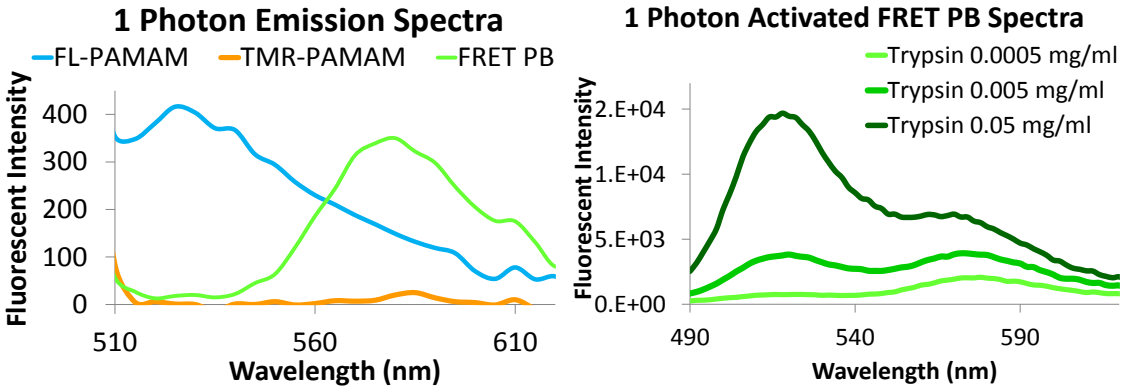

Figure 2.7: Left) Spectra from FL-PAMAM dendrimer excited by 485 nm light and emitting a peak around 520 nm, the TMR-PAMAM dendrimer shows greatly reduced fluorescence at its peak emission (590 nm), while the PB shows minimal FL fluorescence but strong fluorescence corresponding with TMR indicating efficient FRET in the uncleaved PB. Right) Emission spectra (ex 490 nm) of PB after 2 h incubation with varying concentrations of trypsin (as indicated) showing enhanced FL Sensor fluorescence with increasing trypsin indicating trypsin cleavage of PBs by *in vitro*.

Single photon in vitro assays were conducted modeled after an EnzChek® Gelatinase/Collagenase FRET based Assay Kit from (Molecular Probes®, Invetrogen, Carlsbad, CA). PBs containing BR1 and BR2 peptide sequence were found to be cleavable by both MMP 9 and MMP2 with a sensor to reference ratio determined at varying time and concentrations (**Figure 2.8**). Sensitivity down to 0.03 U/ml MMP was found after 3 hours of incubation with higher concentrations requiring shorter incubation times. Like the EnzCheck® Assay, longer incubation times (~16 hours) for the PBs were found to have higher sensitivity and used in the *ex vivo* mouse aorta tests (section 3.6).

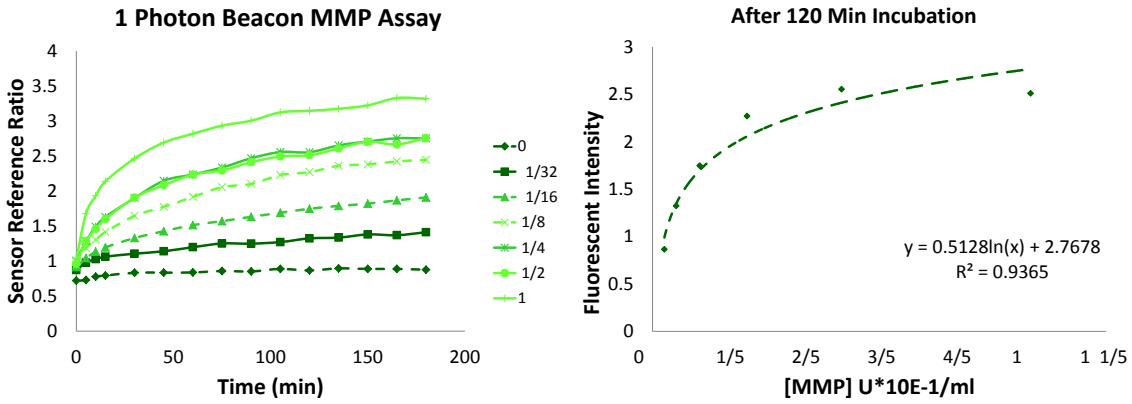

Figure 2.8: Left) Sensor/Reference ratios for single photon measurements of kinetics of the BR2 peptide PBs at multiple concentrations (U/ml) incubated in ~72 pMoles PB/ml in reaction buffer for up to three hours. Right) The sensor/reference ratio at 120 minutes plotted against MMP concentration representing the reaction progress enzyme kinetics.

For initial 2P studies, PBs were diluted to ~72 pMoles PB/ml in a slide well and the suspension illuminated (**Figure 2.9A**). Unactivated PBs were imaged in both the FL (sensor) and TMR (reference) channels from 720 to 980 nm for excitation, then activated using trypsin and incubated for 2 hours and imaged again. Mean intensities of the 2P spectra showed a large difference in the emission between unactivated and activated PBs around 780 nm, the peak output of the titanium-sapphire laser (**Figure 2.9B**). Analysis of the sensor/reference ratio through the 2-Photon spectra revealed a peak in sensor reference ratio around 760 nm and the largest increase in sensor reference ratio with proteolytic activation also at 760 nm (**Figure 2.9C**). An excitation wavelength of 780 nm was then chosen for all following 2-Photon imaging as it provided a sufficient increase in sensor/reference ratio. 780 nm is also near the peak power output of the titanium-sapphire laser enhancing fluorescence signal, and allows for the collection of SHG in *ex vivo* imaging distinct from the FL and TMR channels.

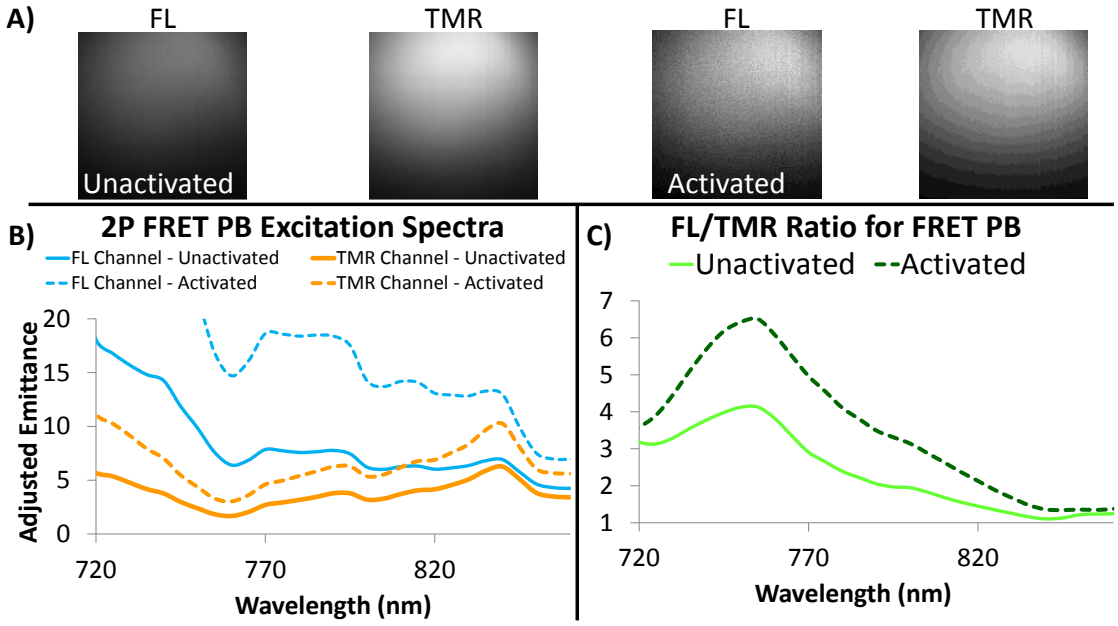

Figure 2.9: A) Images of the fluorescence of PBs in suspension in the FL and TMR channels for both unactivated and activated PBs. Activation is evidenced by the increase in the mean intensity in the FL channel for the activated PBs and the enhanced FL/TMR ratio. B) Two photon spectral excitation sweeps for the PB before (solid lines) and after (dotted lines) protease activation for both the FL (blue) and TMR (orange) emission channels. C) Changes in the FL to TMR 2P fluorescence ratio illustrates a peak around 760 nm excitation that increases significantly with protease activation.

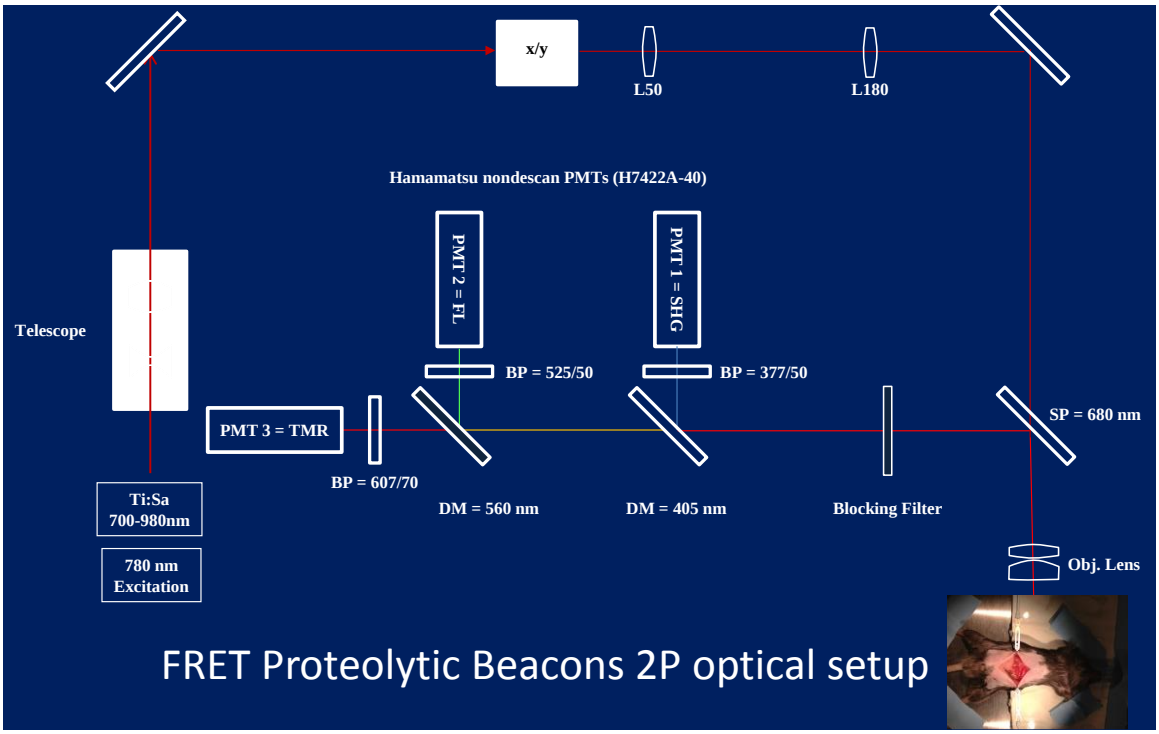

Figure 2.10: Optical path of TiSa laser used for 2-photon imaging along with the filters used for the each channel used for imaging of PBs upon the AIM.

2.2.3.3 FRET imaging of altered MMP expression in vitro through the addition of AngII and doxycycline compared to gelatin zymography

Assays of wild type and ApoE$^{-/-}$ murine VSMCs were cultured in well plates until near confluence. The standard VSMC culture media was then removed and replaced with media lacking FBS. Multiple wells of VSCMs were then administered AngII, doxy, AngII & doxy, or left untreated (control) and incubated for up to 72 hours. Aspirate was then removed from each well and each group was then tested for MMP activity using 1-photon imaging with PBs, 2-photon imaging with beacons, and then compared to gelatin zymography (**Figure 2.11**). Densitometry of the gelatin zymography was determined using ImageJ Gel Analysis tool, 1-photon data was taken from the Gen5 software provided by BioTek®, and 2-photon readings were acquired using the mean intensity of each image using ImageJ. Both densitometry and 2-photon imaging show an increase in MMP activity for cultures dosed with AngII over cell cultures that received no treatment.

2-photon imaging of aspirate dosed with doxycycline (both Doxy and AngII & Doxy groups) exhibited widely varying fluorescent emission that appeared to be due to a confounding effect of the doxycycline on fluorescence rather than cleavage of the PBs.

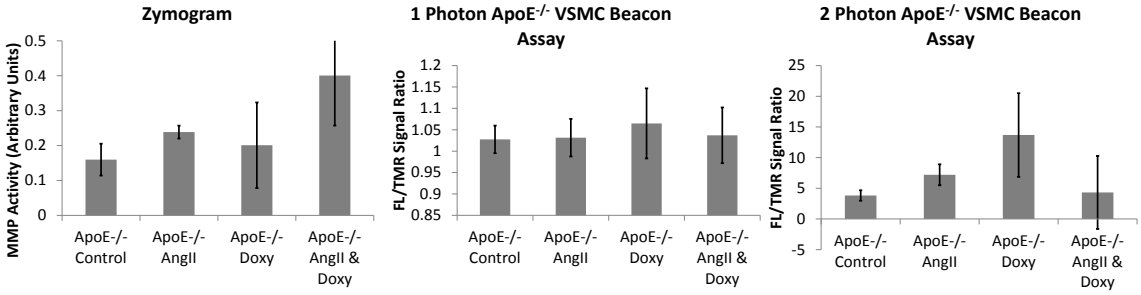

Figure 2.11: Results of the *in vitro* assays for ApoE$^{-/-}$ VSMC aspirate from densitometry measurements from gelatin zymography (Left), 1-photon fluorescence on a plate reader (middle), and from 2-photon images (left).

2.2.3.4 Ex vivo imaging of MMP activity in the AngII infused ApoE$^{-/-}$ mouse model of aneurysm

Both wildtype control (n=2) and ApoE$^{-/-}$ mice infused with AngII for 14 days (n=3) were sacrificed and their abdominal aortas removed and cleaned for imaging whether the ApoE$^{-/-}$ AngII aortas were fully aneurysmal or not, as long as there was evidence of remodeling. Multiple *en face* 2-photon image stacks were taken for both wildtype and ApoE$^{-/-}$ mice infused with AngII for 14 days prior to PB treatment and after 16 hours of incubation on the MOD at 0 mmHg (**Figures 2.12 & 2.13, respectively**). Within the adventitia where SHG denoted the presence of collagen, without PBs there was little to no signal in either the FL (sensor) or TMR (reference) channel. After immersion in a ~72 pmol/ml PB solution for up to 16 hours, there was a distinct increase in signal found in both FL (sensor) or TMR (reference) channels. After immersion in PBs for 16 hours, ApoE$^{-/-}$ 14 day AngII infused mouse aortas that had undergone remodeling displayed increased FL signal relative to wild type control aortas that had also been immersed in PBs (**Figure 2.13**), and an increase in the sensor/reference ratio indicating an increase in MMP activity within the adventitia of the remodeled aortas.

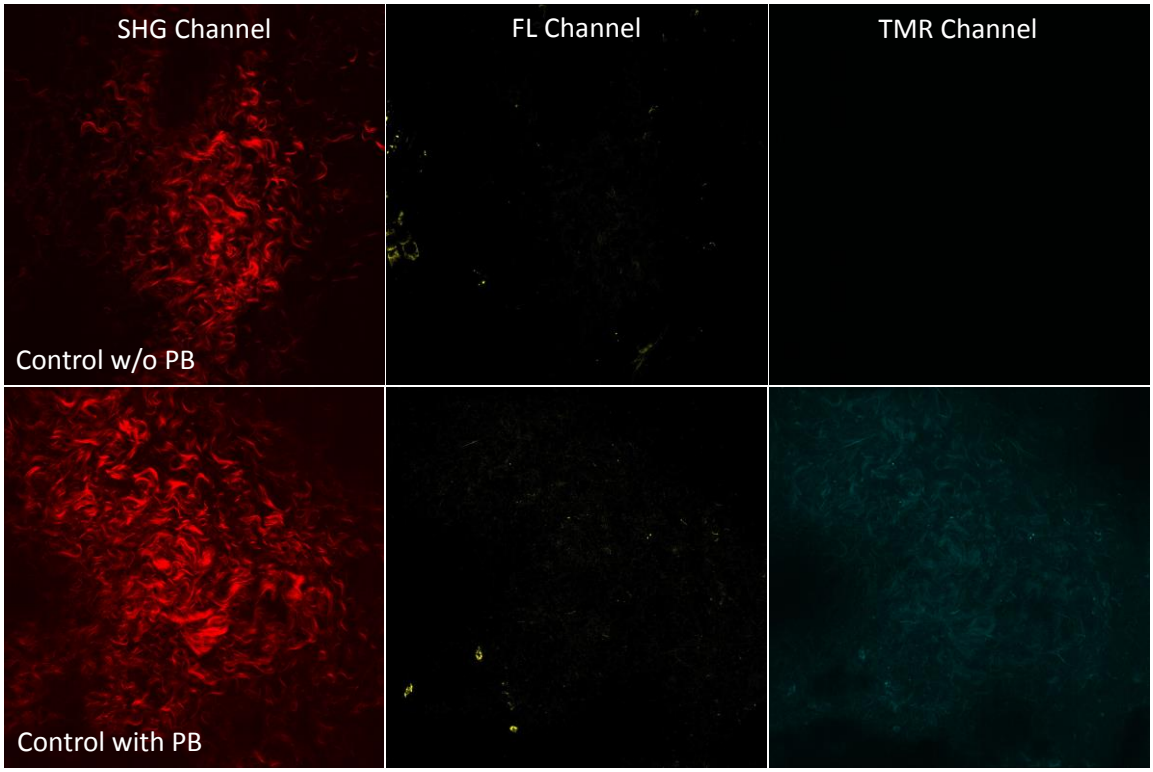

Figure 2.12: Top Row) Representative 2-Photon single slice images of the adventitia for SHG, FL, and TMR channels prior to incubation with PBs for a wild type control mouse depicting collagen signal (red), while signal in the FL and TMR channels is absent. Bottom Row) Representative 2-Photon single slice images of the adventitia for SHG, FL, and TMR channels after 16 hours of incubation with PBs for a wild type control mouse depicting collagen signal (red), and signal in the FL and TMR channels.

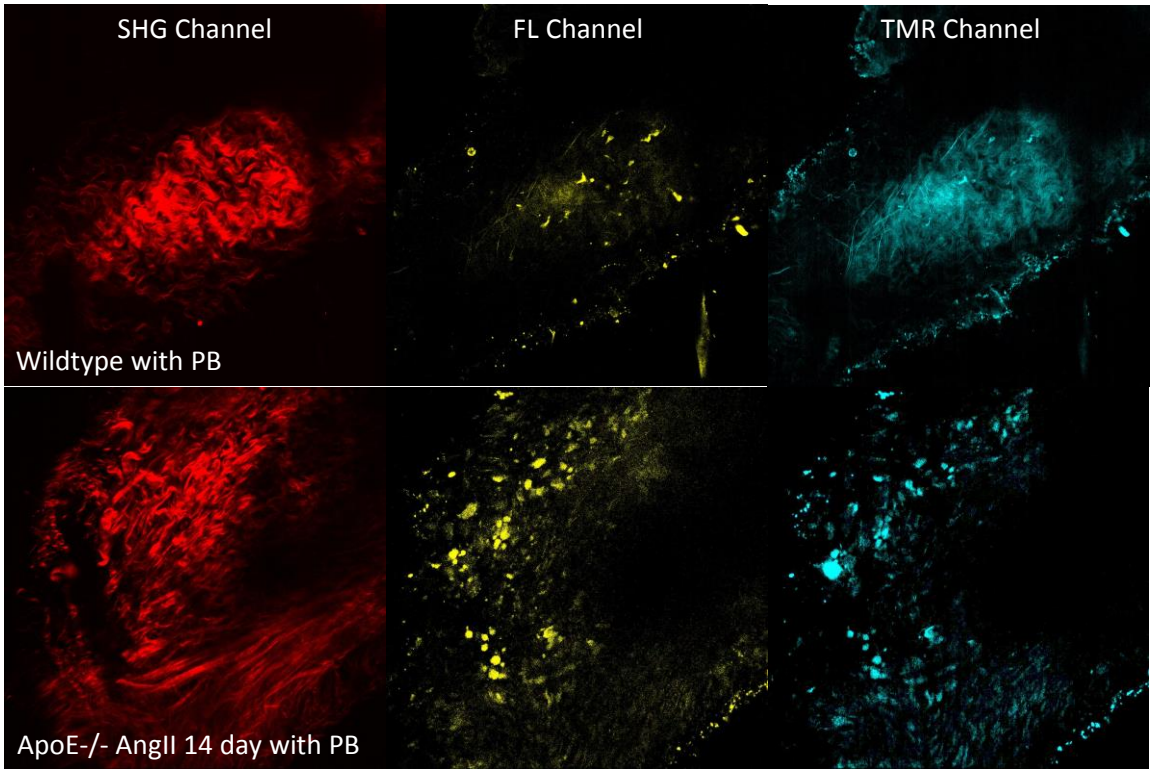

Figure 2.13: Top Row) Representative 2-Photon single slice images of the adventitia for SHG, FL, and TMR channels after to being incubated with PBs for a wild type control mouse aorta depicting collagen signal (red), with signal in the FL and TMR channels indicating MMP activity. Bottom Row) Representative 2-Photon single slice images of the adventitia for SHG, FL, and TMR channels after 16 hours of incubation with PBs for an ApoE$^{-/-}$ 14 day AngII infused remodeled mouse aorta depicting collagen signal (red), with increased signal in the FL and TMR channels. Notice that where SHG is present, autofluorescence is absent, so in the corresponding images, the fluorescence is being generated primarily by the PBs.

After *en face* imaging of both ApoE$^{-/-}$ 14 day AngII infused remodeled and wild type control aortas, multiple 200 μm thick cross-sectional slices from each specimen were also imaged. Although auto-fluorescence of the elastin within the medial layers contributes to both the FL and TMR channels, the ApoE$^{-/-}$ 14 day AngII infused

remodeled aorta images had significantly greater sensor/reference ratios ($p=0.004$) and can be seen in maximum intensity projections of the image stacks (**Figure 2.14**).

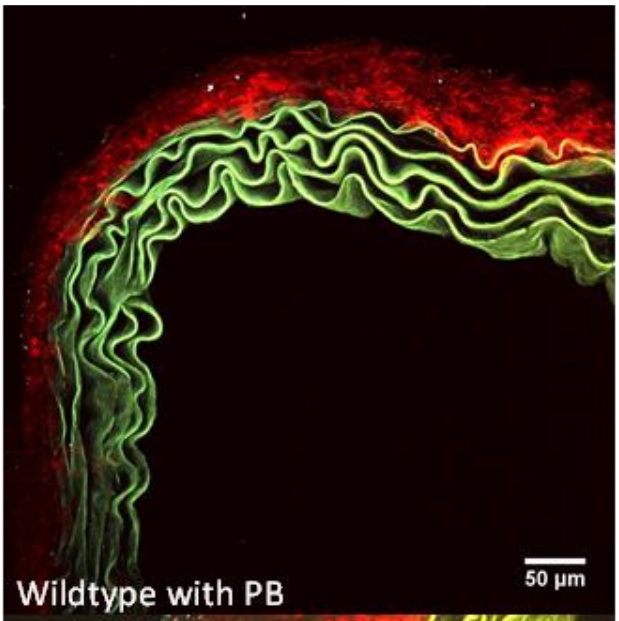
Wildtype with PB
50 µm

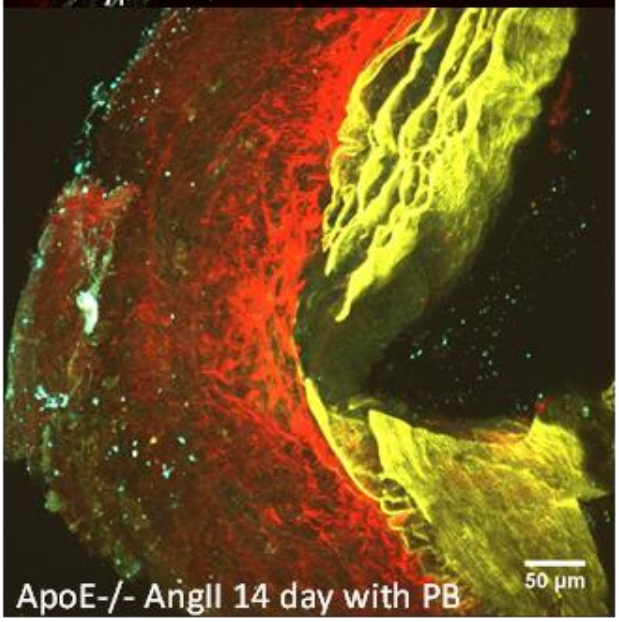
ApoE-/- AngII 14 day with PB
50 µm

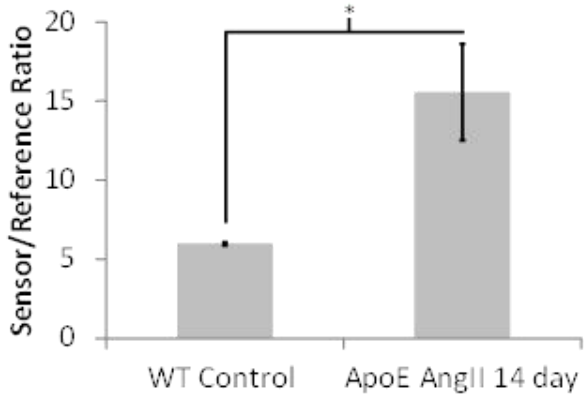
Sensor/Reference Ratio
20
15
10
5
0
*
WT Control
ApoE AngII 14 day

Figure 2.14: 2-Photon maximum intensity projections for cross-sectional image stacks of wild type (Top) and ApoE$^{-/-}$ 14 day AngII infused remodeled (Middle) aortas using 4 µm steps up to 100 µm. Images are an overlay of 3 channels: SHG (Red) primarily depicting collagen, FL (yellow) signifying the cleaved FL fluorophore and auto-fluorescence of the elastin in the medial layer of the aorta, and TMR (Cyan) signifying mostly the remaining uncleaved PBs still undergoing FRET and the auto-fluorescence of the elastin in the medial layer of the aorta. The mean intensity in the FL and TMR channels for each maximum intensity projection for every slice from each specimen was used to give the sensor reference ratio (Bottom) and indicates an increase in MMP activity in the ApoE$^{-/-}$ 14 day AngII infused remodeled aortas over the wild type controls (*p=0.004).

2.2.4 Discussion

2.2.4.1 Summary of Results

With the 1-photon FRET characteristics demonstrated, the 2P excitation spectra were obtained and used to characterize the proteolytic cleavage of PBs. Proteolytic cleavage of the PBs was observed in the 2P spectra and an excitation wavelength of 780 nm was chosen for imaging studiesshowing a large increase in FL emission and a significant increase in sensor/reference ratio upon cleavage and allowed of collection of SHG at 390 nm, distinct from the FL and TMR fluorescence channels. Although attempts at recreating the ApoE$^{-/-}$ mouse model of aneurysm *in vitro* using VSMCs and the addition of did not recapitulate the *in vivo* process, it was shown using gel zymography and 2P imaging that the addition of AngII into cell culture did increase expression and activity of MMPs, which has been reported to occur in the animal model.

Although the ApoE$^{-/-}$ AngII infused mice did not all present with fully formed aneurysms as is expected with between 50-75% of the animals in this model [10, 147], evidence of dilation, adventitial thickening, changes in collagen fiber structure, and increased MMP activity were still observed. Imaging of the PBs in *ex vivo* tests showed a

threefold increase in sensor reference ratio between wild type control and ApoE$^{-/-}$ remodeled aortas in cross-sectional image stacks.

2.2.4.2 Relation to previous work

Activatable fluorescent imaging tools have become a very important in imaging biological systems especially during the disease process both *in vitro* and *ex vivo*, and increasingly *in vivo*. Much of this work has been done using quenched agents that then generate high levels of fluorescence when the fluorophore is released by and enzyme-mediated reaction. Agents such as these have been put to commercial use such as EnzChek® Gelatinase/Colagenase FRET based Assay Kit from (Molecular Probes®, Invetrogen, Carlsbad, CA) or MMPSense® and MMPSense FAST® (PerkinElmer inc. Waltham, MA) in studies where MMPs play a central role in diseases such as cancer invasion, progression and metastasis, rheumatism, pulmonary diseases, and cardiovascular disease [148-150]. Each of these can have both advantages and disadvantages, such as EnzChek® is specifically for *in vitro* assays, and for *ex vivo* and *in vivo* assays, MMPSense® will often have issues with vehicle uptake or reduced circulation time [129, 151]. Unlike these commercially available products, use of PBs comes with certain advantages, especially in the use of the dendrimer backbone, which allows for a much more customizable product (see *section 2.4.4 future studies*).

As not all ApoE$^{-/-}$ 14 day AngII-infused mice presented with fully formed suprarenal aneurysms, they cannot be directly compared to previous results, mechanical or otherwise. However, those that did undergo remodeling but did not present with full aneurysm formation expressed a phenotype similar to wildtype mice infused with AngII [144]. While other studies that looked into temporal MMP activity in the ApoE$^{-/-}$ 14 day AngII-infused mouse model like Eagleton *et al*. [135], were able to show significantly increased MMP expression after 21 days in the ApoE$^{-/-}$ AngII-infused aneurysmal model through gene expression and zymography, use of PBs was able to show elevated MMP activity levels in the aneurysmal model compared to control aortas as early as 14 days. Additionally, to the best of our knowledge, this is currently the first and only study to

look into the 2P spectra of such PBs and their fluorophores as well as FRET activity under 2P conditions. We believe that the current study is also the first to collect SHG simultaneously with FRET PBs in living tissue, a technology that may be extremely useful in future mechanobiological studies.

2.2.4.3 Limitations

The ApoE$^{-/-}$ AngII infused mouse model of aneurysm has become a standard in genetic animal models for AAA, however one limitation of this study is the inherent uncertainty in trying to recreate the model *in vitro* and moving even further away from the human disease. Also, *in vitro* studies of the ApoE$^{-/-}$ VSMCs did not clearly show an increase or reduction in MMP activity with the addition of AngII and/or doxycycline. Reasons for this could include the VSMCs becoming quiescent and no longer responding to factors as they would have *in vivo*, which also might explain the absence of long strands of α-actin in the ICC the would be visible in the cells if they were expressing a contractile phenotype [146]. Also, the method for AngII administration could have affected the cellular response, as in the animal model the AngII is administered continuously through an osmotic pump, while *in vitro* the AngII was administered as a bolus.

For the *ex vivo* studies, limitations of imaging with the AIM and MOD set have been described previously [111, 144, 152]. In this study, it was found that the autofluorescence given off by the elastin in the medial layer bleed over into both the FL and TMR channel, however measurements taken in the adventitial layer did not contain any autofluorescence as evidenced by the lack of any signal in the before image stacks even though SHG signal was well defined. We could be justly certain that any signal in the FL and TMR channels was due to fluorescence given off by the PBs. If the autofluorescence of elastin was needed to be avoided, then studies could be reserved to just the adventitia. However, as evidenced in the comparison between cross-sectional images of the wildtype control and ApoE$^{-/-}$ AngII infused remodeled aorta, there was still

a measurable difference in the signal to reference ratio of the PBs that was significant and demonstrated increased MMP activity within the medial layer.

One problem that were encountered when imaging *ex vivo* aortas was the difficulty in matching locations of before image stacks and images stacks taken after being immersed in PBs. Also, we are assuming the PBs to be completely diffuse in the image stacks taken after immersion.

2.2.4.4 Future Studies

Continued use of PBs in the study of vascular disease would allow for the investigation into a more detailed time course for the initiation, progression, and rupture of aneurysm in the $ApoE^{-/-}$ AngII mouse model by quantifying changes in protease activity, load dependent ECM microstructure, and biomechanical response at early time points post AngII infusion *In vivo* imaging and then on into fully aneurysmal states and beyond.

Future studies in this line of research have the possibility of combining FRET imaging *in vivo* as has been done previously in cancer research [124-127] and eventually localized drug delivery through the specialized dendrimer backbone that is used in the PBs [153-155]. Prodrugs developed in such ways that the drug is attached to a dendrimer backbone offer several advantages over traditional drug delivery systems that can have severe side effects. Dendrimers are an ideal candidate for prodrug development as these molecules can be modified to manipulate their size, solubility, drug loading, and bioactivity and can be loaded with fluorophores as well for simultaneous imaging [124, 127]. For example, such molecules can be modified to present binding domains that will allow future local targeting. Recent work has also demonstrated that dendritic structures can be chemically designed to disassemble in response to physical or chemical signals [154, 156, 157]. This may allow the design of an amplification scheme, where one stimulus releases multiple drug molecules, and FRET based PBs would allow for imaging of such a system.

2.2.4.5 Conclusions

PBs can prove to be a useful tool for future studies that can look into and investigate a more detailed time course for the initiation, progression, and rupture of aneurysm in the ApoE$^{-/-}$ AngII mouse model. Develop a novel dendritic prodrug that releases a known broad based MMP inhibitor (doxycycline) upon cleavage by MMPs themselves.

2.3: Development and Characterization of a MMP Activated Doxycycline Prodrug for the Inhibition of Protease Activity and Reduction of Aneurysm Formation in a Mouse Model of Aneurysm

Darren Haskett[1] MS, Tyler Smith[2] BS, Urs Utzinger[1,3,4] PhD, Dominic McGrath[1,2,3] PhD, Jonathan Vande Geest[1,3,4,5] PhD

*1. Graduate Interdisciplinary Program of Biomedical Engineering**

*2. Department of Chemistry and Biochemistry**

*3. BIO5 Institute**

*4. Department of Biomedical Engineering**

*5. Department of Aerospace and Mechanical Engineering**

**The University of Arizona*

Tucson, AZ

Corresponding Author

Jonathan P. Vande Geest, PhD

The University of Arizona

Department of Aerospace and Mechanical Engineering

Department of Biomedical Engineering

BIO5 Institute

Graduate Interdisciplinary Program in Biomedical Engineering

1130 N. Mountain

PO Box 210119

Tucson, AZ 85721-0119

Phone: (520) 621-2514

Fax: (520) 621-8191

Email: jpv1@email.arizona.edu

2.3.1 Introduction

It is clear that there is a need to develop improved methods of both diagnosing and treating patients with small progressing AAAs. As a result of this clinical issue, significant research has focused on improving the diagnosis and treatment options for patients with AAA [5, 158-163]. Pharmacological methods of treatment using anti-hypertensives, statins, ACE inhibitors, and protease inhibitors, such as doxycycline, to reduce aneurysmal expansion have been explored with a few displaying promising results [107, 110, 164-167].

The $ApoE^{-/-}$ AngII mouse model of AAA has been used by several groups, including ours [103, 111], for this purpose as it maintains many of the same characteristics of human AAA disease including inflammation, atherosclerosis, thrombus deposition, and preference of dilation in the abdominal aorta [12, 15, 111, 117, 122]. This proposal is focused on using the $ApoE^{-/-}$ AngII model to develop novel diagnostic and therapeutic agents for AAA.

There have also been several recent studies in both animals and in humans suggesting that the pharmaceutical treatment of AAA with broad based MMP inhibitors such as doxycycline reduces AAA growth [107, 109, 118, 168, 169]. One recent human study provided conflicting evidence in support of this hypothesis [166]. We hypothesize that the limited local dose of DOX from systemic oral delivery limits its potential in inhibiting the local up-regulation of MMPs in AAA. We also seek to develop a novel prodrug that releases DOX locally in response to elevated MMP activity and reduce any pathologic response that leads to loss of mechanical function as an initial step for treatment of AAA disease.

2.3.2 Materials and Methods

2.3.2.1 Prodrug synthesis, Characterization, and Enzymatic Assays

The prodrug, constructed in the laboratory of Dr. Dominic McGrath, will utilize specified MMP cleaved peptide linkers described by Hu et al, 2010 [170] for use with doxyrubicin prodrugs, as linkers with 9-aminodoxycycline (**Figure 2.15A**). These peptide linkers are

cleavable by the gelatinases with selectivity for MMP2 and MMP9, and 14 (**Figure 2.15B**).

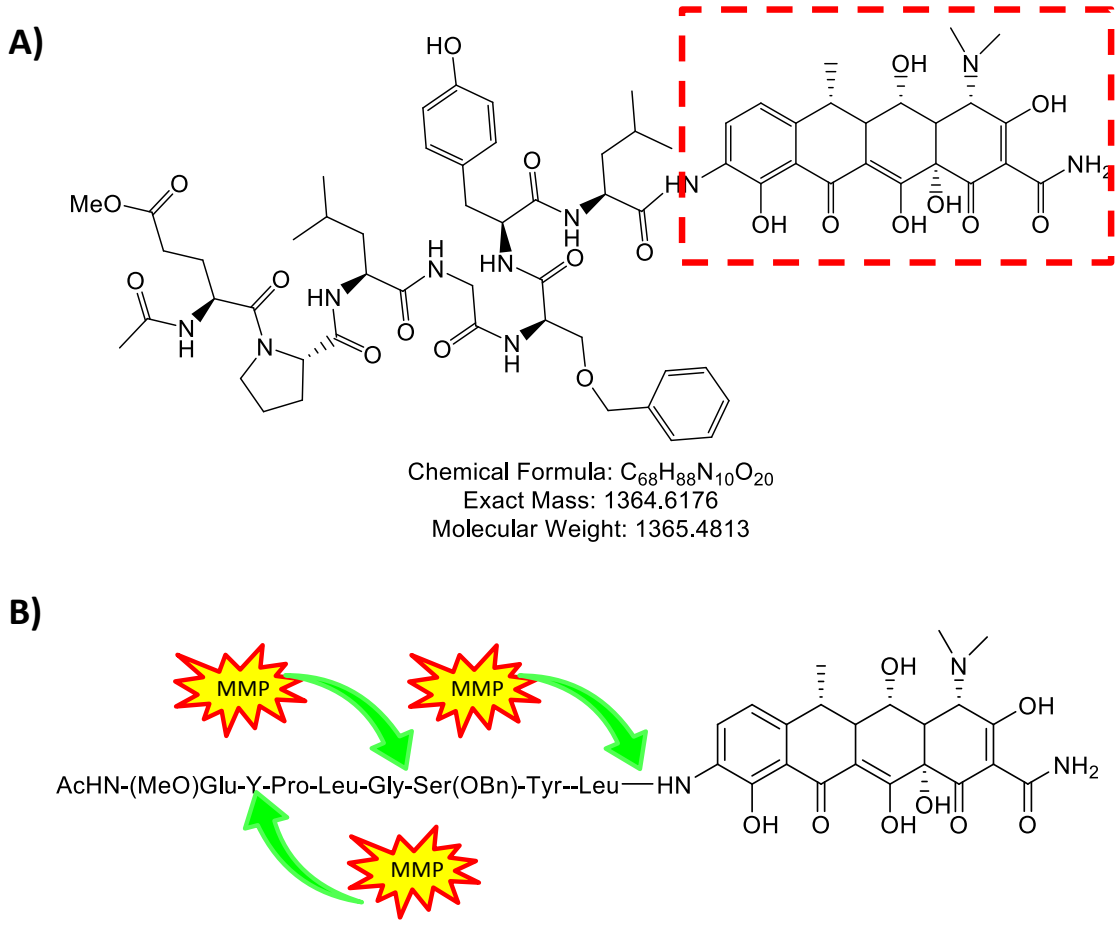

Figure 2.15 A) Bond diagram of the 9-amino doxycycline (outlined in red) attached to the peptide linker. B) Mechanism of action by which MMPs will degrade the peptide chain eventually releasing 9-amino doxycycline.

Briefly, Doxycycline (1 g, 2.16 mmol) was dissolved in 20 mL of concentrated H_2S0_4 and cooled to 0°C. Sodium nitrite (290 mg, 3.38 mmol) was added slowly over 10 min. The reaction mixture was stirred an additional 3 h and then diluted with 30 mL of methanol. The solution was poured into ice-cooled, stirred ether (500 mL), and the mixture was filtered. The precipitate was washed well with ether and dried to yield a pale yellow solid (0.71 g, 67%). The solid was used without further purification.

Crude 9-nitro doxycycline (1 g, 2.04 mmol) was dissolved in 25 mL of methanol and poured into a 500 mL Paar hydrogenation flask. Palladium (10%) on charcoal (0.1 g) was added along with 2.5 mL of concentrated HCl. The vessel was charged with 50 psi of H2, and the bottle was stirred at room temperature for 18 hours. The catalyst was filtered through Celite and filtrate was diluted to 50 mL with methanol containing HCl and rapidly dripped into cold stirred ether (500 mL) to give a light tan powder in 85% (795 mg).

After the peptide linker was attached to the 9-amino doxycycline, creation of the complete prodrug was confermed through mass spectrometry. Cleavage of the prodrug and release of the 9-amino doxycycline was also confirmed through mass spectrometry and High Performance Liquid Chromatography using activated MMPs. Pro-MMPs 2, 9, and 14 (Enzo® Life Sciences, #ALX-200-419, # ALX-200-422, # ALX-201-100) were activated using amino-phenyl mercuric acetate (APMA) (#A9563, Sigma-Aldrich, St. Louis, MO USA) based off of a protocol described by Sellers et al. [171].

2.3.2.2 VSMCs acquisition and culture and characterization

The isolation and culture of murine VSMCs are described in section 2.2.3. For alternative assays, porcine VSMCs were used from the explant method used previously in our lab [146]. Briefly, aortas were obtained from the University of Arizona Meat Science Laboratory 10-20 min post-mortem. The adventitia and intima were removed from the explants in sterile conditions. The medial layer was cut into small pieces, and the explants were placed in 60 mm petri dishes containing 5 ml of Dulbecco's Modified Eagle Medium (DMEM) from Gibco® (Life technologies™, USA) supplemented with 10% Fetal Bovine Serum (FBS) from GemCell™, 100U/ml of penicillin, 100 mg/ml of streptomycin, 5 mg/ml of amphotericin B (Fungizone), and 25 mM HEPES from Gibco® (Life technologies™, USA). The culture medium was changed every other day and cultures were maintained in a humidified environment at 37° C and 5% CO2. Cell outgrowth from the explants was observed after two weeks.

Again, cell identity was confirmed by immunocytochemistry (ICC) on cells cultured onto glass coverslips after the third passage, using double immunostaining by primary polyclonal antibodies goat anti-alpha smooth muscle actin (ab21027; Abcam, USA) conjugated with secondary antibody donkey anti-goat FITC (ab6566; Abcam, USA) and primary polyclonal antibodies rabbit anti-calponin (ab46794; Abcam, USA) conjugated with secondary antibody goat anti-rabbit Cy5 (ab6564; Abcam, USA) in that order to prevent cross-conjugation. Cell nuclei were counterstained using VECTSHIELD® mounting media containing 4',6-diamidino-2-phenylindole (DAPI) (Vector Laboratories , USA). For all other experiments performed, cells from passages 4-6 were used.

2.3.2.3 MMP activity in Cultured Murine VSMCs through Zymography and Prodrug Metabolism

The rate of metabolism of the prodrug in cell culture was measured using *in vitro* assays of VSMCs. Cells were brought to 60% confluence using VSMC culture medium that was changed every other day in a humidified environment at 37^0C and 5% CO_2. Upregulation of MMP activity was achieved with the addition of AngII (A9525, Sigma-Aldrich, St. Louis, MO USA) to the culture medium and verified through gel zymography.

Briefly, aliquots were electrophoresed on a 10% Criterion™ Zymogram Ready Gel® (#345-0080, Bio-Rad, USA) according to the manufacturer's instructions and based off a protocol described by Troeberg and Nagase [143]. After electrophoresis, the gel apparatus was disassembled and the gel was placed in zymogram renaturing buffer (#161-0765, Bio-Rad, USA) for one hour at room temperature, after which the gel was placed in zymogram development solution (#161-0766, Bio-Rad, USA) and incubated at 37^0C overnight. The gel was then stained with Coomassie Brilliant Blue R-250 (#161-0400, Bio-Rad, USA) staining solution for 1 hour and destained using a destaining solution until clear bands appeared.

Prior to treatment with the prodrug, the culture medium was removed and replaced with culture medium that did not contain fetal bovine serum and incubated overnight. The doxycycline prodrug was then added to the medium. Test assays were then incubated for 24 hours after which the aspirate was removed and aliquots tested for MMP activity. Aliquots of the aspirate were also removed and centrifuged with acetonitrile. The supernatant was then removed and injected into the HPLC device and eluted as described before (section 2.1) to determine presence of doxycycline and doxycycline conjugates.

2.3.2.4 Toxicity assays of doxycycline derivatives on VSMCs

In order to measure cytotoxicity of the prodrug and the 9-Aminodoxycycline released after proteolytic cleavage and compare it to standard doxycycline a CellTiter 96 AQueous One Solution Cell Proliferation Assay® (Promega, Wisconsin, USA) was used with the dye reagent MTS ([3-(4,5-dimethylthiazol-2-yl)-5-(3-carboxymethoxyphenyl)-2-(4-sulfophenyl)-2H-tetrazolium, inner salt) under manufacturer instructions. Briefly, using murine VSMCs with multiple sets and controls (media without cells, media with cells and without MTS, media with cells and MTS without Doxy/9-Amino, and increasing concentration of Ethanol and DMSO). The following increasing concentrations of Doxy, 9-Amino, prodrug, ethanol, and DMSO were used: 90.9, 107, 130.4, 145.2, 152.5, 159.6, 166.66, 173.5, 186.9, and 200 μg/ml. These concentrations were used based on previous MTS assays that suggested lower concentrations of each compound were less than 10% cytotoxic. In order to quantify cytotoxicity we measured absorbance at 490nm on a BioTek® Synergy H1 Hybrid Plate Reader. The absorbance was then quantified, as a percent of the control without prodrug, in order to graph % Activity vs. [μg/ml].

2.3.2.5 In situ Reduction of MMP activity in the ApoE$^{-/-}$ AngII infused mouse model of aneurysm (initiation of disease, zymography, imaging)

Using the ApoE$^{-/-}$ AngII infused mouse model of aneurysm, the ability of the prodrug and conjugates to affect aneurysm initiation and progression compared to standard doxycycline was investigated. Use of the model has been described previously [111]. Briefly, using the same colony described in *section 2.2*, adult mice (approximately six months old) ApoE$^{-/-}$ mice were administered with AngII (1000 ng/min/kg) along with either 30mg/kg/day doxycycline, 30mg/kg/day equivalent prodrug, or vehicle through an intra-peritoneal Azlet® mini-osmotic pump for 7 days and placed on a high fat diet as reported previously [10, 111, 172]. The ability of the prodrug to reduce aneurysm formation or progression will be assessed qualitatively and quantitatively by sacrificing the mice, excising the aorta, and mounting the aorta into the tubular biaxial assembly of our MOD in order to measure outer diameter at pressures seen *in vivo* [145]. The aorta was then homogenized and analyzed for both MMP content (gelatin zymography) and doxycycline/prodrug concentrations using mass spec and HPLC. Additional tissue from the heart was also homogenized and analyzed for both MMP content as well as doxycycline and prodrug content for comparison.

2.3.3 Preliminary Results

2.3.3.1 Characterization of Prodrug through Mass Spectrometry and High Performance Liquid Chromatography (HPLC)

Mass spectrometry results (**Figure 2.16**) show that when incubated in a mixture containing MMP 2, MMP9, and MMP14 that the peptide linker is degraded and 9-amino doxycycline is released. Full degradation of the prodrug occurs within 75 minutes *in vitro*, while the actual kinetics and rate at which the prodrug is cleaved still need to be determined.

Experiments using HLPC were conducted to determine the rate at which MMPs would degrade the peptide chain and release 9-amino doxycycline. Unfortunately, due to the dated equipment and faulty second batch of prodrug, no useful data sets were able to be collected (**Figure 2.17**).

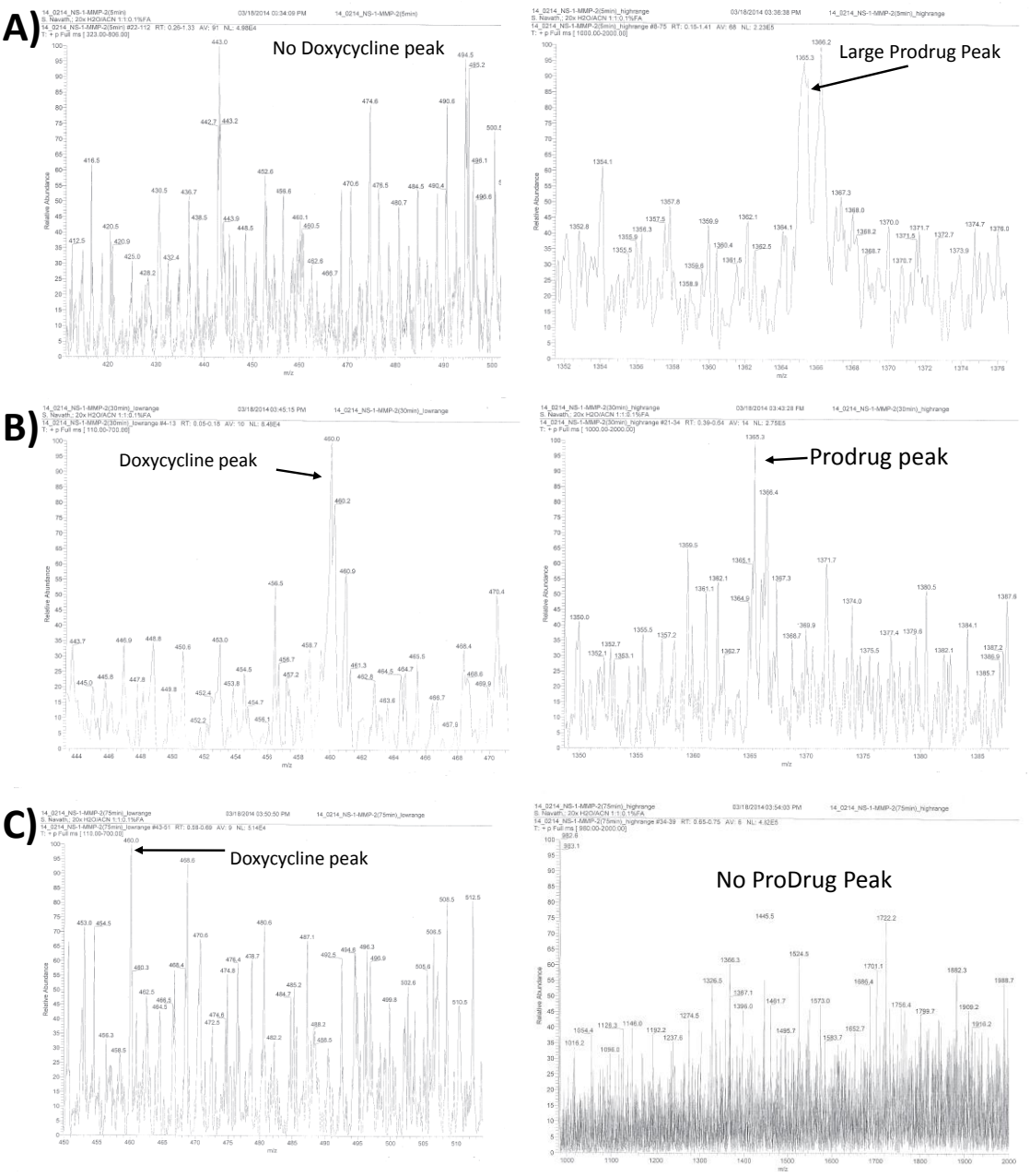

Figure 2.16: Mass spectrometry results from incubation of prodrug with activated MMPs at 5 min (A), 30 min (B), and 75 min (C) demonstrating digestion of the peptide linker and release of the 9-amino doxycycline. Left and right columns are displayed as the difference in molecular weights between 9-amino doxycycline and the prodrug was too great to depict the peaks on the same scale.

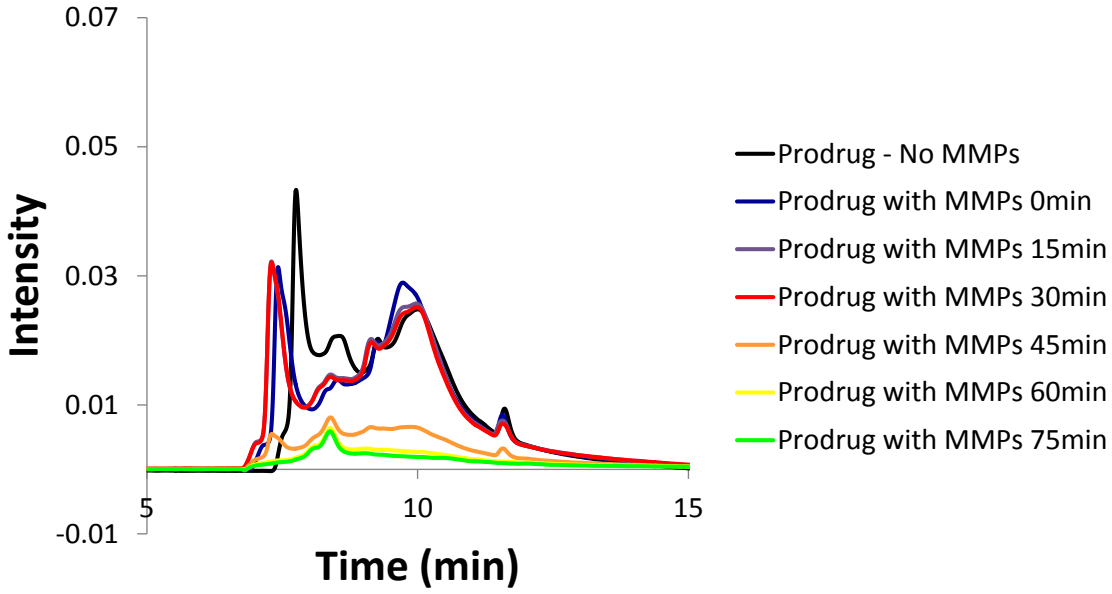

Figure 2.17: HPLC showing different peaks of the prodrug, 9-amino doxycycline, and the peptide linker after digestion with active MMPs.

2.3.3.2 Changes in MMP activity with the addition of Prodrug and doxycycline in vitro

After the porcine VSMCs were cultured to 80% confluence, the standard media was removed and replaced with media that did not contain fetal bovine serum. Wells were then separated into groups that were given either doxycycline, 9-amino doxycycline, or used as controls. After 48 hours, the aspirate was then removed and tested for the presence of MMPs using gel zymography. Densitometry analysis of the gelatin zymography (**Figure 2.18**) determined using the ImageJ Gel Analysis tool showed that doxycycline did reduce the amount of MMPs expressed by the VSMCs *in vitro* after 48 hours, and that 9-amino doxycycline significantly reduced the amount of MMP activity compared to controls ($p=0.037$).

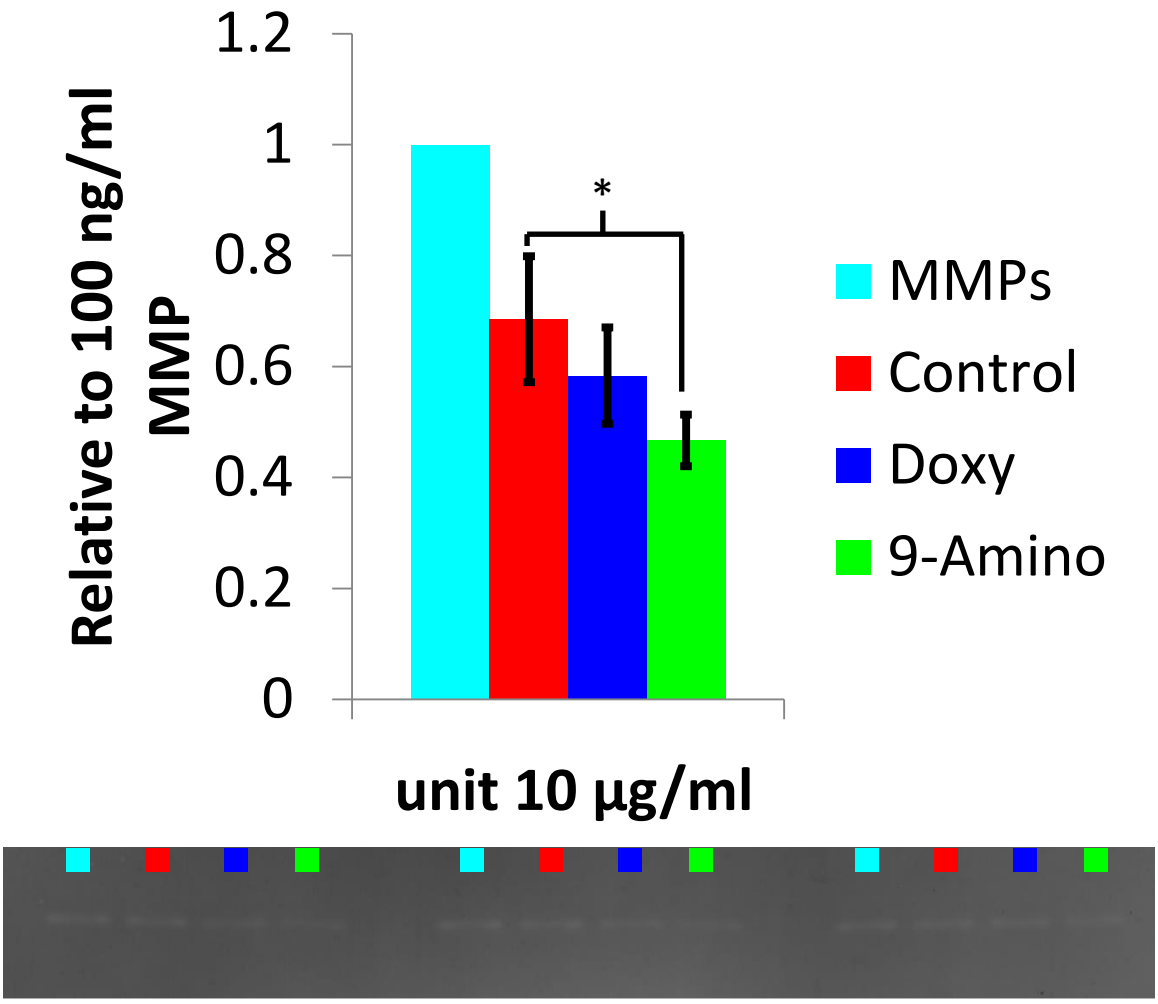

Figure 2.18: Gel zymography results from wildtype VSMC aspirate show a decrease in MMP activity with the addition of both doxycycline and 9-amino doxycycline (* P ≤ 0.05).

2.3.3.3 Toxicity assay of doxycycline derivatives on VSMCs

The MTS assay (**Figure 2.19**), performed in order to measure cytotoxicity of the 9-amino doxycycline to standard doxycycline found that the 9-amino doxycycline was slightly more toxic having an LD-50 level of 156.8 µg/ml compared to doxycycline at 148.9 µg/ml. Compared to ethanol, with an LD-50 level of 55 µg/ml, both the 9-amino

doxycycline and doxycycline are much better tolerated *in vitro*, and the efficacious dose for both was much lower at 10 μg/ml.

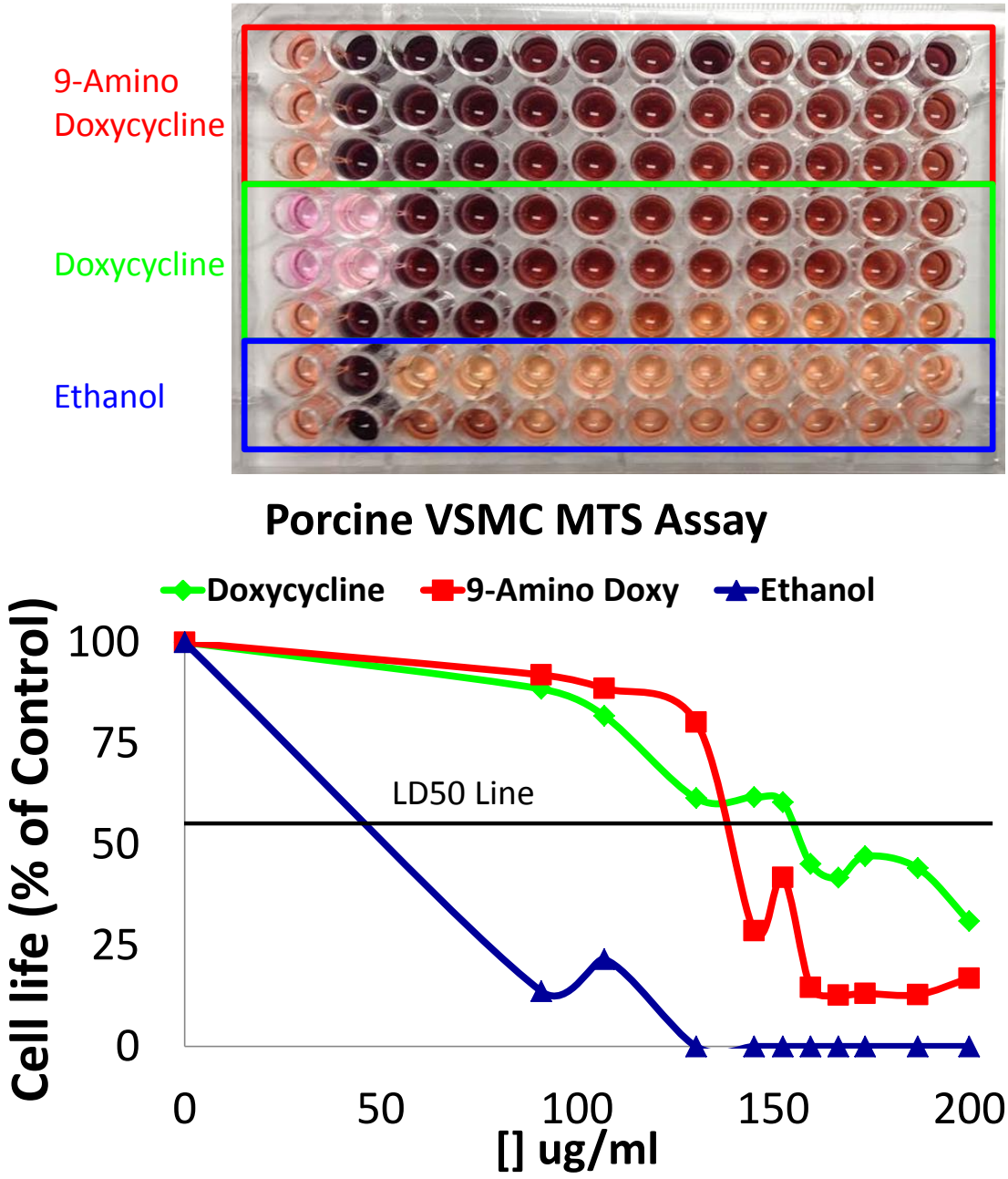

Figure 2.19: Top) Image of MTS assay containing 9-amino doxycycline, doxycycline, and ethanol in increasing concentrations from left to right, decreased absorbance

indicates decreased proliferation and increased toxicity. Bottom) The LD-50 denotes the concentration at which the dosage is lethal to 50% of the population.

2.3.4 Continuing Work

Initial work has shown the ability of the prodrug to release 9-amino doxycycline in the presence of activated MMPs, as well as the reduction of MMP activity *in vivo* with the addition of 9-amino doxycycline. Successful demonstration of MMP inhibition using the prodrug construct proposed herein will allow us to develop a second generation prodrug based on "self-immolative" dendrimer disassembly [154, 156, 157]. In these prodrugs, cleavage of a peptide linker by MMPs will result, through the cascade cleavage of a dendrimer structure, in the release of multiple doxycycline moieties.

2.4: Conclusion

In conclusion, this study, for the first time, quantified biaxial mechanical behavior of the ApoE$^{-/-}$ AngII infused model of aneurysm, while simultaneously quantifying changes in ECM microstructure at multiple time points. It also showed that massive remodeling of the microstructure of the aorta led to an altered mechanical response with the progression of disease in the ApoE$^{-/-}$ AngII infused mouse model of aneurysm. It was also shown that localized MMP activity, known to be elevated in aneurysmal and tissue undergoing remodeling, was able to be quantified spatially *ex vivo* in the ApoE$^{-/-}$ AngII infused model of AAA though the use of novel proteolytic FRET beacons and multiphoton imaging. Additionally, the development of a novel prodrug able to release a doxycycline derivative able to reduce MMP activity in the presence of elevated MMP activity shows potential in treating AAA development and possible progression. Future directions for this research would include *in vivo* animal studies (**Figure 2.20**) with an eye on eventual human trials.

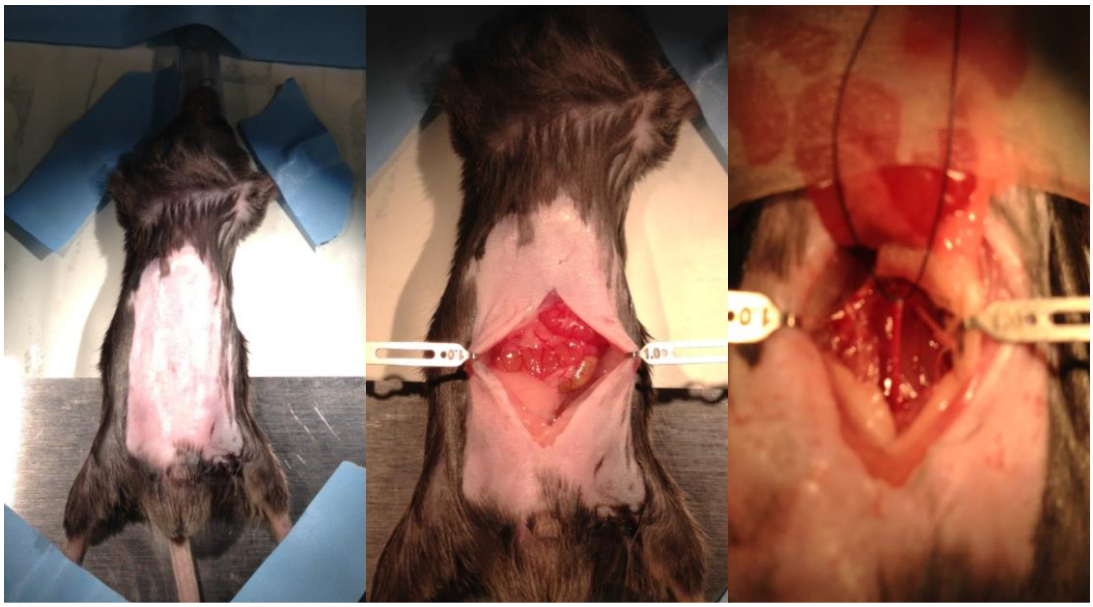

Figure 2.20: Serial images of a surgery that exposes and ligates the abdominal aorta of a mouse to gain access for imaging of the abdominal aorta *in vivo*.

REFERENCES

1. Vorp, D.A., Biomechanics of abdominal aortic aneurysm. J Biomech, 2007. 40(9): p. 1887-902.
2. Vorp, D.A. and J.P.V. Geest, *Biomechanical Determinants of Abdominal Aortic Aneurysm Rupture.* Arterioscler Thromb Vasc Biol, 2005. 25(8): p. 1558-1566.
3. Go, A.S., et al., *Heart disease and stroke statistics--2014 update: a report from the American Heart Association.* Circulation, 2014. 129(3): p. e28-e292.
4. Go, A.S., et al., *Heart disease and stroke statistics--2013 update: a report from the American Heart Association.* Circulation, 2013. 127(1): p. e6-e245.
5. Kurosawa, K., J.S. Matsumura, and D. Yamanouchi, *Current status of medical treatment for abdominal aortic aneurysm.* Circ J, 2013. 77(12): p. 2860-6.
6. Brewster, D.C., *Presidential address: what would you do if it were your father? Reflections on endovascular abdominal aortic aneurysm repair.* J Vasc Surg, 2001. 33(6): p. 1139-47.
7. Hovsepian, D.M., et al., *Elevated plasma levels of matrix metalloproteinase-9 in patients with abdominal aortic aneurysms: a circulating marker of degenerative aneurysm disease.* J Vasc Interv Radiol, 2000. 11(10): p. 1345-52.
8. Schlosser, F.J., et al., *Mortality after elective abdominal aortic aneurysm repair.* Ann Surg, 2010. 251(1): p. 158-64.
9. Sternbergh, W.C., 3rd and S.R. Money, *Hospital cost of endovascular versus open repair of abdominal aortic aneurysms: a multicenter study.* J Vasc Surg, 2000. 31(2): p. 237-44.
10. Cassis, L.A., et al., *ANG II infusion promotes abdominal aortic aneurysms independent of increased blood pressure in hypercholesterolemic mice.* Am J Physiol Heart Circ Physiol, 2009. 296(5): p. H1660-5.
11. Daugherty, A. and L. Cassis, *Angiotensin II-mediated development of vascular diseases.* Trends Cardiovasc Med, 2004. 14(3): p. 117-20.
12. Daugherty, A. and L.A. Cassis, *Mouse models of abdominal aortic aneurysms.* Arterioscler Thromb Vasc Biol, 2004. 24(3): p. 429-34.
13. Manning, M.W., et al., *Abdominal aortic aneurysms: fresh insights from a novel animal model of the disease.* Vasc Med, 2002. 7(1): p. 45-54.
14. Saraff, K., et al., *Aortic dissection precedes formation of aneurysms and atherosclerosis in angiotensin II-infused, apolipoprotein E-deficient mice.* Arterioscler Thromb Vasc Biol, 2003. 23(9): p. 1621-6.
15. Daugherty, A., M.W. Manning, and L.A. Cassis, *Angiotensin II promotes atherosclerotic lesions and aneurysms in apolipoprotein E-deficient mice.* J Clin Invest, 2000. 105(11): p. 1605-12.
16. Birkedal-Hansen, H., et al., *Matrix metalloproteinases: a review.* Crit Rev Oral Biol Med, 1993. 4(2): p. 197-250.
17. Page-McCaw, A., A.J. Ewald, and Z. Werb, *Matrix metalloproteinases and the regulation of tissue remodelling.* Nat Rev Mol Cell Biol, 2007. 8(3): p. 221-33.
18. Lu, H., et al., *Novel mechanisms of abdominal aortic aneurysms.* Curr Atheroscler Rep, 2012. 14(5): p. 402-12.

19. Baroneza, J.E., et al., *MMP-1 promoter genotype and haplotype association with posterior tibial tendinopathy.* Gene, 2014. 547(2): p. 334-337.
20. Cierna, Z., et al., *Matrix metalloproteinase 1 and circulating tumor cells in early breast cancer.* BMC cancer, 2014. 14(1): p. 472.
21. Garza-Gómez, J., et al., *An investigation into the MMP1 gene promoter region polymorphism–1607 2G with recessive dystrophic epidermolysis bullosa disease severity in northeastern Mexican patients.* International journal of dermatology, 2014. 53(8): p. 985-990.
22. Huang, S.F., et al., *The effect of a single nucleotide polymorphism in the matrix metalloproteinase-1 (MMP-1) promoter on force-induced MMP-1 expression in human periodontal ligament cells.* European journal of oral sciences, 2008. 116(4): p. 319-323.
23. DeCoux, A., et al., *Myocardial matrix metalloproteinase-2: inside out and upside down.* Journal of molecular and cellular cardiology, 2014. 77: p. 64-72.
24. Díaz, N. and D. Suárez, *Extensive Simulations of the Full-Length Matrix Metalloproteinase-2 Enzyme in a Prereactive Complex with a Collagen Triple-Helical Peptide.* Biochemistry, 2015. 54(5): p. 1243-1258.
25. Pereira, I.T., et al., *Fibronectin affects transient MMP2 gene expression through DNA demethylation changes in non-invasive breast cancer cell lines.* 2014.
26. Kizaki, K., et al., *Elevated oxidative stress monitored via the albumin-thiol redox state is correlated with matrix metalloproteinase-3 elevation in patients with rheumatoid arthritis.* Clinical laboratory, 2014. 61(1-2): p. 175-178.
27. Munshi, A., et al., *Association of tumor necrosis factor-α and matrix metalloproteinase-3 gene variants with stroke.* European Journal of Neurology, 2011. 18(8): p. 1053-1059.
28. Privalova, E., et al., *[Matrix metalloproteinases and hypertrophic cardiomyopathy]*. Kardiologiia, 2013. 54(5): p. 4-7.
29. Keles, D., et al., *Expression and activity levels of matrix metalloproteinase-7 and in situ localization of caseinolytic activity in colorectal cancer.* Clinical biochemistry, 2014. 47(13): p. 1265-1271.
30. Long, Z.-W., J.-L. Wang, and Y.-N. Wang, *Matrix metalloproteinase-7 mRNA and protein expression in gastric carcinoma: a meta-analysis.* Tumor Biology, 2014. 35(11): p. 11415-11426.
31. Wang, J., et al., *Inhibition of fibroblast growth factor receptor signaling impairs metastasis of hepatocellular carcinoma.* Tumor Biology, 2014. 35(11): p. 11005-11011.
32. Devarajan, P., et al., *Structure and expression of the cDNA encoding human neutrophil collagenase.* Blood, 1991. 77(12): p. 2731-2738.
33. Erkol, A., et al., *Relation of plasma matrix metalloproteinase-8 levels late after myocardial infarction with left ventricular volumes and ejection fraction.* Turk Kardiyol Dern Ars, 2013. 41(7): p. 617-624.

34. Hasty, K.A., et al., *Human neutrophil collagenase. A distinct gene product with homology to other matrix metalloproteinases.* Journal of Biological Chemistry, 1990. 265(20): p. 11421-11424.
35. Dubois, B., et al., *Gelatinase B deficiency protects against endotoxin shock.* European journal of immunology, 2002. 32(8): p. 2163-2171.
36. Forsyth, P., et al., *Gelatinase-A (MMP-2), gelatinase-B (MMP-9) and membrane type matrix metalloproteinase-1 (MT1-MMP) are involved in different aspects of the pathophysiology of malignant gliomas.* British journal of cancer, 1999. 79(11-12): p. 1828.
37. Opdenakker, G., et al., *Gelatinase B functions as regulator and effector in leukocyte biology.* Journal of leukocyte biology, 2001. 69(6): p. 851-859.
38. Jung, J., S. Warter, and Y. Rumpler. *Localization of stromelysin 2 gene to the q22. 3-23 region of chromosome 11 by in situ hybridization*. in *Annales de génétique*. 1990. Société d'édition de l'association d'enseignement médical des hôpitaux de Paris.
39. Mao, L., et al., *Role of matrix metalloproteinase-10 in the BMP-2 inducing osteoblastic differentiation.* Endocrine journal, 2013. 60(12): p. 1309-1319.
40. Martinez-Aguilar, E., et al., *Matrix metalloproteinase 10 is associated with disease severity and mortality in patients with peripheral arterial disease.* Journal of vascular surgery, 2015. 61(2): p. 428-435.
41. Vaalamo, M., et al., *Distinct expression profiles of stromelysin-2 (MMP-10), collagenase-3 (MMP-13), macrophage metalloelastase (MMP-12), and tissue inhibitor of metalloproteinases-3 (TIMP-3) in intestinal ulcerations.* The American journal of pathology, 1998. 152(4): p. 1005.
42. Zhang, G., et al., *Matrix metalloproteinase-10 promotes tumor progression through regulation of angiogenic and apoptotic pathways in cervical tumors.* BMC cancer, 2014. 14(1): p. 310.
43. Giambernardi, T.A., et al., *Overview of matrix metalloproteinase expression in cultured human cells.* Matrix Biology, 1998. 16(8): p. 483-496.
44. Kou, Y., et al., *Knockdown of MMP11 inhibits proliferation and invasion of gastric cancer cells.* International journal of immunopathology and pharmacology, 2013. 26(2): p. 361-370.
45. Luo, D., et al., *Alternative splicing and promoter usage generates an intracellular stromelysin 3 isoform directly translated as an active matrix metalloproteinase.* Journal of Biological Chemistry, 2002. 277(28): p. 25527-25536.
46. Curci, J.A., et al., *Expression and localization of macrophage elastase (matrix metalloproteinase-12) in abdominal aortic aneurysms.* J Clin Invest, 1998. 102(11): p. 1900-10.
47. Traylor, M., et al., *A novel MMP12 locus is associated with large artery atherosclerotic stroke using a genome-wide age-at-onset informed approach.* 2014.
48. Bhalla, G., et al., *Collagenase-3 expression in periapical lesions: an immunohistochemical study.* Biotechnic & Histochemistry, 2014. 89(6): p. 457-463.

49. Johansson, N., M. Ahonen, and V.-M. Kähäri, *Matrix metalloproteinases in tumor invasion.* Cellular and Molecular Life Sciences CMLS, 2000. 57(1): p. 5-15.
50. Abraham, R., et al., *Identification of MMP-15 as an anti-apoptotic factor in cancer cells.* Journal of Biological Chemistry, 2005. 280(40): p. 34123-34132.
51. Esparza, J., et al., *Fibronectin upregulates gelatinase B (MMP-9) and induces coordinated expression of gelatinase A (MMP-2) and its activator MT1-MMP (MMP-14) by human T lymphocyte cell lines. A process repressed through RAS/MAP kinase signaling pathways.* Blood, 1999. 94(8): p. 2754-2766.
52. Knäuper, V., et al., *Cellular mechanisms for human procollagenase-3 (MMP-13) activation Evidence that MT1-MMP (MMP-14) and gelatinase a (MMP-2) are able to generate active enzyme.* Journal of Biological Chemistry, 1996. 271(29): p. 17124-17131.
53. Lund, D.K., V. Mouly, and D. Cornelison, *MMP-14 is necessary but not sufficient for invasion of three-dimensional collagen by human muscle satellite cells.* American Journal of Physiology-Cell Physiology, 2014. 307(2): p. C140-C149.
54. Zucker, S., et al., *Tissue inhibitor of metalloproteinase-2 (TIMP-2) binds to the catalytic domain of the cell surface receptor, membrane type 1-matrix metalloproteinase 1 (MT1-MMP).* Journal of Biological Chemistry, 1998. 273(2): p. 1216-1222.
55. Konttinen, Y.T., et al., *Analysis of 16 different matrix metalloproteinases (MMP-1 to MMP-20) in the synovial membrane: different profiles in trauma and rheumatoid arthritis.* Annals of the rheumatic diseases, 1999. 58(11): p. 691-697.
56. Lee, M.-H. and G. Murphy, *Matrix metalloproteinases at a glance.* Journal of cell science, 2004. 117(18): p. 4015-4016.
57. Haeusler, G., et al., *Localization of matrix metalloproteinases,(MMPs) their tissue inhibitors, and vascular endothelial growth factor (VEGF) in growth plates of children and adolescents indicates a role for MMPs in human postnatal growth and skeletal maturation.* Calcified Tissue International, 2005. 76(5): p. 326-335.
58. Grant, G.M., et al., *Overview of expression of matrix metalloproteinases (MMP-17, MMP-18, and MMP-20) in cultured human cells.* Matrix biology, 1999. 18(2): p. 145-148.
59. Itoh, Y., et al., *Membrane type 4 matrix metalloproteinase (MT4-MMP, MMP-17) is a glycosylphosphatidylinositol-anchored proteinase.* Journal of Biological Chemistry, 1999. 274(48): p. 34260-34266.
60. Sohail, A., et al., *MT4-(MMP17) and MT6-MMP (MMP25), a unique set of membrane-anchored matrix metalloproteinases: properties and expression in cancer.* Cancer and Metastasis Reviews, 2008. 27(2): p. 289-302.
61. Cossins, J., et al., *Identification of MMP-18, a putative novel human matrix metalloproteinase.* Biochemical and biophysical research communications, 1996. 228(2): p. 494-498.
62. Bister, V.-O., et al., *Differential expression of three matrix metalloproteinases, MMP-19, MMP-26, and MMP-28, in normal and inflamed intestine and colon cancer.* Digestive diseases and sciences, 2004. 49(4): p. 653-661.

63. Djonov, V., et al., *MMP-19: cellular localization of a novel metalloproteinase within normal breast tissue and mammary gland tumours.* The Journal of pathology, 2001. 195(2): p. 147-155.
64. Impola, U., et al., *Expression of matrix metalloproteinase (MMP)-7 and MMP-13 and loss of MMP-19 and p16 are associated with malignant progression in chronic wounds.* British Journal of Dermatology, 2005. 152(4): p. 720-726.
65. Sedlacek, R., et al., *Matrix metalloproteinase MMP-19 (RASI-1) is expressed on the surface of activated peripheral blood mononuclear cells and is detected as an autoantigen in rheumatoid arthritis.* Immunobiology, 1998. 198(4): p. 408-423.
66. Llano, E., et al., *Identification and structural and functional characterization of human enamelysin (MMP-20).* Biochemistry, 1997. 36(49): p. 15101-15108.
67. Sulkala, M., et al., *The localization of matrix metalloproteinase-20 (MMP-20, enamelysin) in mature human teeth.* Journal of Dental Research, 2002. 81(9): p. 603-607.
68. Ahokas, K., et al., *Matrix metalloproteinases 21 and 26 are differentially expressed in esophageal squamous cell cancer.* Tumor Biology, 2006. 27(3): p. 133-141.
69. Ahokas, K., et al., *Matrix metalloproteinase-21, the human orthologue for XMMP, is expressed during fetal development and in cancer.* Gene, 2002. 301(1): p. 31-41.
70. Skoog, T., et al., *MMP-21 is expressed by macrophages and fibroblasts in vivo and in culture.* Experimental dermatology, 2006. 15(10): p. 775-783.
71. Suomela, S., et al., *Expression of MMP-10, MMP-21, MMP-26, and MMP-28 in Merkel cell carcinoma.* Virchows Archiv, 2009. 455(6): p. 495-503.
72. Leong, D.J., et al., *Matrix Metalloproteinases*, in *Encyclopedia of Exercise Medicine in Health and Disease*. 2012, Springer. p. 547-551.
73. Puente, X.S., et al., *Comparative genomic analysis of human and chimpanzee proteases.* Genomics, 2005. 86(6): p. 638-647.
74. Velasco, G., et al., *Cloning and characterization of human MMP-23, a new matrix metalloproteinase predominantly expressed in reproductive tissues and lacking conserved domains in other family members.* Journal of Biological Chemistry, 1999. 274(8): p. 4570-4576.
75. Galea, C.A., et al., *Domain structure and function of matrix metalloprotease 23 (MMP23): role in potassium channel trafficking.* Cellular and Molecular Life Sciences, 2014. 71(7): p. 1191-1210.
76. de la Peña, S., et al., *Expression of the matrix metalloproteases 2, 14, 24, and 25 and tissue inhibitor 3 as potential molecular markers in advanced human gastric cancer.* Disease markers, 2014. 2014.
77. Dzwonek, J., M. Rylski, and L. Kaczmarek, *Matrix metalloproteinases and their endogenous inhibitors in neuronal physiology of the adult brain.* FEBS letters, 2004. 567(1): p. 129-135.

78. Llano, E., et al., *Identification and characterization of human MT5-MMP, a new membrane-bound activator of progelatinase a overexpressed in brain tumors.* Cancer Research, 1999. 59(11): p. 2570-2576.
79. Pei, D., *Leukolysin/MMP25/MT6-MMP: a novel matrix metalloproteinase specifically expressed in the leukocyte lineage.* Cell research, 1999. 9(4): p. 291-303.
80. Starr, A.E., et al., *Biochemical Characterization and N-terminomics Analysis of Leukolysin, the Membrane-type 6 Matrix Metalloprotease (MMP25) chemokine and vimentin cleavages enhance cell migration and macrophage phagocytic activities.* Journal of Biological Chemistry, 2012. 287(16): p. 13382-13395.
81. Zhao, H., et al., *Identification and role of the homodimerization interface of the glycosylphosphatidylinositol-anchored membrane type 6 matrix metalloproteinase (MMP25).* Journal of Biological Chemistry, 2008. 283(50): p. 35023-35032.
82. Li, S., et al., *Maturation of Growth Differentiation Factor 15 in Human Placental Trophoblast Cells Depends on the Interaction With Matrix Metalloproteinase-26.* The Journal of Clinical Endocrinology & Metabolism, 2014. 99(11): p. E2277-E2287.
83. Marchenko, G.N. and A.Y. Strongin, *MMP-28, a new human matrix metalloproteinase with an unusual cysteine-switch sequence is widely expressed in tumors.* Gene, 2001. 265(1): p. 87-93.
84. Marchenko, N.D., G.N. Marchenko, and A.Y. Strongin, *Unconventional activation mechanisms of MMP-26, a human matrix metalloproteinase with a unique PHCGXXD cysteine-switch motif.* Journal of Biological Chemistry, 2002. 277(21): p. 18967-18972.
85. Pirilä, E., et al., *Collagenase-2 (MMP-8) and matrilysin-2 (MMP-26) expression in human wounds of different etiologies.* Wound repair and regeneration, 2007. 15(1): p. 47-57.
86. Cominelli, A., et al., *Matrix metalloproteinase-27 is expressed in CD163+/CD206+ M2 macrophages in the cycling human endometrium and in superficial endometriotic lesions.* Molecular human reproduction, 2014: p. gau034.
87. Cominelli, A., et al., *A Unique C-terminal Domain Allows Retention of Matrix Metalloproteinase-27 in the Endoplasmic Reticulum.* Traffic, 2014. 15(4): p. 401-417.
88. Nagase, H., R. Visse, and G. Murphy, *Structure and function of matrix metalloproteinases and TIMPs.* Cardiovascular research, 2006. 69(3): p. 562-573.
89. Illman, S.A., J. Lohi, and J. Keski-Oja, *Epilysin (MMP-28)–structure, expression and potential functions.* Experimental dermatology, 2008. 17(11): p. 897-907.
90. Lohi, J., et al., *Epilysin, a novel human matrix metalloproteinase (MMP-28) expressed in testis and keratinocytes and in response to injury.* Journal of Biological Chemistry, 2001. 276(13): p. 10134-10144.

91. Saarialho-Kere, U., et al., *Epilysin (MMP-28) expression is associated with cell proliferation during epithelial repair.* Journal of investigative dermatology, 2002. 119(1): p. 14-21.
92. Freestone, T., et al., *Inflammation and matrix metalloproteinases in the enlarging abdominal aortic aneurysm.* Arterioscler Thromb Vasc Biol, 1995. 15(8): p. 1145-51.
93. Davis, V., et al., *Matrix metalloproteinase-2 production and its binding to the matrix are increased in abdominal aortic aneurysms.* Arterioscler Thromb Vasc Biol, 1998. 18(10): p. 1625-33.
94. Thompson, R.W., et al., *Production and localization of 92-kilodalton gelatinase in abdominal aortic aneurysms. An elastolytic metalloproteinase expressed by aneurysm-infiltrating macrophages.* J Clin Invest, 1995. 96(1): p. 318-26.
95. Longo, G.M., et al., *Matrix metalloproteinases 2 and 9 work in concert to produce aortic aneurysms.* J Clin Invest, 2002. 110(5): p. 625-32.
96. Crowther, M., et al., *Increased matrix metalloproteinase 2 expression in vascular smooth muscle cells cultured from abdominal aortic aneurysms.* J Vasc Surg, 2000. 32(3): p. 575-83.
97. Golub, L.M., et al., *A non-antimicrobial tetracycline inhibits gingival matrix metalloproteinases and bone loss in Porphyromonas gingivalis-induced periodontitis in rats.* Ann N Y Acad Sci, 1994. 732: p. 96-111.
98. Golub, L.M., et al., *Minocycline reduces gingival collagenolytic activity during diabetes. Preliminary observations and a proposed new mechanism of action.* J Periodontal Res, 1983. 18(5): p. 516-26.
99. Greenwald, R.A., *Treatment of destructive arthritic disorders with MMP inhibitors. Potential role of tetracyclines.* Ann N Y Acad Sci, 1994. 732: p. 181-98.
100. Uitto, V.J., et al., *Doxycycline and chemically modified tetracyclines inhibit gelatinase A (MMP-2) gene expression in human skin keratinocytes.* Ann N Y Acad Sci, 1994. 732: p. 140-51.
101. Petrinec, D., et al., *Doxycycline inhibition of aneurysmal degeneration in an elastase-induced rat model of abdominal aortic aneurysm: preservation of aortic elastin associated with suppressed production of 92 kD gelatinase.* J Vasc Surg, 1996. 23(2): p. 336-46.
102. Curci, J.A., et al., *Pharmacologic suppression of experimental abdominal aortic aneurysms: acomparison of doxycycline and four chemically modified tetracyclines.* J Vasc Surg, 1998. 28(6): p. 1082-93.
103. Manning, M.W., L.A. Cassis, and A. Daugherty, *Differential effects of doxycycline, a broad-spectrum matrix metalloproteinase inhibitor, on angiotensin II-induced atherosclerosis and abdominal aortic aneurysms.* Arterioscler Thromb Vasc Biol, 2003. 23(3): p. 483-8.
104. Pyo, R., et al., *Targeted gene disruption of matrix metalloproteinase-9 (gelatinase B) suppresses development of experimental abdominal aortic aneurysms.* J Clin Invest, 2000. 105(11): p. 1641-9.

105. Vinh, A., et al., *A novel histone deacetylase inhibitor reduces abdominal aortic aneurysm formation in angiotensin II-infused apolipoprotein E-deficient mice.* J Vasc Res, 2008. 45(2): p. 143-52.
106. Baxter, B.T., et al., *Prolonged administration of doxycycline in patients with small asymptomatic abdominal aortic aneurysms: report of a prospective (Phase II) multicenter study.* J Vasc Surg, 2002. 36(1): p. 1-12.
107. Mosorin, M., et al., *Use of doxycycline to decrease the growth rate of abdominal aortic aneurysms: a randomized, double-blind, placebo-controlled pilot study.* J Vasc Surg, 2001. 34(4): p. 606-10.
108. Thompson, R.W. and B.T. Baxter, *MMP inhibition in abdominal aortic aneurysms. Rationale for a prospective randomized clinical trial.* Ann N Y Acad Sci, 1999. 878: p. 159-78.
109. Bartoli, M.A., et al., *Localized administration of doxycycline suppresses aortic dilatation in an experimental mouse model of abdominal aortic aneurysm.* Ann Vasc Surg, 2006. 20(2): p. 228-36.
110. Prall, A.K., et al., *Doxycycline in patients with abdominal aortic aneurysms and in mice: comparison of serum levels and effect on aneurysm growth in mice.* J Vasc Surg, 2002. 35(5): p. 923-9.
111. Haskett, D., et al., *Progressive alterations in microstructural organization and biomechanical response in the ApoE mouse model of aneurysm.* Biomatter, 2013. 3(3).
112. Lederle, F.A., *The rise and fall of abdominal aortic aneurysm.* Circulation, 2011. 124(10): p. 1097-9.
113. Dua, A., et al., *Epidemiology of aortic aneurysm repair in the United States from 2000 to 2010.* J Vasc Surg, 2014. 59(6): p. 1512-7.
114. Roger, V.L., et al., *Heart disease and stroke statistics--2012 update: a report from the American Heart Association.* Circulation, 2012. 125(1): p. e2-e220.
115. Weintraub, N.L., *Understanding abdominal aortic aneurysm.* N Engl J Med, 2009. 361(11): p. 1114-6.
116. Kent, K.C., et al., *Analysis of risk factors for abdominal aortic aneurysm in a cohort of more than 3 million individuals.* J Vasc Surg, 2010. 52(3): p. 539-48.
117. Daugherty, A., D.L. Rateri, and L.A. Cassis, *Role of the renin-angiotensin system in the development of abdominal aortic aneurysms in animals and humans.* Ann N Y Acad Sci, 2006. 1085: p. 82-91.
118. Baxter, B.T., M.C. Terrin, and R.L. Dalman, *Medical management of small abdominal aortic aneurysms.* Circulation, 2008. 117(14): p. 1883-9.
119. Thompson, R.W., et al., *Pathophysiology of abdominal aortic aneurysms: insights from the elastase-induced model in mice with different genetic backgrounds.* Ann N Y Acad Sci, 2006. 1085: p. 59-73.
120. Thompson, R.W., P.J. Geraghty, and J.K. Lee, *Abdominal aortic aneurysms: basic mechanisms and clinical implications.* Curr Probl Surg, 2002. 39(2): p. 110-230.
121. Frangioni, J.V., *In vivo near-infrared fluorescence imaging.* Curr Opin Chem Biol, 2003. 7(5): p. 626-34.

122. Miyama, N., et al., *Bioluminescence and magnetic resonance imaging of macrophage homing to experimental abdominal aortic aneurysms.* Mol Imaging, 2012. 11(2): p. 126-34.
123. Ramaswamy, A.K., et al., *Molecular imaging of experimental abdominal aortic aneurysms.* ScientificWorldJournal, 2013. 2013: p. 973150.
124. McIntyre, J.O., et al., *Development of a novel fluorogenic proteolytic beacon for in vivo detection and imaging of tumour-associated matrix metalloproteinase-7 activity.* Biochem J, 2004. 377(Pt 3): p. 617-28.
125. McIntyre, J.O. and L.M. Matrisian, *Optical proteolytic beacons for in vivo detection of matrix metalloproteinase activity.* Methods Mol Biol, 2009. 539: p. 155-74.
126. McIntyre, J.O. and L.M. Matrisian, *Molecular imaging of proteolytic activity in cancer.* J Cell Biochem, 2003. 90(6): p. 1087-97.
127. McIntyre, J.O., R.L. Scherer, and L.M. Matrisian, *Near-infrared optical proteolytic beacons for in vivo imaging of matrix metalloproteinase activity.* Methods Mol Biol, 2010. 622: p. 279-304.
128. Xiong, W., et al., *Doxycycline delays aneurysm rupture in a mouse model of Marfan syndrome.* J Vasc Surg, 2008. 47(1): p. 166-72; discussion 172.
129. Scherer, R.L., et al., *Optical imaging of matrix metalloproteinase-7 activity in vivo using a proteolytic nanobeacon.* Mol Imaging, 2008. 7(3): p. 118-31.
130. Keyes, J.T., et al., *Comparisons of planar and tubular biaxial tensile testing protocols of the same porcine coronary arteries.* Ann Biomed Eng, 2013. 41(7): p. 1579-91.
131. Utzinger, U., et al., *Large-scale time series microscopy of neovessel growth during angiogenesis.* Angiogenesis, 2015.
132. Bal, U., et al., *Intravital confocal and two-photon imaging of dual-color cells and extracellular matrix mimics.* Microsc Microanal, 2013. 19(1): p. 201-12.
133. Ray, J.L., et al., *Isolation of vascular smooth muscle cells from a single murine aorta.* Methods Cell Sci, 2001. 23(4): p. 185-8.
134. Piedrahita, J.A., et al., *Generation of mice carrying a mutant apolipoprotein E gene inactivated by gene targeting in embryonic stem cells.* Proc Natl Acad Sci U S A, 1992. 89(10): p. 4471-5.
135. Eagleton, M.J., et al., *Early increased MT1-MMP expression and late MMP-2 and MMP-9 activity during Angiotensin II induced aneurysm formation.* J Surg Res, 2006. 135(2): p. 345-51.
136. Guo, R.W., et al., *Angiotensin II induces matrix metalloproteinase-9 expression via a nuclear factor-kappaB-dependent pathway in vascular smooth muscle cells.* Regul Pept, 2008. 147(1-3): p. 37-44.
137. Luchtefeld, M., et al., *Angiotensin II induces MMP-2 in a p47phox-dependent manner.* Biochem Biophys Res Commun, 2005. 328(1): p. 183-8.
138. Acharya, M.R., et al., *Chemically modified tetracyclines as inhibitors of matrix metalloproteinases.* Drug Resist Updat, 2004. 7(3): p. 195-208.

139. Franco, C., et al., *Doxycycline alters vascular smooth muscle cell adhesion, migration, and reorganization of fibrillar collagen matrices.* Am J Pathol, 2006. 168(5): p. 1697-709.
140. Grandas, O.H., et al., *Regulation of vascular smooth muscle cell expression and function of matrix metalloproteinases is mediated by estrogen and progesterone exposure.* J Vasc Surg, 2009. 49(1): p. 185-91.
141. Leber, T.M. and F.R. Balkwill, *Zymography: a single-step staining method for quantitation of proteolytic activity on substrate gels.* Anal Biochem, 1997. 249(1): p. 24-8.
142. Mannello, F. and M. Sebastiani, *Zymographic analyses and measurement of matrix metalloproteinase-2 and -9 in nipple aspirate fluids.* Clin Chem, 2003. 49(9): p. 1546-50.
143. Troeberg, L. and H. Nagase, *Measurement of matrix metalloproteinase activities in the medium of cultured synoviocytes using zymography.* Methods Mol Biol, 2003. 225: p. 77-87.
144. Haskett, D., et al., *The effects of angiotensin II on the coupled microstructural and biomechanical response of C57BL/6 mouse aorta.* J Biomech, 2011.
145. Keyes, J.T., et al., *Adaptation of a planar microbiaxial optomechanical device for the tubular biaxial microstructural and macroscopic characterization of small vascular tissues.* J Biomech Eng, 2011. 133(7): p. 075001.
146. Ardila, D.C., et al., *TGFbeta2 differentially modulates smooth muscle cell proliferation and migration in electrospun gelatin-fibrinogen constructs.* Biomaterials, 2015. 37: p. 164-73.
147. Xie, X., et al., *Doxycycline does not influence established abdominal aortic aneurysms in angiotensin II-infused mice.* PLoS One, 2012. 7(9): p. e46411.
148. Leahy, A.A., et al., *Analysis of the trajectory of osteoarthritis development in a mouse model by serial near-infrared fluorescence imaging of matrix metalloproteinase activities.* Arthritis Rheumatol, 2015. 67(2): p. 442-53.
149. Lin, S.A., et al., *Optical imaging biomarkers of drug-induced vascular injury.* Mol Imaging, 2015. 14.
150. Pivoraite, U., et al., *Exosomes from Human Dental Pulp Stem Cells Suppress Carrageenan-Induced Acute Inflammation in Mice.* Inflammation, 2015.
151. Scherer, R.L., J.O. McIntyre, and L.M. Matrisian, *Imaging matrix metalloproteinases in cancer.* Cancer Metastasis Rev, 2008. 27(4): p. 679-90.
152. Haskett, D., et al., *Altered tissue behavior of a non-aneurysmal descending thoracic aorta in the mouse model of Marfan syndrome.* Cell Tissue Res, 2012. 347(1): p. 267-77.
153. McCarthy, T.D., et al., *Dendrimers as drugs: discovery and preclinical and clinical development of dendrimer-based microbicides for HIV and STI prevention.* Mol Pharm, 2005. 2(4): p. 312-8.
154. McGrath, D.V., *Dendrimer disassembly as a new paradigm for the application of dendritic structures.* Mol Pharm, 2005. 2(4): p. 253-63.

155. Megens, R.T., et al., *Imaging collagen in intact viable healthy and atherosclerotic arteries using fluorescently labeled CNA35 and two-photon laser scanning microscopy.* Mol Imaging, 2007. 6(4): p. 247-60.
156. Li, S., et al., *Dendrimer disassembly by benzyl ether depolymerization.* J Am Chem Soc, 2003. 125(35): p. 10516-7.
157. Szalai, M.L., R.M. Kevwitch, and D.V. McGrath, *Geometric disassembly of dendrimers: dendritic amplification.* J Am Chem Soc, 2003. 125(51): p. 15688-9.
158. Fillinger, M.F., et al., *In vivo analysis of mechanical wall stress and abdominal aortic aneurysm rupture risk.* J Vasc Surg, 2002. 36(3): p. 589-97.
159. Raghavan, M.L., et al., *Regional distribution of wall thickness and failure properties of human abdominal aortic aneurysm.* J Biomech, 2006. 39(16): p. 3010-6.
160. Raghavan, M.L. and D.A. Vorp, *Toward a biomechanical tool to evaluate rupture potential of abdominal aortic aneurysm: identification of a finite strain constitutive model and evaluation of its applicability.* J Biomech, 2000. 33(4): p. 475-82.
161. Valencia, A.A., et al., *Blood flow dynamics in saccular aneurysm models of the basilar artery.* J Biomech Eng, 2006. 128(4): p. 516-26.
162. Vande Geest, J.P., et al., *A biomechanics-based rupture potential index for abdominal aortic aneurysm risk assessment: demonstrative application.* Ann N Y Acad Sci, 2006. 1085: p. 11-21.
163. Vande Geest, J.P., et al., *Towards a noninvasive method for determination of patient-specific wall strength distribution in abdominal aortic aneurysms.* Ann Biomed Eng, 2006. 34(7): p. 1098-106.
164. Brophy, C.M., J.E. Tilson, and M.D. Tilson, *Propranolol stimulates the crosslinking of matrix components in skin from the aneurysm-prone blotchy mouse.* J Surg Res, 1989. 46(4): p. 330-2.
165. Liao, S., et al., *Suppression of experimental abdominal aortic aneurysms in the rat by treatment with angiotensin-converting enzyme inhibitors.* J Vasc Surg, 2001. 33(5): p. 1057-64.
166. Meijer, C.A., et al., *Doxycycline for stabilization of abdominal aortic aneurysms: a randomized trial.* Ann Intern Med, 2013. 159(12): p. 815-23.
167. Steinmetz, E.F., et al., *Treatment with simvastatin suppresses the development of experimental abdominal aortic aneurysms in normal and hypercholesterolemic mice.* Ann Surg, 2005. 241(1): p. 92-101.
168. Dodd, B.R. and R.A. Spence, *Doxycycline inhibition of abdominal aortic aneurysm growth: a systematic review of the literature.* Curr Vasc Pharmacol, 2011. 9(4): p. 471-8.
169. Lindeman, J.H., et al., *Clinical trial of doxycycline for matrix metalloproteinase-9 inhibition in patients with an abdominal aneurysm: doxycycline selectively depletes aortic wall neutrophils and cytotoxic T cells.* Circulation, 2009. 119(16): p. 2209-16.

170. Hu, Z., et al., *Discovery of matrix metalloproteases selective and activated peptide-doxorubicin prodrugs as anti-tumor agents.* Bioorg Med Chem Lett, 2010. 20(3): p. 853-6.
171. Sellers, A., et al., *Evidence that latent collagenases are enzyme-inhibitor complexes.* Biochem J, 1977. 163(2): p. 303-7.
172. Haskett, D., et al., *The effects of angiotensin II on the coupled microstructural and biomechanical response of C57BL/6 mouse aorta.* J Biomech. 45(5): p. 772-9.
173. Vande Geest, J.P., M.S. Sacks, and D.A. Vorp, *The effects of aneurysm on the biaxial mechanical behavior of human abdominal aorta.* J Biomech, 2006. 39(7): p. 1324-34.
174. Choi, H., R.C. Tostes, and R.C. Webb, *Mitochondrial aldehyde dehydrogenase prevents ROS-induced vascular contraction in angiotensin-II hypertensive mice.* J Am Soc Hypertens.
175. Intengan, H.D. and E.L. Schiffrin, *Vascular remodeling in hypertension: roles of apoptosis, inflammation, and fibrosis.* Hypertension, 2001. 38(3 Pt 2): p. 581-7.
176. Sparks, M.A., et al., *Angiotensin II type 1A receptors in vascular smooth muscle cells do not influence aortic remodeling in hypertension.* Hypertension. 57(3): p. 577-85.
177. Cassis, L.A., et al., *Aldosterone does not mediate angiotensin II-induced atherosclerosis and abdominal aortic aneurysms.* Br J Pharmacol, 2005. 144(3): p. 443-8.
178. Henriques, T.A., et al., *Orchidectomy, but not ovariectomy, regulates angiotensin II-induced vascular diseases in apolipoprotein E-deficient mice.* Endocrinology, 2004. 145(8): p. 3866-72.
179. Goergen, C.J., et al., *Influences of aortic motion and curvature on vessel expansion in murine experimental aneurysms.* Arterioscler Thromb Vasc Biol. 31(2): p. 270-9.
180. Baek, S., K.R. Rajagopal, and J.D. Humphrey, *A theoretical model of enlarging intracranial fusiform aneurysms.* J Biomech Eng, 2006. 128(1): p. 142-9.
181. Eberth, J.F., et al., *Mechanics of carotid arteries in a mouse model of Marfan Syndrome.* Ann Biomed Eng, 2009. 37(6): p. 1093-104.
182. Humphrey, J.D. and K.R. Rajagopal, *A constrained mixture model for arterial adaptations to a sustained step change in blood flow.* Biomech Model Mechanobiol, 2003. 2(2): p. 109-26.
183. Keyes, J.T., et al., *Adaptation of a two-photon-microscope-interfacing planar biaxial device for the microstructural characterization of small tubular tissue specimens.* Journal of Biomechanical Engineering, 2011. Jul; 133(7):075001.
184. Peti-Peterdi, J. and P.D. Bell, *Confocal and two-photon microscopy.* Methods Mol Med, 2003. 86: p. 129-38.
185. Keyes, J.T., et al., *Design and Demonstration of a Microbiaxial Optomechanical Device for Multiscale Characterization of Soft Biological Tissues with Two-Photon Microscopy.* Microsc Microanal: p. 1-9.

186. Kirkpatrick, N.D., et al., *In vitro model for endogenous optical signatures of collagen.* J Biomed Opt, 2006. 11(5): p. 054021.
187. Schulze-Bauer, C.A., P. Regitnig, and G.A. Holzapfel, *Mechanics of the human femoral adventitia including the high-pressure response.* Am J Physiol Heart Circ Physiol, 2002. 282(6): p. H2427-40.
188. Gleason, R.L., E. Wilson, and J.D. Humphrey, *Biaxial biomechanical adaptations of mouse carotid arteries cultured at altered axial extension.* J Biomech, 2007. 40(4): p. 766-76.
189. Humphrey, J.D., et al., *Fundamental role of axial stress in compensatory adaptations by arteries.* J Biomech, 2009. 42(1): p. 1-8.
190. Debes, J.C. and Y.C. Fung, *Biaxial mechanics of excised canine pulmonary arteries.* Am J Physiol, 1995. 269(2 Pt 2): p. H433-42.
191. Fung, Y., *Biomechanics: Mechanical Properties of Living Tissues*. 2nd ed. 1993, New York: Springer.
192. Vande Geest, J.P., M.S. Sacks, and D.A. Vorp, *Age dependency of the biaxial biomechanical behavior of human abdominal aorta.* J Biomech Eng, 2004. 126(6): p. 815-22.
193. Fung, Y.C. and S.Q. Liu, *Determination of the mechanical properties of the different layers of blood vessels in vivo.* Proc Natl Acad Sci U S A, 1995. 92(6): p. 2169-73.
194. Benetos, A., et al., *Influence of angiotensin-converting enzyme and angiotensin II type 1 receptor gene polymorphisms on aortic stiffness in normotensive and hypertensive patients.* Circulation, 1996. 94(4): p. 698-703.
195. Benetos, A., et al., *Arterial alterations with aging and high blood pressure. A noninvasive study of carotid and femoral arteries.* Arterioscler Thromb, 1993. 13(1): p. 90-7.
196. Benetos, A., et al., *Influence of angiotensin II type 1 receptor polymorphism on aortic stiffness in never-treated hypertensive patients.* Hypertension, 1995. 26(1): p. 44-7.
197. Lajemi, M., et al., *Angiotensin II type 1 receptor-153A/G and 1166A/C gene polymorphisms and increase in aortic stiffness with age in hypertensive subjects.* J Hypertens, 2001. 19(3): p. 407-13.
198. Boulesteix, T., et al., *Micrometer scale ex vivo multiphoton imaging of unstained arterial wall structure.* Cytometry A, 2006. 69(1): p. 20-6.
199. Werkmeister, E., et al., *Multiphoton microscopy for blood vessel imaging: new non-invasive tools (Spectral, SHG, FLIM).* Clin Hemorheol Microcirc, 2007. 37(1-2): p. 77-88.
200. Zoumi, A., et al., *Imaging coronary artery microstructure using second-harmonic and two-photon fluorescence microscopy.* Biophys J, 2004. 87(4): p. 2778-86.
201. Zoumi, A., A. Yeh, and B.J. Tromberg, *Imaging cells and extracellular matrix in vivo by using second-harmonic generation and two-photon excited fluorescence.* Proc Natl Acad Sci U S A, 2002. 99(17): p. 11014-9.

202. Schenke-Layland, K., et al., *Imaging of cardiovascular structures using near-infrared femtosecond multiphoton laser scanning microscopy.* J Biomed Opt, 2005. 10(2): p. 024017.
203. Gleason, R.L., et al., *A multiaxial computer-controlled organ culture and biomechanical device for mouse carotid arteries.* J Biomech Eng, 2004. 126(6): p. 787-95.
204. Keyes, J.T., et al., *Design and Demonstration of a Microbiaxial Optomechanical Device for Multiscale Characterization of Soft Biological Tissues with Two-Photon Microscopy.* Microsc Microanal, 2011: p. 1-9.
205. Zaucha, M.T., et al., *A novel cylindrical biaxial computer-controlled bioreactor and biomechanical testing device for vascular tissue engineering.* Tissue Eng Part A, 2009. 15(11): p. 3331-40.
206. Gasser, T.C., R.W. Ogden, and G.A. Holzapfel, *Hyperelastic modelling of arterial layers with distributed collagen fibre orientations.* J R Soc Interface, 2006. 3(6): p. 15-35.
207. Grootenboer, N., et al., *Epidemiology, aetiology, risk of rupture and treatment of abdominal aortic aneurysms: does sex matter?* Eur J Vasc Endovasc Surg, 2009. 38(3): p. 278-84.
208. Hans, C.P., et al., *Inhibition of Notch1 signaling reduces abdominal aortic aneurysm in mice by attenuating macrophage-mediated inflammation.* Arterioscler Thromb Vasc Biol. 32(12): p. 3012-23.
209. Iida, Y., et al., *Efficacy and mechanism of angiotensin II receptor blocker treatment in experimental abdominal aortic aneurysms.* PLoS One. 7(12): p. e49642.
210. Remus, E.W., et al., *The role of lysyl oxidase family members in the stabilization of abdominal aortic aneurysms.* Am J Physiol Heart Circ Physiol. 303(8): p. H1067-75.
211. Yao, Y., et al., *In vivo imaging of macrophages during the early-stages of abdominal aortic aneurysm using high resolution MRI in ApoE mice.* PLoS One. 7(3): p. e33523.
212. Ford, M.D., et al., *Hemodynamics of the mouse abdominal aortic aneurysm.* J Biomech Eng. 133(12): p. 121008.
213. Goergen, C.J., et al., *In vivo quantification of murine aortic cyclic strain, motion, and curvature: implications for abdominal aortic aneurysm growth.* J Magn Reson Imaging. 32(4): p. 847-58.
214. Collins, M.J., et al., *Mechanical properties of suprarenal and infrarenal abdominal aorta: implications for mouse models of aneurysms.* Med Eng Phys. 33(10): p. 1262-9.
215. Haskett, D., et al., *The effects of angiotensin II on the coupled microstructural and biomechanical response of C57BL/6 mouse aorta.* J Biomech, 2011. 45(5): p. 772-9.
216. Barisione, C., et al., *Rapid dilation of the abdominal aorta during infusion of angiotensin II detected by noninvasive high-frequency ultrasonography.* J Vasc Surg, 2006. 44(2): p. 372-6.

217. Keyes, J.T., et al., *Design and demonstration of a microbiaxial optomechanical device for multiscale characterization of soft biological tissues with two-photon microscopy.* Microsc Microanal, 2011. 17(2): p. 167-75.
218. Fornasa, G., et al., *A CD31-derived peptide prevents angiotensin II-induced atherosclerosis progression and aneurysm formation.* Cardiovasc Res. 94(1): p. 30-7.
219. Yang, L., et al., *Role of Kruppel-Like Factor 2 and Protease-Activated Receptor-1 in Vulnerable Plaques of ApoE(-/-) Mice and Intervention With Statin.* Can J Cardiol, 2013.
220. Deguchi, J.O., et al., *Genetically engineered resistance for MMP collagenases promotes abdominal aortic aneurysm formation in mice infused with angiotensin II.* Lab Invest, 2009. 89(3): p. 315-26.
221. Sheth, R.A., M. Maricevich, and U. Mahmood, *In vivo optical molecular imaging of matrix metalloproteinase activity in abdominal aortic aneurysms correlates with treatment effects on growth rate.* Atherosclerosis, 2010. 212(1): p. 181-7.
222. Fujikura, K., et al., *A novel noninvasive technique for pulse-wave imaging and characterization of clinically-significant vascular mechanical properties in vivo.* Ultrason Imaging, 2007. 29(3): p. 137-54.
223. Lindeman, J.H., et al., *Distinct defects in collagen microarchitecture underlie vessel-wall failure in advanced abdominal aneurysms and aneurysms in Marfan syndrome.* Proc Natl Acad Sci U S A, 2010. 107(2): p. 862-5.
224. Schriefl, A.J., et al., *Remodeling of intramural thrombus and collagen in an Ang-II infusion ApoE-/- model of dissecting aortic aneurysms.* Thromb Res. 130(3): p. e139-46.

APPENDIX A: The Effects of Angiotensin II on the Coupled Microstructural and Biomechanical Response of C57BL/6 Mouse Aorta

Darren Haskett[1] MS, Erin Speicher[2], Marie Fouts[3], Doug Larson[1,4], Mohamad Azhar[5,6] PhD, Urs Utzinger[1,5] PhD, Jonathan Vande Geest[1,2,5] PhD

1. Graduate Interdisciplinary Program of Biomedical Engineering

2. Department of Aerospace and Mechanical Engineering

3. Department of Medical Pharmacology

4. Department of Surgery, Sarver Heart Center

5. BIO5 Institute

6. Department of Cellular and Molecular Medicine

The University of Arizona

Tucson, AZ

Corresponding Author

Jonathan P. Vande Geest, PhD

The University of Arizona

Aerospace and Mechanical Engineering

Graduate Interdisciplinary Program in Biomedical Engineering

BIO5 Institute

1130 N. Mountain

PO Box 210119

Tucson, AZ 85721-0119

Phone: (520) 621-2514

Fax: (520) 621-8191

Email: jpv1@email.arizona.edu

Journal of biomechanics. 2012; 45(5):772-9

A.1 Abstract

Rationale: Abdominal aortic aneurysm (AAA) is a complex disease that leads to a localized dilation of the infrarenal aorta, the rupture of which is associated with significant morbidity and mortality. Animal models of AAA can be used to study how changes in the microstructural and biomechanical behavior of aortic tissues develop as disease progresses in these animals. We chose here to investigate the effect of angiotensin II (AngII) in C57BL/6 mice as a first step towards understanding how such changes occur in the established *ApoE*$^{-/-}$ AngII infused mouse model of AAA.

Objective: The objective of this study was to utilize a recently developed device in our laboratory to determine how the microstructural and biomechanical properties of AngII-infused C57BL/6 wildtype mouse aorta change following 14 days of AngII infusion.

Methods: C57BL/6 wildtype mice were infused with either saline or AngII for 14 days. Aortas were excised and tested using a device capable of simultaneously characterizing the biaxial mechanical response and load-dependent (unfixed, unfrozen) extracellular matrix organization of mouse aorta (using multiphoton microscopy). Peak strains and stiffness values were compared across experimental groups, and both datasets were fit to a Fung-type constitutive model. The mean mode and full width at half maximum (FWHM) of fiber histograms from two photon microscopy were quantified in order to assess the preferred fiber distribution and degree of fiber splay, respectively.

Results: The axial stiffness of all mouse aorta was found to be an order of magnitude larger than the circumferential stiffness. The aortic diameter was found to be significantly increased for the AngII infused mice as compared to saline infused control ($p=0.026$). Aneurysm, defined as a percent increase in maximum diameter of 30% (defined with respect to saline control), was found in 3 of the 6 AngII infused mice. These three mice displayed adventitial collagen that lacked characteristic fiber crimp. The biomechanical response in the AngII infused mice showed significantly reduced circumferential

compliance. We also noticed that the ability of the adventitial collagen fibers in AngII infused mice to disperse in reaction to circumferential loading was suppressed.

Conclusions: Collagen remodeling is present following 14 days of AngII infusion in C57BL/6 mice. Aneurysmal development occurred in 50% of our AngII infused mice, and these dilatations were accompanied with adventitial collagen remodeling and decreased circumferential compliance.

Key Words: aorta, aneurysm, mouse, microstructure, multiphoton, two-photon, AngII, angiotensin

A.2 Introduction

Abdominal aortic aneurysm (AAA) is a complex disease manifesting in a localized dilation of the infrarenal aorta, the rupture of which is associated with significant morbidity and mortality. It is known that aneurysmal tissue is remodeled in the disease process in humans [1] and that such reorganization leads to alterations in mechanical properties [173]. Since AAA disease is complex, multifactorial, and not fully understood, there is a need to understand the underlying mechanisms of disease initiation, how they develop, and how they lead to expansion and rupture. Animal models of aneurysmal disease can be useful for studying alterations during disease development (e.g., in the tissue's mechanical response) and also for studying novel and new endovascular treatments.

The study of the formation and progression of vascular disease has also focused on quantifying any changes observed in fiber realignment and altered mechanical properties. Of the many methods developed in order to conduct such studies, the infusion of angiotensin II (AngII) has become prevalent as it is known to induce many physiological responses, including vasoconstriction, aldosterone release, water and sodium retension, and elevated sympathetic activity [11, 174]. In addition, AngII has been found to directly contribute to vascular smooth muscle cell growth and vessel remodeling [174-176]. Thus it is of importance to determine how vessel remodeling is initiated and develops into vascular disease using AngII infused animals.

Infusing *ApoE*$^{-/-}$ mice with AngII using subcutaneously implanted Alzet pumps was found to not only affect atherosclerotic development, but also correspond to aneurysmal development in the abdominal region of the aorta. Described by Daugherty et al., the model employs AngII infusion of *ApoE*$^{-/-}$ mice on a C57BL/6 genetic background [15]. Analysis of the abdominal region of the aorta revealed luminal dilation, medial degeneration, and the presence of thrombotic material, all of which are features present in human AAA and as such should also be seen in an appropriate animal model of this disease [13]. For this reason, the AngII infused *ApoE*$^{-/-}$ model has also been used to study the effects of different pharmacological treatments of AAA [103, 177, 178]. However, much of the work surrounding the study of this mouse model has been based on a categorical approach and

although this does help in classifying the disease, it does not quantitatively describe aneurysmal disease progression as this disease progresses over time [179].

One metric of quantifying disease progression has been determining the mechanical stresses occurring within the vessel, since studying the stress associated with arterial behavior has often been connected with the growth and remodeling that may act as either an indicator or initiator of disease [180-182]. Constitutive modeling of arterial tissue is an important tool for biomechanical studies of AAA disease as it will elucidate how differences in stress might correlate with the state of the extracellular matrix, and thus how changes in mechanical response may predict or correlate to a diseased state.

The long term goal of our group is to determine the changes in biomechanical response and associated alterations in microstructure in the AngII infused *ApoE*$^{-/-}$ model of aneurysm as it develops over time. We chose this model as it exhibits medial degeneration, inflammatory components, thrombus formation, and atherosclerosis [13], all of which are present in human AAA [12].

As a first step towards our long term goal, the purpose of this study is to determine the baseline biomechanical and microstructural changes as a result of AngII infusion, while also demonstrating a new means of assessing the coupled microstructural and biomechanical response of aorta in mice. We also seek to investigate how AngII leads to altered matrix organization and potential aneurysm formation. To provoke aortic remodeling, C57BL/6 mice were given systemic infusion of AngII through an osmotic pump. Simultaneous macroscopic testing combined with nonlinear optical microscopy demonstrated differences in the biomechanical response and microstructural organization of AngII infused mice as compared to saline infused controls.

A.3. Methods

A.3.1 Vessel Isolation

Mice on a C57BL/6 background from 5 to 6 months of age were given either 1000 ng/kg/min AngII (A9525, Sigma-Aldrich, St. Louis, MO USA) or sterile phosphate buffered saline (Saline control) (pH-7.4) for control, through an Azlet® mini-osmotic

pump (model 2002, Durect Co., Cupertino, CA USA) implanted subcutaneously into the dorsum. All animal use and experimental procedures for mouse testing were performed according to the approved protocol (#06-045) of the University of Arizona Institutional Animal Care and Use Committee (IACUC) and Animal Welfare Assurance Number (A3248-01). After 14 days the specimens were sacrificed and the aorta was surgically removed. Briefly, an incision was made into the abdominal cavity up through the thoracic cavity and the sternum removed. The viscera were carefully detached from the aorta leaving the aorta exposed along the back of the ventral cavity. The physiologic strain was determined by measuring the difference in lengths between markers placed on the aorta prior to and after excision and removal. Once excised from the ascending aorta to the iliac bifurcation, the aorta was cleaned of excess perivascular tissue taking care not to damage or tear the specimen. For this study the suprarenal region of the aorta was then cannulated on custom-pulled micropipette capillary tubes and secured using cyanoacrylate adhesive. Any large aortic branches were ligated using braided sutures. A small annulus was cut adjacent to the section being tested and imaged to determine wall thickness photogrammetrically from three averaged measurements.

Markers for the strain vision system were placed on the aorta, which was then mounted in the tubular-biaxial assembly of our microbiaxial optomechanical device [183]. The tubular-biaxial assembly attaches the specimen to a closed-loop flow system with a syringe pump and pressure transducer able to control luminal pressure. The attached specimen was then set in line with a single stepper motor and load cell within the bath through a bellows and pushrods pulley system able to control axial displacement and acquire axial loads. The specimen bath contained PBS, pH-7.4 warmed to 37±0.7°C, and was set over the strain vision system able to acquire vessel diameter. For further detail on this device, its capabilities and resolutions can be found in Keyes *et al*. [183].

A.3.2 Biaxial Testing

After the specimen was attached to the tubular-biaxial assembly, the undisplaced position of the specimen was interactively determined by pulling on the specimen until the

point where it no longer bends and creases are not visible in the vessel at zero pressure. The total axial displacement is then determined using the free unloaded length of the cannulated aortic section stretched to the point it reaches the previously determined physiologic strain. The vessel was then preconditioned by cycling through axial displacements up to the physiologic strain with concurrent pressurization of the vessel up to physiologic ranges using 10 consecutive cycles.

The tubular macroscopic biaxial test consisted of combining two uncoupled mechanical tests stepping between either fixed axial displacements or constant pressures. First, the specimen was pressurized from 0±2mmHg to 100±2 mmHg at each of six different axial displacements corresponding to 0.0, 0.2, 0.4, 0.6, 0.8 and 1.0 of the physiologic axial strain, ε_p. The specimen was then displaced up to the physiologic axial strain, ε_p, at each of five fixed pressures (P = 0±2, 25±2, 50±2, 75±2, 100±2 mmHg). Outputs of the mechanical tests were the vessel radius, axial stretch, lumen pressure, and axial load.

A.3.3 Multiphoton Imaging

Once the mechanical testing was complete the assembly was then placed underneath the Advanced Intravital Microscope (AIM) for multiphoton imaging. Our device has been specifically designed for integration with the AIM at the University of Arizona's BIO5 Institute. Multiphoton microscopy offers advantages of superior image quality, deeper optical sectioning, and reduced photo damage for hydrated *ex vivo* tissues when attempting to visualize the extracellular matrix microstructure [184]. The AIM uses a pulsed Titanium-Sapphire laser (680-1060nm) for simultaneous two-photon excitation and second harmonic imaging. For this study an Olympus XLUMPLFL 20x water immersion objective with a numerical aperture of 0.9 was used with a laser power on the sample of 25mW and excitation wavelength of λ=780nm. Collagen visualization came from second harmonic generation (SHG) collected through a bandpass filter (377/50). Autofluorescence emission from elastin is collected through another bandpass filter

(460/80). Further detail on the AIM and the integration of our mechanical device into the AIM can be found in Keyes *et al*. [185].

As obtaining a single image stack of an aorta took approximately 10 minutes, each vessel was slowly displaced axially to the physiologic strain used in the mechanical test and held for 3 minutes to eliminate any viscoelastic effects. Three image stacks were taken for each specimen, all at the physiologic strain with pressurizations of 0±2, 50±2, 100±2mmHg, each held for a time after being inflated again to eliminate any viscoelastic effects. Image stacks were taken of the specimen using a 500×500μm field of view at 4μm steps imaging from the adventitia into the lumen to a depth of 100μm.

Cross-sectional images of the aortas were obtained by embedding a portion of the previously mechanically tested and imaged aorta in 5% low melting point Agarose (#A9414, Sigma-Aldrich, St. Louis, MO USA) and sectioning using a vibratome. Multiphoton images were again taken using a 500×500μm field of view with 4μm steps up to a depth of 100 microns.

A.3.4 Image Analysis

Image stacks of each specimen contained both SHG and autofluorescence channels. The individual SHG channel was used to determine collagen fiber orientations using a custom written fiber-orientation analysis script for MATLAB (R2008a, MathWorks, Natick, MA USA) [186]. The software overlays vectors in the direction of fibers, from which histograms were generated of the collagen fiber orientations for each 0±2, 50±2, and 100±2mmHg stacks from each specimen. Vector orientations are included from every image in an image stack giving a view of the cumulative fiber orientation through the thickness. To prevent processing images with fibers oriented normal to the imaging plane (as would occur primarily after optical sectioning past the thickness of the wall), image post-processing stops after reaching 100μm with scanning starting at the adventitia. The mean mode and full width at half max (FWHM) were determined as indicators of the preferred fiber alignment and spread of fiber orientation, respectively. From this any

changes in fiber alignment or fiber dispersion that occurs with pressurization can be quantified.

Determination of the percent composition elastin and percent composition collagen was also performed using ImageJ. Masks were made for each channel of the unpressurized stacks using the Otsu method for thresholding. These were then turned into binary images and used to determine the total volume solid from which the individual percent contributions of collagen and elastin were able to be determined through the depth of each specimen.

A.3.5 Data Analysis

Data collected from the circumferential and axial mechanical tests were post-processed using MATLAB. Determining the mean Cauchy stresses ($\sigma_{\theta\theta}$, σ_{zz}) was estimated using [181, 187-189]

$$\sigma_{\theta\theta} = \frac{P_\theta r_i^2}{r_o^2 - r_i^2} \tag{1}$$

$$\sigma_{zz} = \frac{P_z}{A} \tag{2}$$

where P_θ is the transluminal pressure, r_i is the deformed inner radius, r_o is the deformed outer radius, P_z is the axial load, and A is the deformed (current) cross-sectional area. The deformed cross-sectional area, deformed inner radius, and deformed thickness were all determined based upon the measured original thickness of the vessel and assuming the tissue to be incompressible. Shear components were assumed to be negligible giving the Green strains ($E_{\theta\theta}$, E_{zz}) for both the circumferential and axial directions as [190, 191]

$$E_{\theta\theta} = \frac{1}{2}\left(\frac{r^2 - r_o^2}{r_o^2}\right) \tag{3}$$

$$E_{zz} = \frac{1}{2}(\lambda_z^2 - 1)$$

(4)

where r and r_o are the deformed and undeformed mid-thickness radii of the vessel respectively, and $\boldsymbol{\lambda_z}$ is the axial stretch. For constitutive modeling, the Cauchy stresses were converted to 2nd Piola Kirchoff stresses ($S_{\theta\theta}$, S_{zz}) determined from the deformation gradient tensor **F** and using $\mathbf{S}= J\,\mathbf{F}^{-T}\cdot\boldsymbol{\sigma}\cdot\mathbf{F}^{-1}$, where $J=det\,\mathbf{F}=1$ for an incompressible material [192].

$$S_{\theta\theta} = \frac{P_\theta r_i}{t(1+2E_{\theta\theta})} \tag{5}$$

$$S_{zz} = \frac{P_z}{A(1+2E_{zz})} \tag{6}$$

A.3.6 Constitutive Modeling

The mechanical response of the mouse aortic tissue can be quantified using a strain-energy density (W), the form of which is the basis for the constitutive model. We assumed the hyperelastic, incompressible, and anisotropic biomechanical response of mouse tissue can be adequately described using a standard Fung form strain-energy density function [191, 193]

$$W = \frac{C_0}{2}(e^Q - 1) \tag{7}$$

with

$$Q = a_1E_{\theta\theta}^2 + a_2E_{zz}^2 + 2a_{12}E_{zz}E_{\theta\theta} \tag{8}$$

In this model a_1 is a model parameter associated with circumferential ($\theta\theta$) direction, a_2 is a model parameter associated with the axial (zz) direction, a_{12} is a coupling model parameter between the axial and circumferential directions, and C_0 is a model parameter associated with initial slope of the mechanical response (having units of stress). The 2nd Piola Kirchoff stresses are then determined by taking the partial derivative of W with respect to **E** resulting in

$$S_{\theta\theta} = C_0(a_1 E_{\theta\theta} + a_{12} E_{zz})e^Q \tag{9}$$

$$S_{zz} = C_0(a_2 E_{zz} + a_{12} E_{\theta\theta})e^Q \tag{10}$$

Each individual aortic specimen dataset was fit to the constitutive relationship using SigmaStat (v. 3.1, SPSS, Chicago, IL) and also evaluated to obtain the output metrics of peak strain (defined as the circumferential strain at maximum pressure, i.e. 100mmHg, and physiologic axial prestrain) and stiffness (defined as $\partial\mathbf{S}/\partial\mathbf{E}$ at the in vivo axial prestrain and peak circumferential strain). An 'Average' set of parameters was also determined for the saline and AngII groups by fitting the above model to a combined data set of all samples within each group.

A.3.7 Statistical Analysis

Student's t-tests were conducted to compare between the AngII and saline control groups for each output metric, while paired t-tests were used to compare changes within each group for different pressurizations. A one way ANOVA was used to compare across macroscopic and microscopic tests to determine any correlations in changes in mechanical behavior with changes in fiber directionality, dispersion, and content. All statistical analyses were performed in SigmaStat (v. 3.1, SPSS, Chicago, IL).

A.4. Results

A.4.1 Summary of Mice Characteristics

Basic information about the animals used for testing is given in Table 1. Both the heart weight to body weight ratio and aortic thickness tended to be larger for the AngII group, however these increases were not found to be significantly different from the saline controls. The initial unstrained aortic diameter was found to be significantly increased for the AngII infused mice (p=0.026). Although only this single significant difference was found, aneurysm formation, as defined by a percent increase in maximum diameter of 30%,

determined photogrammetrically from images of the entire aorta, was found in 3 of the 6 AngII infused mice presenting in the thoracic aorta of one and in the suprarenal aorta of the other two mice (one of which appeared atherosclerotic).

A.4.2 Image Analysis

Differences in the saline control and AngII infused mouse aortic images were most evident between the controls and those infused with AngII exhibiting aortic aneurysm (Figures 1A and 1B). These 3 of the 6 AngII infused mice presenting with aneurysms showed a loss of crimp in the collagen fibers observed in the multiphoton images that was not observed in the non-aneurysmal AngII infused mice. Histograms of the SHG channel representing collagen fiber orientation (Figure 1C) also demonstrated that a response in fiber orientation and dispersion occurred with pressurization for both groups and were then used to determine fiber orientation mean mode and FWHM. Despite the different appearance of the multiphoton images (Figure 1A: control and AngII infused), both saline controls and AngII infused mouse aortas had preferential axial alignment and upon pressurization both shifted significantly in the direction of circumferential alignment (Figure 2A). Both groups showed increased fiber dispersion with pressurization; however, this increase in fiber dispersion was significant in the saline control mice and not in the AngII infused mice (Figure 2B), indicating a diminished response in AngII infused mice.

Differences in collagen versus elastin percentages through the depth of the vessel wall were not found to be different between the AngII infused mice and the saline controls (Figure 3). The expected change from a more collagen dense adventitial layer to a more elastin comprised medial layer is evident in both groups.

A.4.3 Constitutive Modeling and Biomechanical Response

Results from the saline control and AngII infused mice showed that there was no noticeable change in the in vivo axial prestrain, though the circumferential peak strain was significantly decreased for the AngII infused mice as compared to saline controls (Figure 4A). Stiffness in the circumferential direction tended to be higher in the AngII infused

mice compared to the saline controls (Figure 4B). It was also found that axial stiffness was an order of magnitude greater than circumferential stiffness ($p<0.001$) at corresponding strains for all but one of the AngII specimens exhibiting aneurysm. As expected, differences in the circumferential peak strain corresponded to differences in circumferential stiffness.

Figure 5 shows the constitutive model fit to an individual saline control (Figure 5A) and an AngII infused (Figure 5B) specimen for both the axial and circumferential directions along with raw experimental data. Though the individual fits were able to give R^2 values with an average of 0.92±0.15, the fits for the combined saline controls and AngII infused groups had R^2 values of 0.71 and 0.66, respectively. Even so, the values for each model parameter were still representative of each group and demonstrated the differences seen such as larger values for a_1 than a_2 for both groups denoting when stiffness in the axial direction was greater, and smaller values of a_{12} denoting little interaction between the axial and circumferential directions. Values for the Fung model constants for the combined and individual datasets for the saline control and AngII infused mice are given in Table 2.

A.5. Discussion

A.5.1 Summary of Results

A summary of the results show that there was a significant increase in aortic diameter for the AngII infused specimens ($p=0.026$), but this did not correspond to a significant increase in thickness although an increasing trend was observed. There was a significant ($p=0.009$) decrease in circumferential strain for the AngII infused group compared to the saline controls, which has yet to be reported elsewhere in the literature. Consistently, the stiffness in the circumferential direction tended to increase with 14 days of AngII infusion compared to the saline controls. Another interesting finding was that the axial stiffness was an order of magnitude greater than the circumferential stiffness at physiologic strains for both experimental groups for all but one aneurysmal AngII infused specimen. The large axial stress in most samples was a result of imposing the physiological

axial strains onto the small cross-sectional area of these aortic samples, which was not the case for the thicker walled atherosclerotic aneurysmal specimen.

Individual fits gave high R^2 values for all but the atherosclerotic aneurysm and the relative magnitude of the model parameters was as expected. For all but one, the axial material parameter carried greater weight than the circumferential material parameter ($a_1 > a_2$) and the coupling parameter (a_{12}) was extremely small. Fitting the entire data sets of both AngII infused and saline control responses ('Average' fits) resulted in much lower R^2 values, due primarily to the variability across mice within an experimental group.

Multiphoton images showed alterations in fiber appearance with AngII infused specimens that exhibited aneurysms. However, analysis of the mean mode and FWHM at each circumferential load did not find significant differences between the groups even when the three aneurysmal specimens are singled out. Analysis of the changes in mean mode and FWHM that occurred within each group with pressurization were able to show that AngII infusion did have an effect. Specifically, the collagen fiber FWHM of the saline controls showed a significant change in fiber dispersion with circumferential loading which was absent in the AngII infused vessels, indicating a decrease in the ability of the vessels to respond to circumferential loading. This could also be the reason for the decreased circumferential strain observed in the AngII infused group. These data suggest that AngII did have an effect on aortic microstructure after 14 days of infusion and on the ability of the aorta to respond to circumferential loading as evidenced by decreases in circumferential strain and fiber dispersion. Analysis of the collagen and elastin percent content through the adventitia into the media did not find any differences between groups.

A.5.2 Relation to Previous Works and Future Work

Prior research has demonstrated that AngII promotes increased aortic stiffness often through the activation of the AngII type 1 receptor [194-197]. None of these works, however, have utilized nonlinear microscopy or attempted to model the biomechanical behavior of AngII infused mice. There have been several groups that have utilized nonlinear optical microscopy to study the microstructural organization of vascular

structures [198-202]. Some of these have also looked at induced remodeling [198]. However, there have been only a few studies that utilize simultaneous nonlinear microscopy imaging during mechanical stimulation [183, 203-205]. The authors are not aware of any prior research that was able to simultaneously assess the extracellular matrix and biomechanical response of induced remodeling in a mouse vessel.

Initially, we chose here to model our biaxial data with the Fung constitutive relationship [191, 193] as an easily implementable model for determining constitutive relationships. Future work will include taking the same data and fitting it to microstructurally based constitutive relationships [181, 206] so that comparisons can be made between model derived fiber angles (from nonlinear regression) and those measured from our imaging techniques. Future work is also ongoing within our laboratory focused on using the measured microstructural fiber angles and constructing a microstructurally based constitutive model that is based on this data. Our research group will also utilize the derived constitutive models for induced remodeling to study more closely the biomechanical environment of the developing aneurysm by utilizing the derived constants in computational (finite element) models of aneurysmal tissues.

A.5.3 Study Limitations

One limitation of the study was that circumferential and axial tests were not able to be simultaneously run and thus these data sets were generated sequentially. The axial and circumferential data sets were able to be combined to produce biaxial data sets, but this may have affected the response quantified. For example, the coupled material parameter (a_{12}) could be particularly small across all samples due to the coupling of the axial and circumferential tests. Another limitation of the study included the uncertainty of image stacks being able to adequately image through the thickness of the aorta. Even though multiphoton imaging offers advantages for deep tissue imaging, there was still significant signal loss deeper into the tissue, so that image stacks were kept to only 100 μm from the adventitia into the media and analysis of elastin and collagen relative percentages were only made up to 60 μm into the vessel wall. Images taken from deep within the media were

still of value and future work should look into quantifying the amount of disrupted lamina present in certain animal models of aneurysm.

A.5.4 Conclusions

Although C57BL/6 mice have been known to spontaneously form aneurysm [12], the result of 3 of the 6 AngII infused mice presenting with aneurysm was an unexpected finding. Unlike the *ApoE*$^{-/-}$ with AngII infusion model, the aneurysmal specimens in this study did not present with medial degeneration and thrombus formation, as evidenced by the cross-sectional images, except in one instance. Still, aneurysmal specimens did demonstrate AngII induced remodeling within 14 days of infusion, as evidenced by the loss of collagen crimp in the adventitia. AngII infused mice did demonstrate changes in mechanical response that was significant after only 14 days and coincided with changes in microstructure. As compared to saline control animals, the collagen fibers of the AngII-infused mouse aorta were not able to disperse as greatly in response to increased luminal pressure. With longer administration of AngII, we expect to see the reported trends in response reach even greater significance. In conclusion, our results suggest that aortic remodeling, as quantified using microstructural and biomechanical endpoints, does occur after 14 days of AngII infusion in C57BL/6 mice, possibly leading to aneurysmal deterioration. This study serves as a first step towards understanding the time-course of microstructural and biomechanical changes that occur with AngII-infusion and in the AngII-infused *ApoE*$^{-/-}$ model of AAA.

A.6. Acknowledgements

The authors would like to acknowledge the support of the American Heart Association (GIA 10GRNT4580045 to JPVG), the National Science Foundation (CAREER 0644570 to JPVG), the help of Tom Doetschman and Connie Gard, the National Institutes of Health (HL92508), The Stephen Michael Schneider & The William J. "Billy" Gieszl Investigator Award (University of Arizona) and Arizona Biomedical

Research Commission (#0901). Imaging was done on an NIH sponsored shared device (NIH/NCRR S10RR023737).

A.7. References

1. Vorp, D.A., *Biomechanics of abdominal aortic aneurysm.* J Biomech, 2007. **40**(9): p. 1887-902.
2. Vande Geest, J.P., M.S. Sacks, and D.A. Vorp, *The effects of aneurysm on the biaxial mechanical behavior of human abdominal aorta.* J Biomech, 2006. **39**(7): p. 1324-34.
3. Choi, H., R.C. Tostes, and R.C. Webb, *Mitochondrial aldehyde dehydrogenase prevents ROS-induced vascular contraction in angiotensin-II hypertensive mice.* J Am Soc Hypertens.
4. Daugherty, A. and L. Cassis, *Angiotensin II-mediated development of vascular diseases.* Trends Cardiovasc Med, 2004. **14**(3): p. 117-20.
5. Intengan, H.D. and E.L. Schiffrin, *Vascular remodeling in hypertension: roles of apoptosis, inflammation, and fibrosis.* Hypertension, 2001. **38**(3 Pt 2): p. 581-7.
6. Sparks, M.A., et al., *Angiotensin II type 1A receptors in vascular smooth muscle cells do not influence aortic remodeling in hypertension.* Hypertension. **57**(3): p. 577-85.
7. Daugherty, A., M.W. Manning, and L.A. Cassis, *Angiotensin II promotes atherosclerotic lesions and aneurysms in apolipoprotein E-deficient mice.* J Clin Invest, 2000. **105**(11): p. 1605-12.
8. Manning, M.W., et al., *Abdominal aortic aneurysms: fresh insights from a novel animal model of the disease.* Vasc Med, 2002. **7**(1): p. 45-54.
9. Cassis, L.A., et al., *Aldosterone does not mediate angiotensin II-induced atherosclerosis and abdominal aortic aneurysms.* Br J Pharmacol, 2005. **144**(3): p. 443-8.
10. Henriques, T.A., et al., *Orchidectomy, but not ovariectomy, regulates angiotensin II-induced vascular diseases in apolipoprotein E-deficient mice.* Endocrinology, 2004. **145**(8): p. 3866-72.
11. Manning, M.W., L.A. Cassis, and A. Daugherty, *Differential effects of doxycycline, a broad-spectrum matrix metalloproteinase inhibitor, on angiotensin*

II-induced atherosclerosis and abdominal aortic aneurysms. Arterioscler Thromb Vasc Biol, 2003. **23**(3): p. 483-8.

12. Goergen, C.J., et al., *Influences of aortic motion and curvature on vessel expansion in murine experimental aneurysms.* Arterioscler Thromb Vasc Biol. **31**(2): p. 270-9.
13. Baek, S., K.R. Rajagopal, and J.D. Humphrey, *A theoretical model of enlarging intracranial fusiform aneurysms.* J Biomech Eng, 2006. **128**(1): p. 142-9.
14. Eberth, J.F., et al., *Mechanics of carotid arteries in a mouse model of Marfan Syndrome.* Ann Biomed Eng, 2009. **37**(6): p. 1093-104.
15. Humphrey, J.D. and K.R. Rajagopal, *A constrained mixture model for arterial adaptations to a sustained step change in blood flow.* Biomech Model Mechanobiol, 2003. **2**(2): p. 109-26.
16. Daugherty, A. and L.A. Cassis, *Mouse models of abdominal aortic aneurysms.* Arterioscler Thromb Vasc Biol, 2004. **24**(3): p. 429-34.
17. Keyes, J.T., et al., *Adaptation of a two-photon-microscope-interfacing planar biaxial device for the microstructural characterization of small tubular tissue specimens.* Journal of Biomechanical Engineering, 2011. Jul; **133**(7):075001.
18. Peti-Peterdi, J. and P.D. Bell, *Confocal and two-photon microscopy.* Methods Mol Med, 2003. **86**: p. 129-38.
19. Keyes, J.T., et al., *Design and Demonstration of a Microbiaxial Optomechanical Device for Multiscale Characterization of Soft Biological Tissues with Two-Photon Microscopy.* Microsc Microanal: p. 1-9.
20. Kirkpatrick, N.D., et al., *In vitro model for endogenous optical signatures of collagen.* J Biomed Opt, 2006. **11**(5): p. 054021.
21. Schulze-Bauer, C.A., P. Regitnig, and G.A. Holzapfel, *Mechanics of the human femoral adventitia including the high-pressure response.* Am J Physiol Heart Circ Physiol, 2002. **282**(6): p. H2427-40.

22. Gleason, R.L., E. Wilson, and J.D. Humphrey, *Biaxial biomechanical adaptations of mouse carotid arteries cultured at altered axial extension.* J Biomech, 2007. **40**(4): p. 766-76.
23. Humphrey, J.D., et al., *Fundamental role of axial stress in compensatory adaptations by arteries.* J Biomech, 2009. **42**(1): p. 1-8.
24. Debes, J.C. and Y.C. Fung, *Biaxial mechanics of excised canine pulmonary arteries.* Am J Physiol, 1995. **269**(2 Pt 2): p. H433-42.
25. Fung, Y., *Biomechanics: Mechanical Properties of Living Tissues*. 2nd ed. 1993, New York: Springer.
26. Vande Geest, J.P., M.S. Sacks, and D.A. Vorp, *Age dependency of the biaxial biomechanical behavior of human abdominal aorta.* J Biomech Eng, 2004. **126**(6): p. 815-22.
27. Fung, Y.C. and S.Q. Liu, *Determination of the mechanical properties of the different layers of blood vessels in vivo.* Proc Natl Acad Sci U S A, 1995. **92**(6): p. 2169-73.
28. Benetos, A., et al., *Influence of angiotensin-converting enzyme and angiotensin II type 1 receptor gene polymorphisms on aortic stiffness in normotensive and hypertensive patients.* Circulation, 1996. **94**(4): p. 698-703.
29. Benetos, A., et al., *Arterial alterations with aging and high blood pressure. A noninvasive study of carotid and femoral arteries.* Arterioscler Thromb, 1993. **13**(1): p. 90-7.
30. Benetos, A., et al., *Influence of angiotensin II type 1 receptor polymorphism on aortic stiffness in never-treated hypertensive patients.* Hypertension, 1995. **26**(1): p. 44-7.
31. Lajemi, M., et al., *Angiotensin II type 1 receptor-153A/G and 1166A/C gene polymorphisms and increase in aortic stiffness with age in hypertensive subjects.* J Hypertens, 2001. **19**(3): p. 407-13.
32. Boulesteix, T., et al., *Micrometer scale ex vivo multiphoton imaging of unstained arterial wall structure.* Cytometry A, 2006. **69**(1): p. 20-6.

33. Werkmeister, E., et al., *Multiphoton microscopy for blood vessel imaging: new non-invasive tools (Spectral, SHG, FLIM).* Clin Hemorheol Microcirc, 2007. **37**(1-2): p. 77-88.
34. Zoumi, A., et al., *Imaging coronary artery microstructure using second-harmonic and two-photon fluorescence microscopy.* Biophys J, 2004. **87**(4): p. 2778-86.
35. Zoumi, A., A. Yeh, and B.J. Tromberg, *Imaging cells and extracellular matrix in vivo by using second-harmonic generation and two-photon excited fluorescence.* Proc Natl Acad Sci U S A, 2002. **99**(17): p. 11014-9.
36. Schenke-Layland, K., et al., *Imaging of cardiovascular structures using near-infrared femtosecond multiphoton laser scanning microscopy.* J Biomed Opt, 2005. **10**(2): p. 024017.
37. Gleason, R.L., et al., *A multiaxial computer-controlled organ culture and biomechanical device for mouse carotid arteries.* J Biomech Eng, 2004. **126**(6): p. 787-95.
38. Keyes, J.T., et al., *Design and Demonstration of a Microbiaxial Optomechanical Device for Multiscale Characterization of Soft Biological Tissues with Two-Photon Microscopy.* Microsc Microanal, 2011: p. 1-9.
39. Zaucha, M.T., et al., *A novel cylindrical biaxial computer-controlled bioreactor and biomechanical testing device for vascular tissue engineering.* Tissue Eng Part A, 2009. **15**(11): p. 3331-40.
40. Gasser, T.C., R.W. Ogden, and G.A. Holzapfel, *Hyperelastic modelling of arterial layers with distributed collagen fibre orientations.* J R Soc Interface, 2006. **3**(6): p. 15-35.

A.8. Figures with Figure Legends

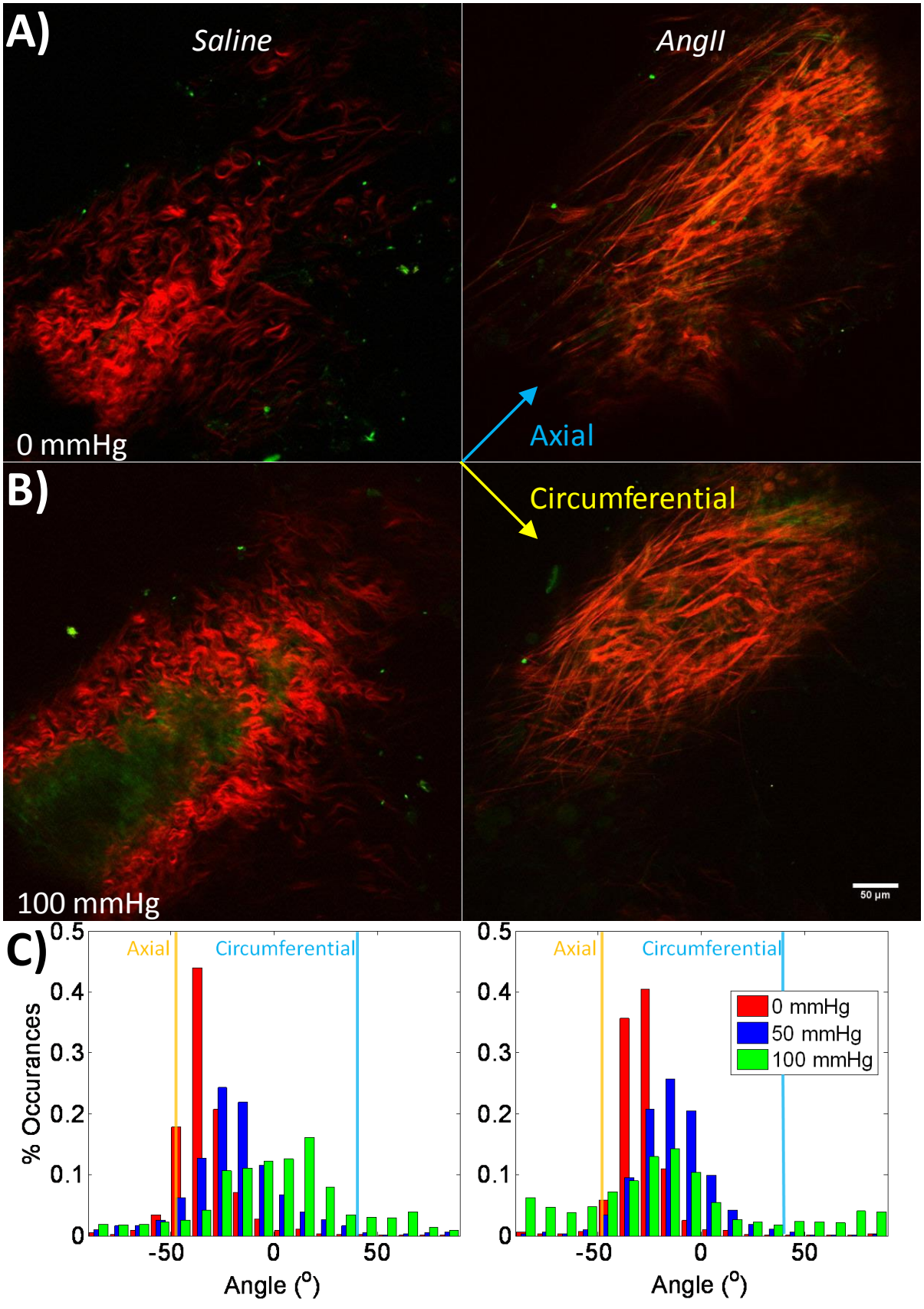
A)
Saline
AngII
0 mmHg
Axial
B)
Circumferential
100 mmHg
50 µm
C)
Axial
Circumferential
% Occurances
0.5
0.4
0.3
0.2
0.1
0
-50
0
50
Angle (°)
0 mmHg
50 mmHg
100 mmHg

Figure 1: Representative multiphoton images of a saline control mouse aorta (Left) and an AngII infused mouse aorta presenting with aneurysm (Right) pulled to the in vivo axial strain at both 0 mmHg (Tile A) and 100 mmHg (Tile B). SHG channel (Red) represents the collagen content of the aorta, while NADH channel (Green) represents primarily the elastin content. These images are taken approximately in the adventitial layer of the aorta. Blue and yellow arrows correspond to axial and circumferential directions respectively. In the saline mouse aorta the expected waviness of the collagen fiber bundles is evident in both unpressurized and pressurized states, while the AngII infused mouse aorta does not exhibit the expected waviness indicating collagen crimp. Histograms (Tile C) show the overall collagen fiber orientations throughout the adventitial layer of the aorta in both 0 mmHg (Red), 50 mmHg (Blue), and 100 mmHg (Green) pressurized states, with blue and yellow bars again representing axial and circumferential directions respectively.

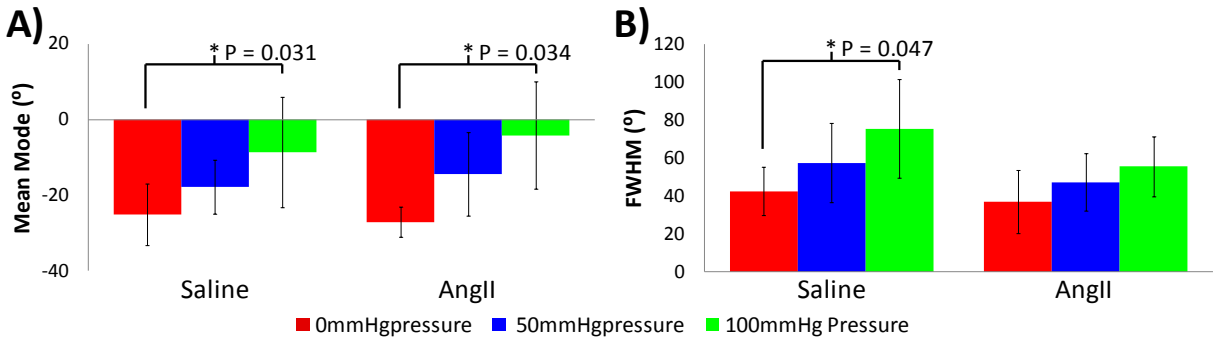

Figure 2: The fiber orientation mean mode (Tile A) in reference to -45° being the axial alignment and 45° being circumferential alignment. Both saline controls and AngII infused mice had preferential axial alignment that shifted with pressurization; both groups exhibited significant changes in fiber alignment with 100mmHg pressurization compared to the unpressurized vessels. The FWHM (Tile B) represents the degree of fiber dispersion, with 0° corresponding to no fiber dispersion. Both saline controls and AngII infused mice exhibited increased fiber dispersion with pressurization, the variance of which was significantly different between 0 and 100 mmHg for Saline infused vessels indicating a decreased fiber response to pressurization in the AngII infused vessels.

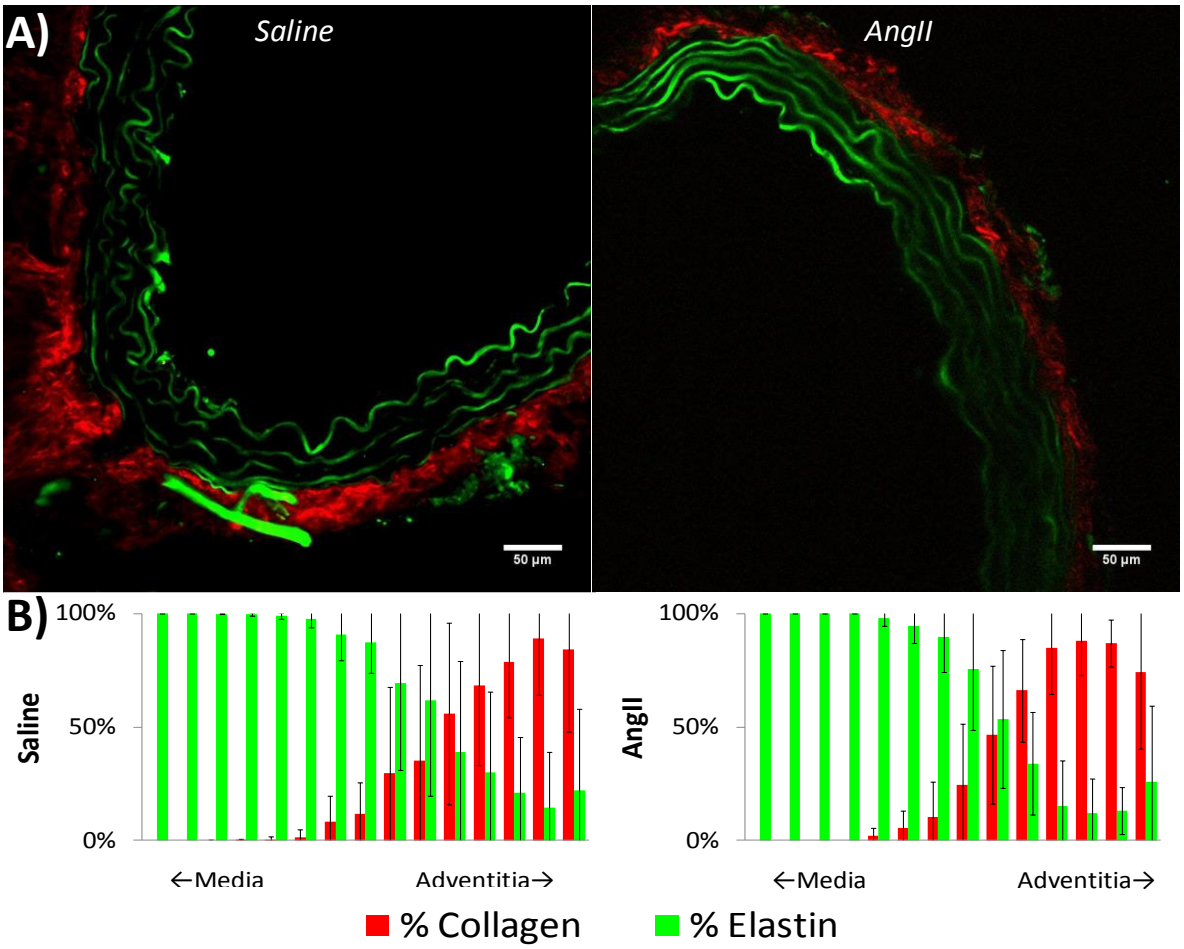

Figure 3: A) Representative cross-sectional multiphoton images depicting the collagen (Red) filled adventitia and elastin (Green) sheets of the media. B) The collagen versus elastin percentages for both Saline control and AngII infused mice plotted through the depth of the aorta from adventitia into the media. Step sizes are 4 µm. The expected change from a more collagen filled adventitial layer to a more elastin filled medial layer is evident in both. Note that the collagen versus elastin percentages (Tile B) were determined from the tubular image stacks and not from these cross sectional images.

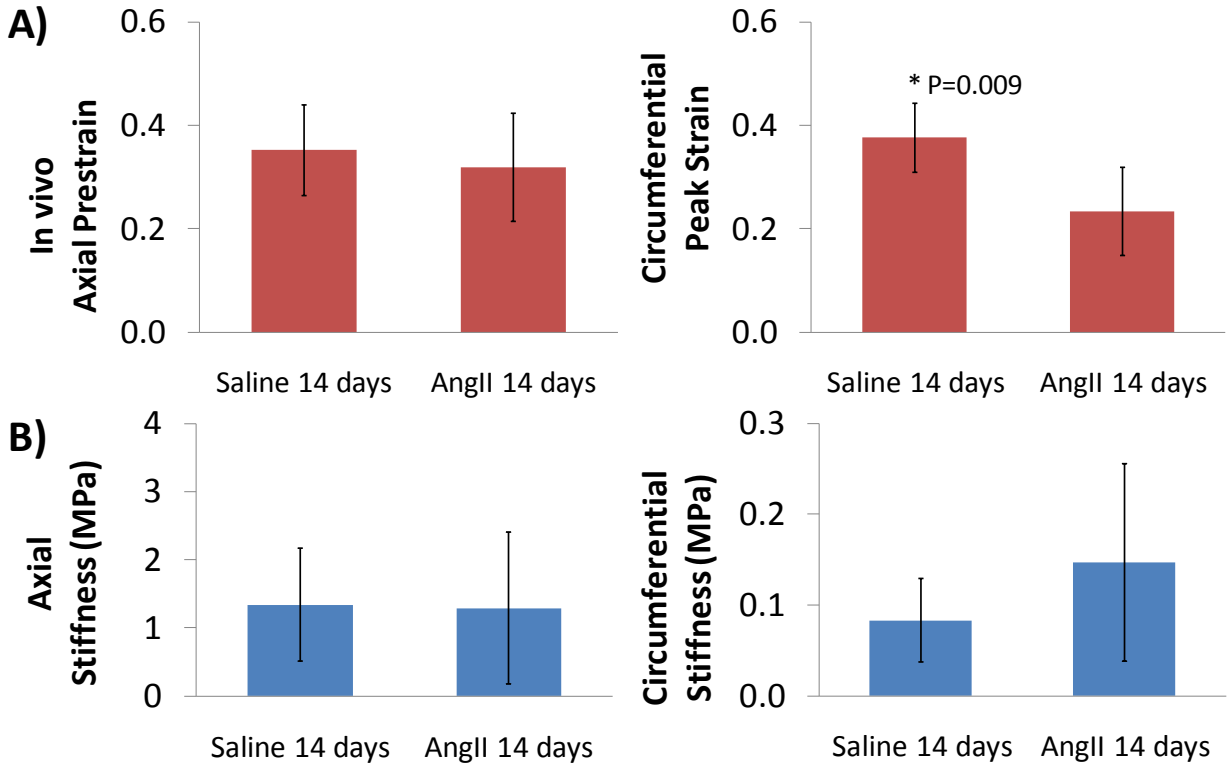

Figure 4: A) Left: In-vivo axial prestrain Right: Peak circumferential strains for both AngII and saline controls. The circumferential peak strain was significantly reduced in the AngII specimens (P=0.009). B) Stiffness of the suprarenal aorta taken at the point of peak strain in the axial (Left) and circumferential (Right) directions for both AngII and saline controls. While axial stiffness did not appear different between the groups, the circumferential stiffness values tended to increase with AngII infusion (but not significantly). Note also the order of magnitude difference between axial and circumferential stiffness for both saline control and AngII infused mice.

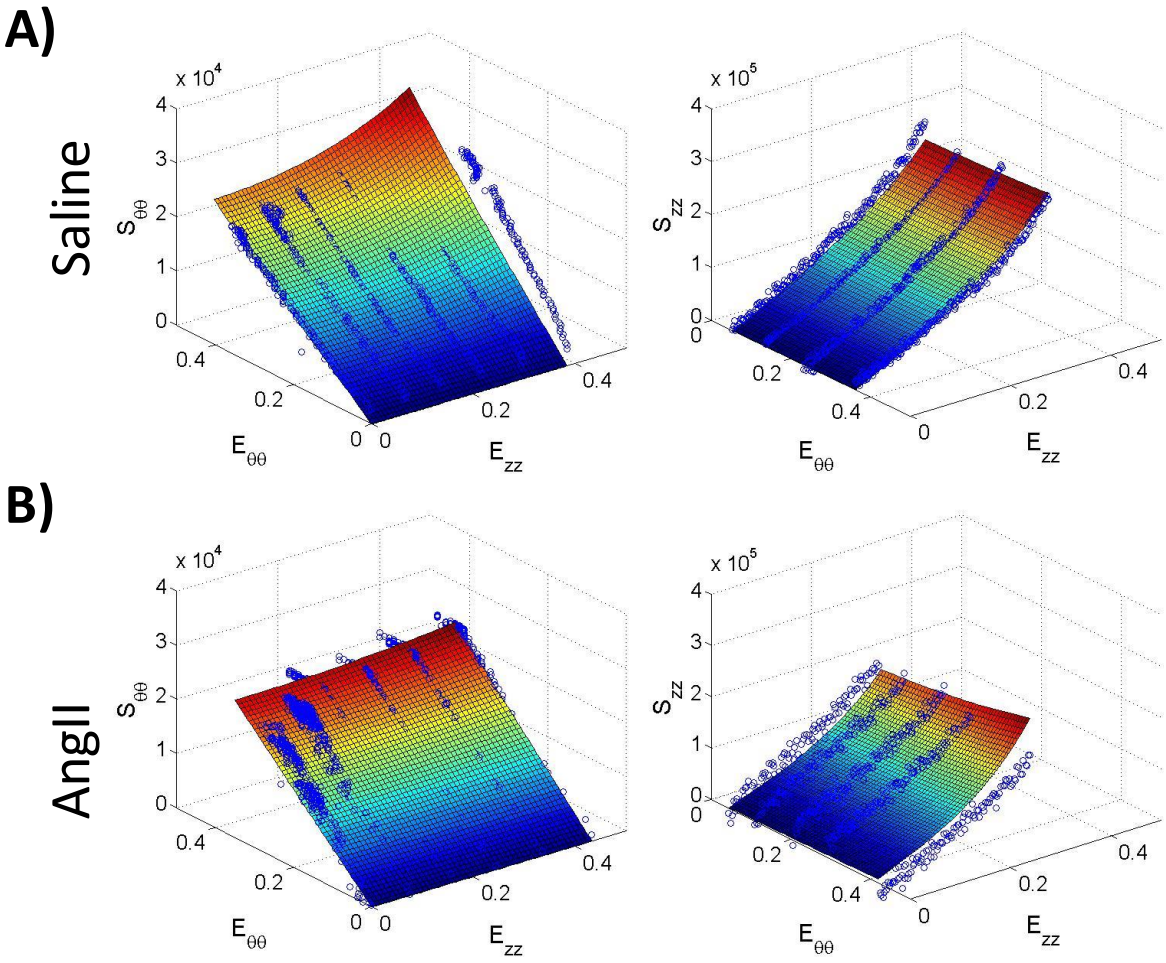

Figure 5: Individual surface fits over the region of tested with experimental data points for a Saline control (A) and an AngII infused (B) mouse test. Note the order of magnitude difference between the axial (Left) and circumferential (Right) stress values for both saline control and AngII infused mice.

A.9. Tables

Table 1. Basic information taken from the two mouse groups used in this study prior to macroscopic and microscopic testing.

	Group size (n)	Weight (g)	Heart weight (g)	Aortic thickness (μm)	Initial inner aortic diameter (mm)
Saline	6	28.1±5.7	0.141±0.038	135.1±15	0.598±0.05
AngII	6	28.5±4.3	0.170±0.031	176.3±72	0.860±0.35*

Values are means ± standard deviations from n = 6 mice/group.

* denotes statistically significant difference with infusion ($p = 0.026$).

Table 2. Fung constants fit to the experimental data of saline infused and AngII infused mice and corresponding R^2 values. Descriptions for the material parameters are in section 2.6.

	C_0 (kPa)	a_1	a_2	a_{12}	R^2
Saline					
Average	1055.9	0.0288	0.708	0.0474	0.71
a	2541.0	0.0534	0.331	2.14E-11	0.98
b	1065.8	0.0360	1.262	1.30E-10	0.98
c	1832.1	0.0393	0.440	2.25E-10	0.97
d	1402.4	0.0535	0.401	7.17E-11	0.90
e	4895.8	0.0078	0.277	1.96E-11	0.96
f	439.1	0.101	2.987	1.38E-9	0.94
AngII					
Average	4676.0	0.0137	0.141	0.00670	0.66
a	13295.8	0.00680	0.0377	0.00113	0.97
b	224.9	0.282	2.121	1.85E-10	0.98
c	811.1	0.189	2.071	0.00260	0.98
d	773.2	0.131	0.995	2.45E-10	0.99
e	383.1	0.132	1.249	0.0172	0.91
f	1124.4	0.100	0.0699	0.0291	0.45

APPENDIX B: Progressive Alterations in Microstructural Organization and Biomechanical Response in the ApoE Mouse Model of Aneurysm

Darren Haskett[1] MS, Mohamad Azhar[2] PhD, Urs Utzinger[1,3,4] PhD, Jonathan Vande Geest[1,3,4,5] PhD

*1. Graduate Interdisciplinary Program of Biomedical Engineering**

2. Department of Pediatrics, Indiana University

*3. BIO5 Institute**

*4. Department of Biomedical Engineering**

*5. Department of Aerospace and Mechanical Engineering**

**The University of Arizona*

Tucson, AZ

Corresponding Author

Jonathan P. Vande Geest, PhD

The University of Arizona

Department of Aerospace and Mechanical Engineering

Department of Aerospace and Biomedical Engineering

BIO5 Institute

Graduate Interdisciplinary Program in Biomedical Engineering

1130 N. Mountain

PO Box 210119

Tucson, AZ 85721-0119

Phone: (520) 621-2514

Fax: (520) 621-8191

Email: jpv1@email.arizona.edu

Biomatter. 2013; 3(3)

B.1 Abstract

AAA is a complex disease that leads to a localized dilation of the infrarenal aorta that develops over years. Longitudinal information in humans has been difficult to obtain for this disease, therefore mouse models have become increasingly used to study the development of AAAs. The objective of this study was to determine any changes that occur in the biomechanical response and fiber microstructure in the ApoE$^{-/-}$ AngII mouse model of aneurysm during disease progression. Adult ApoE$^{-/-}$ AngII infused mice along with wild-type controls were taken at 14 and 28 days. Aortas were excised and tested simultaneously for biaxial mechanical response and ECM organization. Datasets were fit to a Fung-type constitutive model to give peak strains and stiffness values. Images from two photon microscopy were quantified in order to assess the preferred fiber alignment and degree of fiber orientation. Biomechanical results found significant differences that were present at 14 days had returned to normal by 28 days along with significant changes in fiber orientation and dispersion indicating remodeling occurring within the aneurysmal wall. This return of some of the normal biomechanical function, in addition the continuing changes that occur in the microstructure suggest a restorative response that occurs in the ApoE-/- AngII infused model after the initial aneurysm formation.

Key Words:

ApoE,
AAA,
Aneurysm,
Mouse model,
Mechanical,
Microstructure,
Two-photon,
AngII

B.2. Introduction

Abdominal aortic aneurysm (AAA) is currently a leading cause of death in developed countries with occurrence rates expected to increase with aging populations.[207] As they are often asymptomatic, once rupture occurs, AAA is associated with significant morbidity and mortality. Studies have shown that aneurysmal tissue is remodeled in the disease process in humans with alterations in mechanical properties.[1, 173] However, AAA disease is complex and develops over years and obtaining longitudinal information from patients has proven very difficult, thus making the study of the underlying mechanisms of disease initiation and progression problematic. To redress this lack of knowledge involving the evolving mechanical properties with the physiological processes, mouse models have become increasingly used to study the development of AAAs.

Prominent among these mouse models for aneurysm is the apolipoprotein-E knockout ($ApoE^{-/-}$) mouse with long-term subcutaneous infusion of angiotensin II (AngII) described by Daugherty et al.[15] Recently several publications have considered the $ApoE^{-/-}$ AngII infused model of AAA looking at causes of inflammation and inhibiting aneurysm formation.[208-211] While important, such studies do not provide insight into the hemodynamics or mechanical environment which are now considered instigating factors in the initiation and progression of disease. To fill this gap in the literature, recent work by Ford[212] and Goergen[213] have looked into the hemodynamics and cyclic strain in the $ApoE^{-/-}$ AngII infused model of AAA, respectively.

Still missing, though, are the biomechanical properties of the $ApoE^{-/-}$ AngII infused model of AAA associated with progression of disease. Also of importance, is the need to couple any biomechanical modeling with changes in extracellular matrix and associated alterations in microstructure. Recent work has started to address this by first defining the mechanical properties and constitutive modeling of wild-type (C57BL/6) mice.[214, 215] However, these studies do not include the actual the $ApoE^{-/-}$ AngII infused model of AAA. The purpose of this paper is to assess changes that occur in the biomechanical response

along with associated ECM remodeling and alterations in fiber response during disease progression for the ApoE$^{-/-}$ AngII infused mouse model of AAA.

B.3. Methods

B.3.1 Mouse Model and Specimen Preparation

ApoE knockout mice (*ApoE*$^{-/-}$) were bred from stock obtained from The Jackson Laboratory (Bar Harbor, ME), backcrossed 10 times into wild-type C57BL/6J background, and maintained as a colony of heterozygous animals. All animal use and experimental procedures for mouse testing were performed according to the approved protocol (#06-045) of the University of Arizona Institutional Animal Care and Use Committee (IACUC) and Animal Welfare Assurance Number (A3248-01). Adult (approximately six month old) *ApoE*$^{-/-}$ and *ApoE*$^{+/+}$ (C57BL/6J wild-type control mice) had Azlet® mini-osmotic pumps (Durect Corp) implanted subcutaneously into the dorsum under anesthesia. Pumps were filled with either AngII (#A9525 Sigma-Aldrich, St. Louis, MO USA) to provide for continuous infusion at a rate of 1000 ng /kg/min or saline for either 14 or 28 days (models 2002 and 2004 respectively) as described in the literature[10, 135, 216]. Mice were placed on a high fat diet and fed *ad libitum*. Groups included control mice with saline vehicle (N=8), control mice with AngII vehicle (N=8), and the aneurysm model of *ApoE*$^{-/-}$ with AngII vehicle (N=6) each split between 14 and 28 days of infusion. For the aneurysm model, only specimens that exhibited aneurysm formation (defined as a >50% increase in aortic diameter or the onset of dissection) and able to undergo full testing at the two time points were used in this study.

At the end of the 14 or 28 day vehicle infusion, mice were sacrificed and the unfixed aorta was isolated and surgically removed (**Figure 1**) for mechanical testing as reported previously.[215] Briefly, an incision was made from the abdominal cavity to the thoracic cavity in order to carefully remove the viscera leaving the aorta exposed along the back of the ventral cavity. The physiologic strain was determined using markers placed on the aorta and measured prior to and after excision and detachment. Once excised from the ascending aorta to the iliac bifurcation, the aorta was cleaned of excess perivascular tissue taking care

not to damage or tear the specimen. Proximal and distal segments of the vessel were trimmed, and the suprarenal region of the aorta was cannulated onto custom-pulled micropipette capillary tubes and secured using cyanoacrylate adhesive gel. Any large aortic branches were ligated using braided sutures. A small annulus was cut adjacent to the section being tested and imaged to give a mean value for wall thickness photogrammetrically from three averaged measurements.

B.3.2 Mechanical Testing and Multiphoton Imaging Protocols

Mechanical testing and imaging protocols have been described previously.[215] Briefly, the specimen was mounted in the tubular-biaxial assembly of our microbiaxial optomechanical device[183] with markers for the strain vision system placed on the vessel. The specimen bath contained PBS, pH-7.4, warmed to 37±0.7°C and was set over the strain vision system. A closed-loop flow system with a syringe pump and pressure transducer controlled luminal pressure within the specimen. A single stepper motor and load cell within the bath allows control of axial displacement and acquisition of axial loads using custom written LabView program (National Instruments). Further details on this device, its capabilities, and its resolutions have been reported previously.[183, 217]

For mechanical testing, the original unloaded outer diameter and axial length of the mounted specimen was interactively determined by pulling on the specimen until the point where it no longer bends and creases are not visible in the vessel at zero pressure. The vessel was preconditioned by cycling through axial displacements up to the previously determined physiologic strain with concurrent pressurization of the vessel up to physiologic ranges using 10 consecutive cycles. Biaxial data were collected from a cyclic pressurization test consisting of pressurization from 0±2mmHg to 100±2 mmHg while stepping through six equal axial displacements up to the physiologic axial strain. Specimens were not inflated or stretched beyond the physiologic values in order to ensure vessel integrity and avoid damage to the ECM that might otherwise occur before imaging. Outputs of the mechanical tests were the vessel radius, axial stretch, lumen pressure, and axial load.

Once the mechanical testing was complete the assembly was placed underneath the Advanced Intravital Microscope (AIM) for multiphoton imaging, where the laser power on the sample was 25mW at an excitation wavelength of λ=780nm. Collagen visualization came from second harmonic generation (SHG) collected through a bandpass filter (377/50), while autofluorescence emission from elastin is collected through another bandpass filter (460/80). Further detail on the AIM and the integration of our mechanical device into the AIM can be found in Keyes et al.[185] Each vessel was slowly displaced axially to the physiologic strain used in the mechanical test and held for 3 minutes to eliminate any viscoelastic effects. Three image stacks were taken for each specimen, at pressurizations of 0±2, 50±2, 100±2mmHg, using a 500×500μm field of view at 4μm steps imaging from the adventitia into the lumen to a depth of 100μm. Cross-sectional images of the aortas were obtained from vibratoming a portion of the previously mechanically tested to obtain a cross-sectional slice and were again taken using a 500×500μm field of view with 4μm steps up to a depth of 100 microns. The individual SHG channel was used to determine collagen fiber orientations using a custom written fiber-orientation analysis script for MATLAB (R2013a, MathWorks).[186] Outputs of the image analysis were the mean mode and full width at half max (FWHM), which indicate the preferred fiber alignment and degree of fiber orientation, respectively.

B.3.3 Data Analysis and Constitutive Framework

Data post-processing and constitutive formulation have been described previously [215]. Briefly, the biaxial data were post-processed using MATLAB to give the mean circumferential and axial Cauchy stresses using standard formulae:[181, 187-189]

$$\sigma_{\theta\theta} = \frac{P_\theta r_i}{t}, \sigma_{zz} = \frac{P_z}{A} \qquad (1)$$

where P_θ is the transluminal pressure, r_i is the deformed (current) inner radius, t is the deformed thickness, P_z is the axial load, and A is the deformed cross-sectional area. The tissue was assumed to be incompressible, and using the previously determined original thickness of the vessel, the deformed cross-sectional area, thickness, and inner radius were

determined. Shear components were assumed to be negligible giving the Green strains ($E_{\theta\theta}$, E_{zz}) for both the circumferential and axial directions as[190, 191]

$$E_{\theta\theta} = \frac{1}{2}\left(\frac{r^2 - r_o^2}{r_o^2}\right), E_{zz} = \frac{1}{2}(\lambda_z^2 - 1) \qquad (2)$$

where r and r_o are the deformed and undeformed mid-thickness radii of the vessel respectively, and $\boldsymbol{\lambda_z}$ is the axial stretch.For constitutive modeling, the Cauchy stresses were then converted to 2nd Piola Kirchoff stresses ($S_{\theta\theta}$, S_{zz}) determined from the deformation gradient tensor **F** and using $\mathbf{S} = J\,\mathbf{F}^{-T} \cdot \boldsymbol{\sigma} \cdot \mathbf{F}^{-1}$, where $J = det\ \mathbf{F} = 1$ for an incompressible material[192]:

$$S_{\theta\theta} = \frac{P_\theta r_i}{t(1+2E_{\theta\theta})}, S_{zz} = \frac{P_z}{A(1+2E_{zz})} \qquad (3)$$

We employed a modified form of the Fung strain-energy density function which has been shown to adequately describe the anisotropic mechanical response[191, 193] to quantify the biaxial mechanical behavior. The specific form being:

$$W = \frac{C_0}{2}(e^Q - 1)\,, Q = a_1 E_{\theta\theta}^2 + a_2 E_{zz}^2 + 2a_{12} E_{zz} E_{\theta\theta} \qquad (4)$$

In this formulation, C_0 is a model parameter associated with initial slope of the mechanical response (having units of stress), and a_1 and a_2 are parameters associated with the circumferential direction (θθ) and axial direction (zz) respectively (unitless), and a_{12} is coupling model parameter between the two directions (unitless). Taking the partial derivative of W with respect to **E** gives the 2nd Piola Kirchoff stresses for which each specimen was then fit using the constitutive relationship in SigmaStat (v3.1, SPSS) and evaluated to obtain the output metrics of peak strain (defined as the circumferential strain at maximum pressure, i.e. 100mmHg, and physiologic axial strain) and stiffness (defined as $\partial\mathbf{S}/\partial\mathbf{E}$ at the in vivo axial strain and peak circumferential strain).

B.3.4 Statistical Analysis

A repeated measures analysis of variance (ANOVA) was used to compare across the ApoE$^{-/-}$ AngII infused model, AngII infused wild-type mice, and control groups for each output metric to determine any correlations in changes in mechanical behavior and

changes in fiber directionality and dispersion. Pairwise comparisons were performed post hoc to identify which groups were different, with $p<0.05$ deemed statistically significant. Paired t-tests were used to compare changes within each group for different pressurizations. All statistical analyses were performed in SigmaStat.

B.4. Results

B.4.1 General Response

As anticipated there was no difference found in any metric between the two time periods of 14 and 28 days for the control mice, thus the data have been combined into one group for reporting below. General results include the significant increase in outer aortic diameter for both 14 and 28 day groups of the aneurysmal ApoE$^{-/-}$ AngII infused model compared to controls (**Figure 2A**). The 14 day ApoE$^{-/-}$ AngII infused model aneurysmal group was found to be significantly greater than controls as well as wild-type AngII infused groups, however the 28 day ApoE$^{-/-}$ AngII infused group was not significantly different from controls or wild-type AngII infused groups (**Figure 2B**). Although physiologic strain tended to decrease with both AngII infusion and with time and more so with the ApoE-/- AngII infused model, there were no significant differences found among the groups (**Figure 2C**).

B.4.2 Mechanics and Constitutive Relationship

Parameters for each individual constitutive fit can be found in *Table 1*. There was a significant decrease in circumferential strain at both time points in the ApoE$^{-/-}$ AngII infused aneurysmal model (**Figure 3A**). This decrease in circumferential strain was accompanied by an increase in circumferential stiffness, however, the aneurysmal model was not found to be significantly different from the controls or AngII infused wild-type mice due to the high variability (**Figure 3B**). The axial stiffness tended to decrease with 14 days of AngII infusion for both wild-type and ApoE$^{-/-}$ mice, but then return closer to the stiffness found in the control mice after 28 days of AngII infusion (**Figure 3C**). The axial stiffness was significantly higher than the circumferential stiffness for both the control and

AngII infused wild-type mice groups, but this was not the case for either time point in the ApoE$^{-/-}$ AngII infused aneurysmal model.

B.4.3 Fiber alignment

SHG imaging showed differences in the collagen structure between the control mice and the ApoE$^{-/-}$ AngII infused aneurismal mice at both 14 and 28 day time points (**Figure 4**). Images show differences in the characteristic collagen crimp that is present in the control images before and during pressurization, which appears to be absent or greatly reduced in the ApoE$^{-/-}$ AngII infused aneurysm model. Representative histograms depicting the fiber angles compiled from each image stack at each pressurization (**Figure 5**) demonstrate a response in fiber orientation and dispersion occurred with pressurization for controls that was absent at both time points in the ApoE$^{-/-}$ AngII infused aneurysm model.

The histograms were used to determine fiber orientation mean mode and FWHM. From the FWHM (**Figure 6A**), the control mice showed a significant increase in fiber dispersion between 0 and 100 mmHg pressurization. An increase nearing significance also occurred in fiber dispersion for the 14 day AngII infused wild-type mice, but was absent in the 28 day AngII infused wild-type mice. The FWHM of ApoE$^{-/-}$ AngII aneurysmal mice at both time points did not express a significant change with pressurization, and at 0 mmHg the FWHM of the 28 day ApoE$^{-/-}$ AngII infused aneurysmal mice was significantly greater than control mice. The fiber directionality given by the mean mode (**Figure 6B**) showed a more axial alignment for control mice that shifted significantly towards axial alignment with pressurization, this axial shift also occurred for AngII infused wild-type mice at both 14 and 28 day time points, though it was not significant. The shift with pressurization tended to be reversed for the ApoE$^{-/-}$ AngII aneurysmal mice at 14 days, and absent at 28 days. Also for the ApoE$^{-/-}$ AngII aneurysmal mice at 28 days, the preferred axial alignment similarly reduced or absent.

Cross sectional images (**Figure 7**) illustrate the dissected aneurysmal sac that occurs in the ApoE$^{-/-}$ AngII aneurysmal model compared to control mice. ApoE$^{-/-}$ AngII

aneurysmal images also reveal the elastic bands that appear to remain intact for all groups, while exhibiting adventitial thickening occurring with aneurysm and increased collagen content for the 28 day ApoE$^{-/-}$ AngII aneurysmal mice.

B.5. Discussion

A summary of the results found that as one would expect, the aortic outer diameter of the aneurysmal model was significantly greater than controls. However, this increase only translated to a significant increase in aortic thickness for the 14 day ApoE$^{-/-}$ AngII infused aneurysmal mice and not to the 28 day ApoE$^{-/-}$ AngII infused aneurysmal mice suggesting that remodeling within the aortic aneurysmal wall is occurring between 14 and 28 days. This remodeling between 14 and 28 days in the aneurysmal model is also suggested by the change in axial stiffness that occurred between 14 and 28 days in the ApoE$^{-/-}$ AngII infused aneurysmal mice, as there was initially a decrease in axial stiffness that was approaching significance, yet at 28 days ApoE$^{-/-}$ AngII infused aneurysmal mice had axial stiffness values closer to those found in the control mice. This trend in decreased axial stiffness at 14 days which was then corrected at 28 days was also found to occur with AngII infusion of wild-type mice suggesting a response not just to aneurysm formation but also AngII indused remodeling as well. One difference that was found, though, between controls and AngII infused wild-type mice compared to the ApoE$^{-/-}$ AngII infused aneurysmal model present at both 14 and 28 day time points was the decrease in circumferential strain and increase in circumferential stiffness.

Multiphoton images showed alterations in fiber appearance in the ApoE$^{-/-}$ AngII infused aneurysmal model and a loss of the characteristic crimp seen in collagen fiber bundles. Both metrics of fiber angle mean mode and FWHM showed gross changes between control and ApoE$^{-/-}$ AngII infused aneurysmal mice. While the control mice were able to respond with increases in fiber dispersion and shifts in mean fiber angle in the direction of increased stress, the ApoE$^{-/-}$ AngII infused aneurysmal mice lacked this ability. Thus, changes in the ApoE$^{-/-}$ AngII infused aneurysmal mice fiber structure and

composition between time points appear to be compensation to the loss in function and ability to respond with shifts in mean fiber angle and dispersion to pressurization.

The ApoE$^{-/-}$ AngII mouse model of aneurysm has become a standard animal model for aneurysm with a plethora of papers just released within the past year examining multiple factors involved with AA formation, progression, or prevention,[208-211, 218, 219] and while many other recent papers examining the biology of AAA disease often implicate mechanics as being a factor,[10, 220, 221] the biaxial properties of the ApoE$^{-/-}$ AngII aneurysmal aorta had yet to be examined until now. While previous studies in our lab [215] and other others such as Collins et al.[214] and Fujikura et al.[222] have used wild-type C57BL/6 mice to look into the mechanical properties of the mouse aorta to gain a more complete picture of underlying properties of vessel response, these studies did not include specimens from the actual ApoE AngII infused aneurysm model. And although Collins et al. reported some histology, absent in both their work and that of Fujikura et al. is analysis of fiber microstructure simultaneously with biomechanical response.

One limitation of the study was the inherent uncertainty of the aortic thickness from which the mechanical results were determined, especially for the aneurysmal specimens as the wall thickness varied around perimeter of the aneurysm due to the dissection creating thicker regions which then had to be averaged. Also, thickness measurements were made from an annulus taken adjacent to the region tested, and although these still included aneurysmal portions of the ApoE$^{-/-}$ AngII infused mice, some imprecision may have been introduced. Also, use of a Fung-type exponential constitutive model comes with limitations such as a lack of ability to capture multiple convexities and can result in constitutive parameters that are not physically reasonable or unique.[173, 192]

Another limitation of the study included the tubular imaging of aneurysmal specimens being unable to penetrate through the entire thickness of the aortic wall. Even though multiphoton imaging offers advantages for deep tissue imaging, there was still significant signal loss deeper into the tissue, so that image stacks were kept to only 100 μm from the outside of the adventitia moving towards the media for analysis. However, while most imaging of mouse vascular walls has been conducted using cross-sectional

imaging,[200, 223, 224] tubular imaging is still preferable to cross-sectional imaging in order to evaluate collagen fiber structure that would not be visible in any other plane. Additionally, full cross-sectional images were unable to be obtained from all specimens. However, cross-sectional images that were able to be obtained suggest that much of the remodeling that occurred between the 14 and 28 day time points in the $ApoE^{-/-}$ AngII infused aneurysm model was primarily collagen remodeling and occurred in the adventitia and the intraluminal thrombus, a finding supported by Schriefl et al.[224] Thus, focusing our study on the collagen remodeling occurring in the adventitia though tubular imaging is appropriate in this case.

Future work focusing on the collagen fiber remodeling could be improved by implementing a constitutive model that includes fiber directionality such as that used by Collins et al.[214] or other more microstructurally based constitutive relationships.[181, 206] Such microstructurally based constitutive relationships could also help when comparisons are made between different aneurysm models and the human disease. One thing that our work here has indicated is that there seems to be response in the $ApoE^{-/-}$ AngII infused model by 28 days that is able to reverse some of the functional mechanical response lost at 14 days. This is similar to findings by Daugherty et al.[117], which showed through histology that after 84 days of AngII infusion there was considerable remodeling of aneurysmal tissue with thinning regions not found at 28 days. We know that this late stage response is happening in the $ApoE^{-/-}$ AngII mouse model and this does not happen in the human disease, so beyond a certain time point, the model may not be useful or appropriate for studying the human disease. Other authors have also found differences between the $ApoE^{-/-}$ AngII infused model and the human disease, such as Saraff et al.,[14] who found aortic dissection is a preceding factor in aneurysm formation in the $ApoE^{-/-}$ AngII infused model. Additionally, Schrifl et al.[224] found remodeling and fibrosis of the intraluminal thrombus in the $ApoE^{-/-}$ AngII infused model which could account for some of the recovered mechanical response. However, this does not mean that measurements taken at time of initial aneurysm formation may not be valuable in studying AAA.

Conclusions

In summary, our study, for the first time, quantified biaxial mechanical behavior of the ApoE$^{-/-}$ AngII infused model of aneurysm, while simultaneously quantifying changes in ECM microstructure at multiple time pints. We found that although a reduction in circumferential strain and an increase in circumferential stiffness continued between the 14 and 28 day time points, this was not the case in the axial direction. This return of some of the normal biomechanical function, in addition the continuing changes that occur in the microstructure suggest a restorative response that occurs in the ApoE$^{-/-}$ AngII infused model after the initial aneurysm formation. Although such finding may cause some reservations about using the ApoE$^{-/-}$ AngII infused aneurysmal model, it might be advantageous to direct future efforts toward understanding and promoting such remodeling, as such a restorative response could have a broader impart on treatments for the human disease. Nevertheless, we hope that the biomechanical material parameters and fiber analysis provided here is able to provide a basis for future work into modeling of aneurysmal progression the ApoE$^{-/-}$ AngII infused model of AAA.

B.6. Disclosure of Potential Conflicts of Interest

None of the authors have any conflict of interest.

B.7. Acknowledgments

The authors would like to acknowledge the support of the American Heart Association (GIA 10GRNT4580045 to JPVG), the National Science Foundation (CAREER 0644570 to JPVG), the help of Tom Doetschman and Connie Gard, the National Institutes of Health (HL92508), The Stephen Michael Schneider & The William J. "Billy" Gieszl Investigator Award (University of Arizona), and Arizona Biomedical Research Commission (#0901).

B.8. References

1. Grootenboer N, Bosch JL, Hendriks JM, van Sambeek MR. Epidemiology, aetiology, risk of rupture and treatment of abdominal aortic aneurysms: Does sex matter? *Eur J Vasc Endovasc Surg*. 2009;38:278-284
2. Vande Geest JP, Sacks MS, Vorp DA. The effects of aneurysm on the biaxial mechanical behavior of human abdominal aorta. *J Biomech*. 2006;39:1324-1334
3. Vorp DA. Biomechanics of abdominal aortic aneurysm. *J Biomech*. 2007;40:1887-1902
4. Daugherty A, Manning MW, Cassis LA. Angiotensin ii promotes atherosclerotic lesions and aneurysms in apolipoprotein e-deficient mice. *J Clin Invest*. 2000;105:1605-1612
5. Hans CP, Koenig SN, Huang N, Cheng J, Beceiro S, Guggilam A, Kuivaniemi H, Partida-Sanchez S, Garg V. Inhibition of notch1 signaling reduces abdominal aortic aneurysm in mice by attenuating macrophage-mediated inflammation. *Arterioscler Thromb Vasc Biol*.32:3012-3023
6. Iida Y, Xu B, Schultz GM, Chow V, White JJ, Sulaimon S, Hezi-Yamit A, Peterson SR, Dalman RL. Efficacy and mechanism of angiotensin ii receptor blocker treatment in experimental abdominal aortic aneurysms. *PLoS One*.7:e49642
7. Remus EW, O'Donnell RE, Jr., Rafferty K, Weiss D, Joseph G, Csiszar K, Fong SF, Taylor WR. The role of lysyl oxidase family members in the stabilization of abdominal aortic aneurysms. *Am J Physiol Heart Circ Physiol*.303:H1067-1075
8. Yao Y, Wang Y, Zhang Y, Li Y, Sheng Z, Wen S, Ma G, Liu N, Fang F, Teng GJ. In vivo imaging of macrophages during the early-stages of abdominal aortic aneurysm using high resolution mri in apoe mice. *PLoS One*.7:e33523
9. Ford MD, Black AT, Cao RY, Funk CD, Piomelli U. Hemodynamics of the mouse abdominal aortic aneurysm. *J Biomech Eng*.133:121008
10. Goergen CJ, Barr KN, Huynh DT, Eastham-Anderson JR, Choi G, Hedehus M, Dalman RL, Connolly AJ, Taylor CA, Tsao PS, Greve JM. In vivo quantification of murine aortic cyclic strain, motion, and curvature: Implications for abdominal aortic aneurysm growth. *J Magn Reson Imaging*.32:847-858
11. Collins MJ, Bersi M, Wilson E, Humphrey JD. Mechanical properties of suprarenal and infrarenal abdominal aorta: Implications for mouse models of aneurysms. *Med Eng Phys*.33:1262-1269
12. Haskett D, Speicher E, Fouts M, Larson D, Azhar M, Utzinger U, Vande Geest J. The effects of angiotensin ii on the coupled microstructural and biomechanical response of c57bl/6 mouse aorta. *J Biomech*. 2011;45:772-779
13. Barisione C, Charnigo R, Howatt DA, Moorleghen JJ, Rateri DL, Daugherty A. Rapid dilation of the abdominal aorta during infusion of angiotensin ii detected by noninvasive high-frequency ultrasonography. *J Vasc Surg*. 2006;44:372-376
14. Cassis LA, Gupte M, Thayer S, Zhang X, Charnigo R, Howatt DA, Rateri DL, Daugherty A. Ang ii infusion promotes abdominal aortic aneurysms independent of increased blood pressure in hypercholesterolemic mice. *Am J Physiol Heart Circ Physiol*. 2009;296:H1660-1665

15. Eagleton MJ, Ballard N, Lynch E, Srivastava SD, Upchurch GR, Jr., Stanley JC. Early increased mt1-mmp expression and late mmp-2 and mmp-9 activity during angiotensin ii induced aneurysm formation. *J Surg Res*. 2006;135:345-351
16. Keyes JT, Haskett D, Borowicz SM, Utzinger U, Azhar M, Vande Geest JP. Adaptation of a two-photon-microscope-interfacing planar biaxial device for the microstructural characterization of small tubular tissue specimens. *Journal of Biomechanical Engineering*. 2011;Jul; 133(7):075001
17. Keyes JT, Borowicz SM, Rader JH, Utzinger U, Azhar M, Vande Geest JP. Design and demonstration of a microbiaxial optomechanical device for multiscale characterization of soft biological tissues with two-photon microscopy. *Microsc Microanal*. 2011;17:167-175
18. Keyes JT, Borowicz SM, Rader JH, Utzinger U, Azhar M, Vande Geest JP. Design and demonstration of a microbiaxial optomechanical device for multiscale characterization of soft biological tissues with two-photon microscopy. *Microsc Microanal*.1-9
19. Kirkpatrick ND, Hoying JB, Botting SK, Weiss JA, Utzinger U. In vitro model for endogenous optical signatures of collagen. *J Biomed Opt*. 2006;11:054021
20. Eberth JF, Taucer AI, Wilson E, Humphrey JD. Mechanics of carotid arteries in a mouse model of marfan syndrome. *Ann Biomed Eng*. 2009;37:1093-1104
21. Schulze-Bauer CA, Regitnig P, Holzapfel GA. Mechanics of the human femoral adventitia including the high-pressure response. *Am J Physiol Heart Circ Physiol*. 2002;282:H2427-2440
22. Gleason RL, Wilson E, Humphrey JD. Biaxial biomechanical adaptations of mouse carotid arteries cultured at altered axial extension. *J Biomech*. 2007;40:766-776
23. Humphrey JD, Eberth JF, Dye WW, Gleason RL. Fundamental role of axial stress in compensatory adaptations by arteries. *J Biomech*. 2009;42:1-8
24. Debes JC, Fung YC. Biaxial mechanics of excised canine pulmonary arteries. *Am J Physiol*. 1995;269:H433-442
25. Fung Y. *Biomechanics: Mechanical properties of living tissues*. New York: Springer; 1993.
26. Vande Geest JP, Sacks MS, Vorp DA. Age dependency of the biaxial biomechanical behavior of human abdominal aorta. *J Biomech Eng*. 2004;126:815-822
27. Fung YC, Liu SQ. Determination of the mechanical properties of the different layers of blood vessels in vivo. *Proc Natl Acad Sci U S A*. 1995;92:2169-2173
28. Fornasa G, Clement M, Groyer E, Gaston AT, Khallou-Laschet J, Morvan M, Guedj K, Kaveri SV, Tedgui A, Michel JB, Nicoletti A, Caligiuri G. A cd31-derived peptide prevents angiotensin ii-induced atherosclerosis progression and aneurysm formation. *Cardiovasc Res*.94:30-37
29. Yang L, Zhou X, Guo R, Shi Y, Liang X, Heng X. Role of kruppel-like factor 2 and protease-activated receptor-1 in vulnerable plaques of apoe(-/-) mice and intervention with statin. *Can J Cardiol*. 2013
30. Deguchi JO, Huang H, Libby P, Aikawa E, Whittaker P, Sylvan J, Lee RT, Aikawa M. Genetically engineered resistance for mmp collagenases promotes abdominal

aortic aneurysm formation in mice infused with angiotensin ii. *Laboratory investigation; a journal of technical methods and pathology*. 2009;89:315-326

31. Sheth RA, Maricevich M, Mahmood U. In vivo optical molecular imaging of matrix metalloproteinase activity in abdominal aortic aneurysms correlates with treatment effects on growth rate. *Atherosclerosis*. 2010;212:181-187
32. Fujikura K, Luo J, Gamarnik V, Pernot M, Fukumoto R, Tilson MD, 3rd, Konofagou EE. A novel noninvasive technique for pulse-wave imaging and characterization of clinically-significant vascular mechanical properties in vivo. *Ultrason Imaging*. 2007;29:137-154
33. Lindeman JH, Ashcroft BA, Beenakker JW, van Es M, Koekkoek NB, Prins FA, Tielemans JF, Abdul-Hussien H, Bank RA, Oosterkamp TH. Distinct defects in collagen microarchitecture underlie vessel-wall failure in advanced abdominal aneurysms and aneurysms in marfan syndrome. *Proceedings of the National Academy of Sciences of the United States of America*. 2010;107:862-865
34. Schriefl AJ, Collins MJ, Pierce DM, Holzapfel GA, Niklason LE, Humphrey JD. Remodeling of intramural thrombus and collagen in an ang-ii infusion apoe-/- model of dissecting aortic aneurysms. *Thromb Res*.130:e139-146
35. Zoumi A, Lu X, Kassab GS, Tromberg BJ. Imaging coronary artery microstructure using second-harmonic and two-photon fluorescence microscopy. *Biophys J*. 2004;87:2778-2786
36. Gasser TC, Ogden RW, Holzapfel GA. Hyperelastic modelling of arterial layers with distributed collagen fibre orientations. *Journal of the Royal Society, Interface / the Royal Society*. 2006;3:15-35
37. Daugherty A, Rateri DL, Cassis LA. Role of the renin-angiotensin system in the development of abdominal aortic aneurysms in animals and humans. *Ann N Y Acad Sci*. 2006;1085:82-91
38. Saraff K, Babamusta F, Cassis LA, Daugherty A. Aortic dissection precedes formation of aneurysms and atherosclerosis in angiotensin ii-infused, apolipoprotein e-deficient mice. *Arterioscler Thromb Vasc Biol*. 2003;23:1621-1626

B.9. Figures and Legends

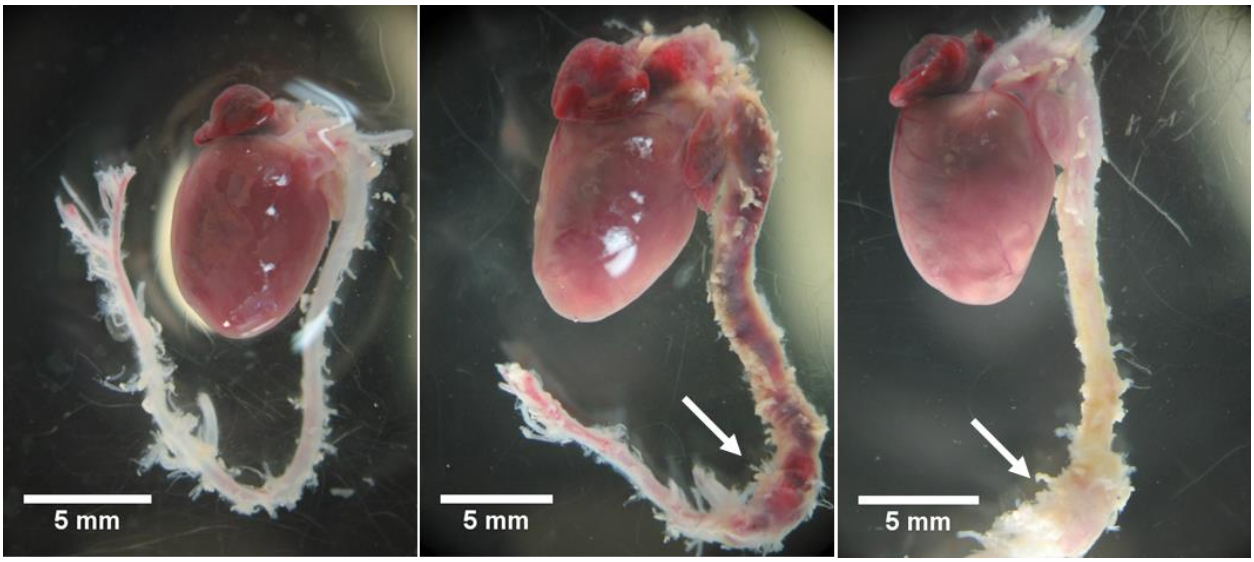

Figure 1: Representative aortas that have been removed and cleaned of excess connective tissue from a control mouse (Left), a 14 day ApoE$^{-/-}$ AngII infused aneurysmal mouse (Middle), and a 28 day ApoE$^{-/-}$ AngII infused aneurysmal mouse (Right). Arrows indicate an aneurysm in the suprarenal aortic region of the ApoE$^{-/-}$ AngII infused mouse that is absent in the wild-type saline infused mouse.

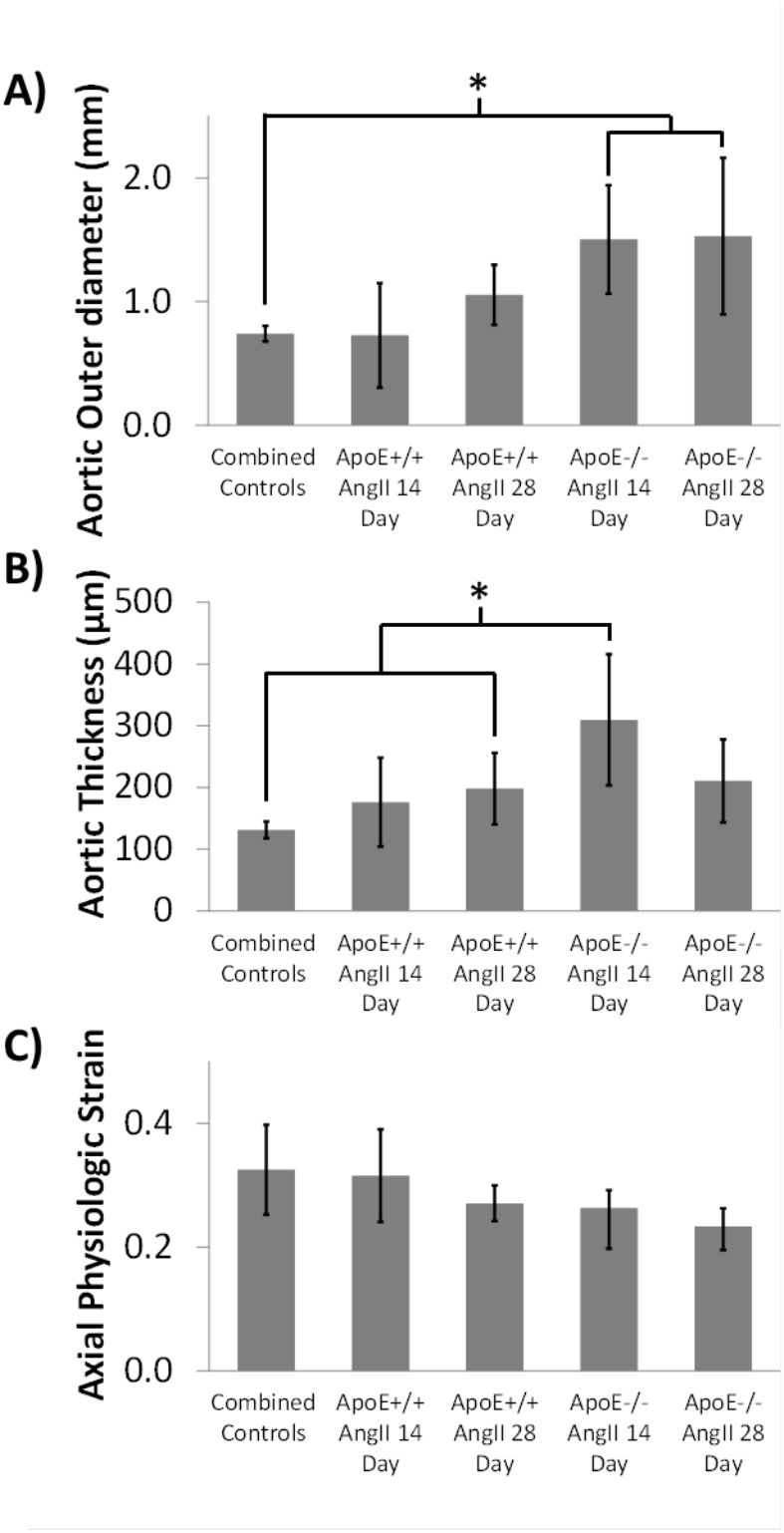
A)
Aortic Outer diameter (mm)
2.0
1.0
0.0
*
Combined Controls
ApoE+/+ AngII 14 Day
ApoE+/+ AngII 28 Day
ApoE-/- AngII 14 Day
ApoE-/- AngII 28 Day
B)
Aortic Thickness (µm)
500
400
300
200
100
0
*
Combined Controls
ApoE+/+ AngII 14 Day
ApoE+/+ AngII 28 Day
ApoE-/- AngII 14 Day
ApoE-/- AngII 28 Day
C)
Axial Physiologic Strain
0.4
0.2
0.0
Combined Controls
ApoE+/+ AngII 14 Day
ApoE+/+ AngII 28 Day
ApoE-/- AngII 14 Day
ApoE-/- AngII 28 Day

Figure 2: A) The initial unloaded outer diameter of the suprarenal segment of the aorta tested taken at its greatest point. B) The initial undeformed thickness of the suprarenal segment of the aorta taken adjacent to the section tested. C) The physiologic strain measured prior to mechanical testing. Error bars shown are standard deviation (* P<0.05).

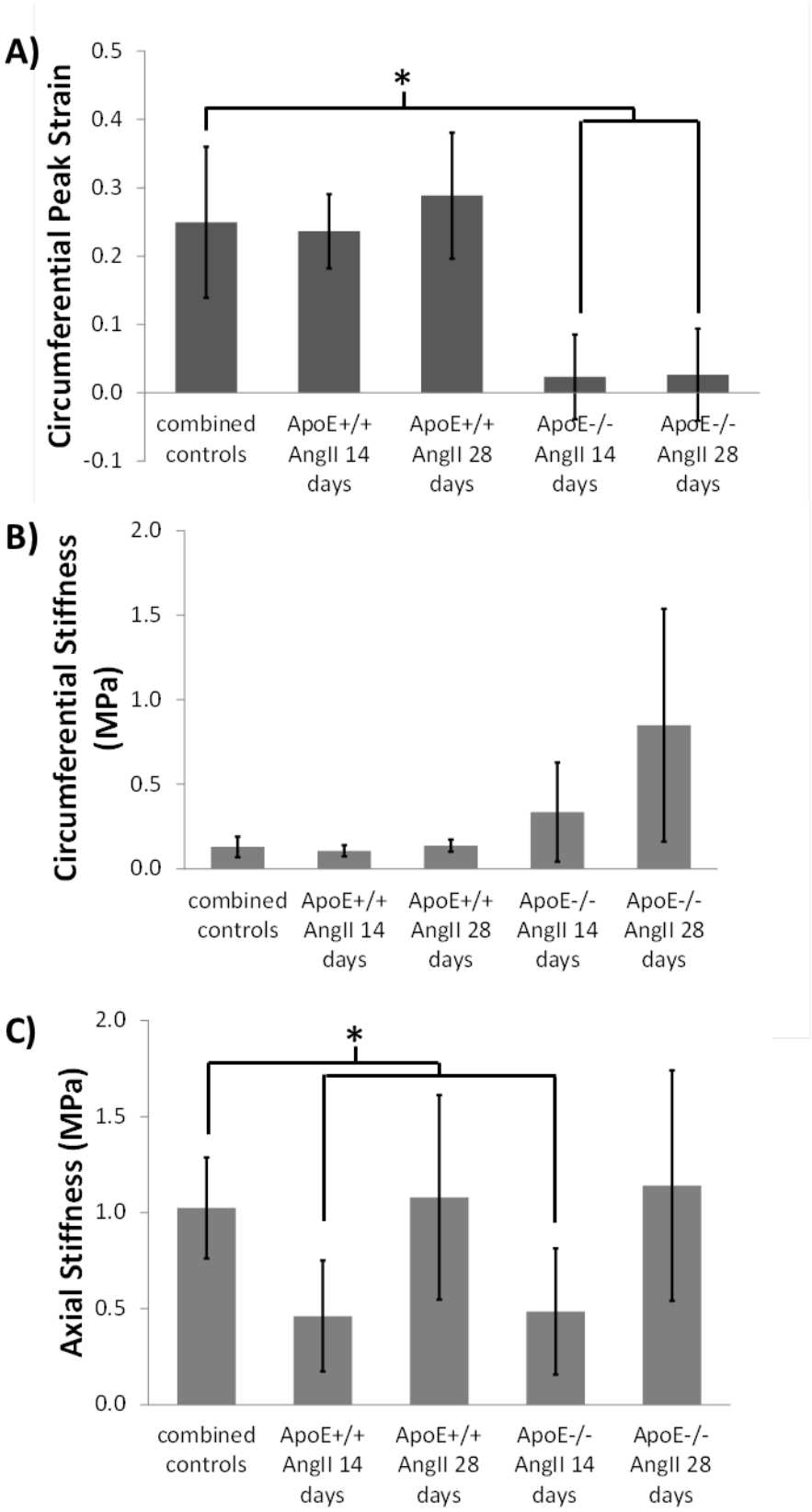
A)
Circumferential Peak Strain
0.5
0.4
0.3
0.2
0.1
0.0
-0.1
*
combined controls
ApoE+/+ AngII 14 days
ApoE+/+ AngII 28 days
ApoE-/- AngII 14 days
ApoE-/- AngII 28 days
B)
Circumferential Stiffness (MPa)
2.0
1.5
1.0
0.5
0.0
combined controls
ApoE+/+ AngII 14 days
ApoE+/+ AngII 28 days
ApoE-/- AngII 14 days
ApoE-/- AngII 28 days
C)
Axial Stiffness (MPa)
2.0
1.5
1.0
0.5
0.0
*
combined controls
ApoE+/+ AngII 14 days
ApoE+/+ AngII 28 days
ApoE-/- AngII 14 days
ApoE-/- AngII 28 days

Figure 3: A) The circumferential peak strain taken at the physiologic axial strain and pressurized to 100 mmHg. B and C) The circumferential stiffness and axial stiffness, respectively, defined as $\partial S/\partial E$ in the circumferential and axial directions at the physiologic axial strain and peak circumferential strain. Error bars shown are standard deviation (* P<0.05).

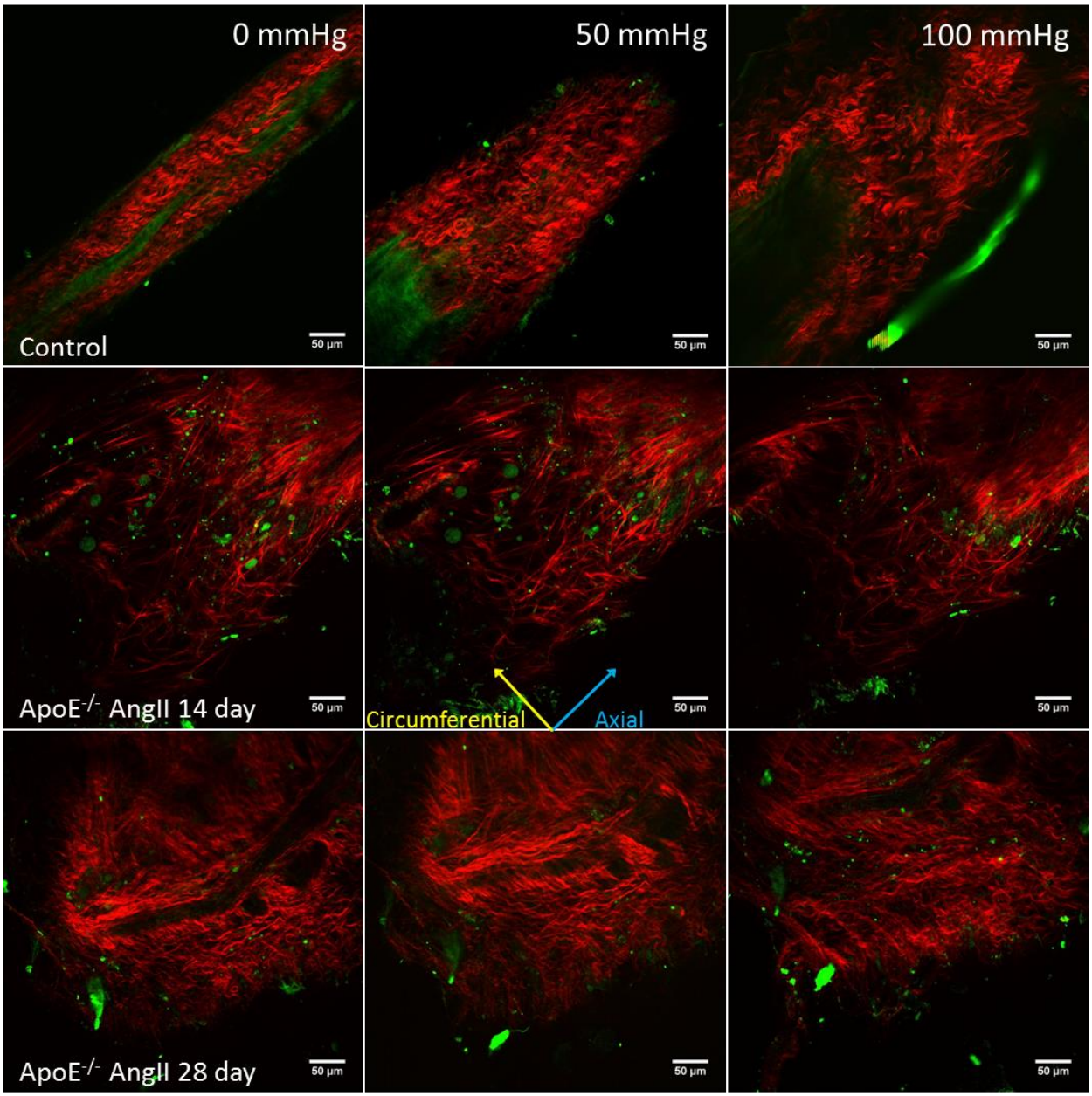

Figure 4: Representative multiphoton images of a control mouse aorta (Top), an ApoE$^{-/-}$ AngII mouse at 14 days (Middle), and ApoE$^{-/-}$ AngII infused mouse at 28 days pulled to the in vivo axial strain at both 0 mmHg (Left), 50 mmHg (Middle), and 100 mmHg (RIght). SHG channel (Red) represents the

collagen content of the aorta, while NADH channel (Green) represents primarily the elastin content or lipid deposits. While some of elastin bands of the media are observable in the control images, these images are taken approximately in the adventitial layer of the aorta, which was observed to be thicker in both the AngII infused wild-type mouse and the ApoE$^{-/-}$ AngII infused model. Blue and yellow arrows correspond to axial and circumferential directions respectively. In the saline mouse aorta the expected waviness of the collagen fiber bundles is evident in both unpressurized and pressurized states, while both the AngII infused wild-type mouse and the ApoE$^{-/-}$ AngII infused model aortas do not exhibit the expected waviness indicating collagen crimp.

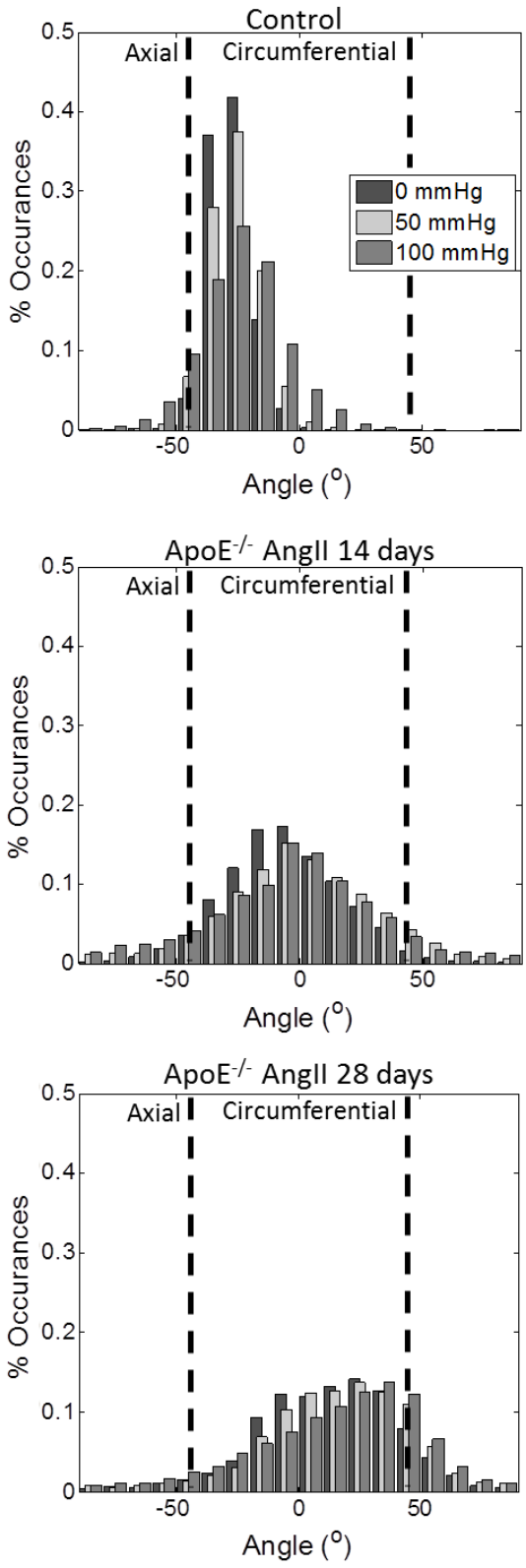
Control
Axial
Circumferential
0 mmHg
50 mmHg
100 mmHg
% Occurances
Angle (°)
ApoE-/- AngII 14 days
Axial
Circumferential
% Occurances
Angle (°)
ApoE-/- AngII 28 days
Axial
Circumferential
% Occurances
Angle (°)

Figure 5: Histogram bars show the overall collagen fiber orientations through the adventitial layer of the aorta at 0 mmHg (Left), 50 mmHg (Middle), and 100 mmHg (Right) pressurized states, with dashed bars representing axial and circumferential directions respectively.

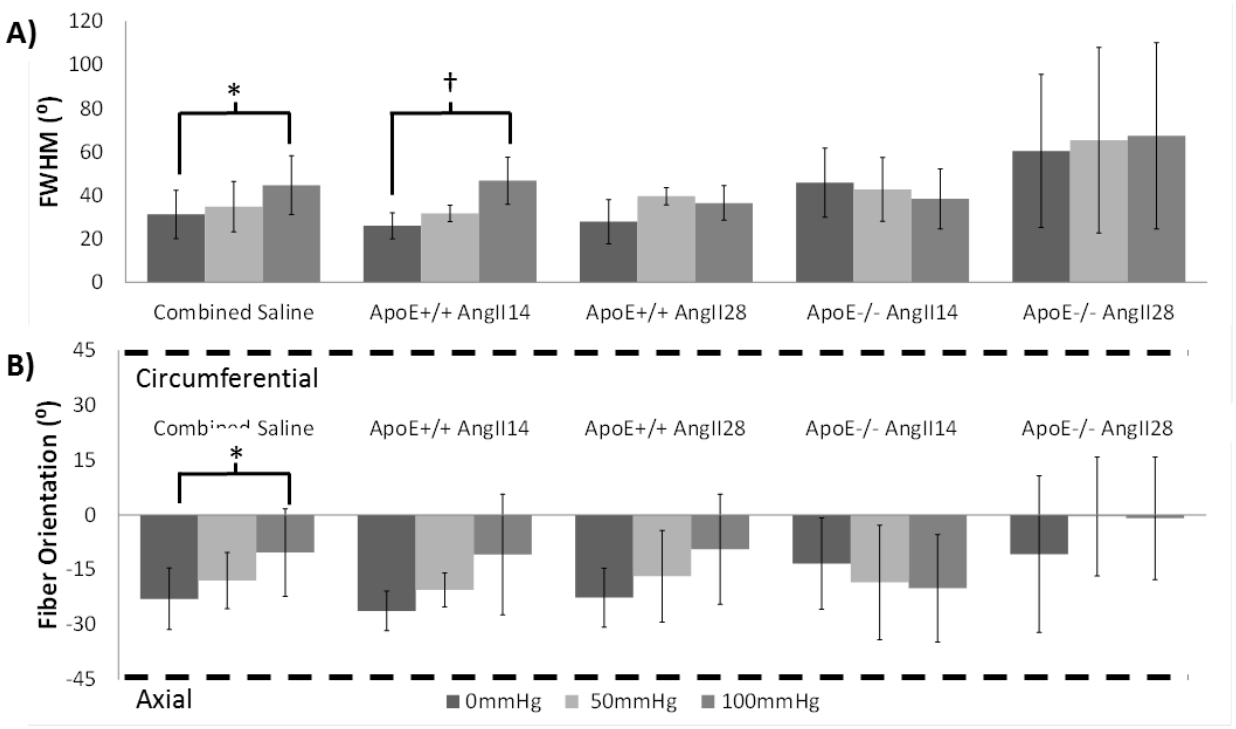

Figure 6: A) The FWHM represents the degree of fiber dispersion, with 0° corresponding fully aligned and 180° corresponding to no fiber alignment or full fiber dispersion. B) The fiber orientation mean mode in reference to -45° being the axial alignment and 45° being circumferential alignment (dashed bars) represents the collagen fibers preferred direction of alignment. Both tiles show the different pressurizations of 0 mmHg (Left), 50 mmHg (Middle), and 100 mmHg (Right). Error bars shown are standard deviation (* P<0.05).

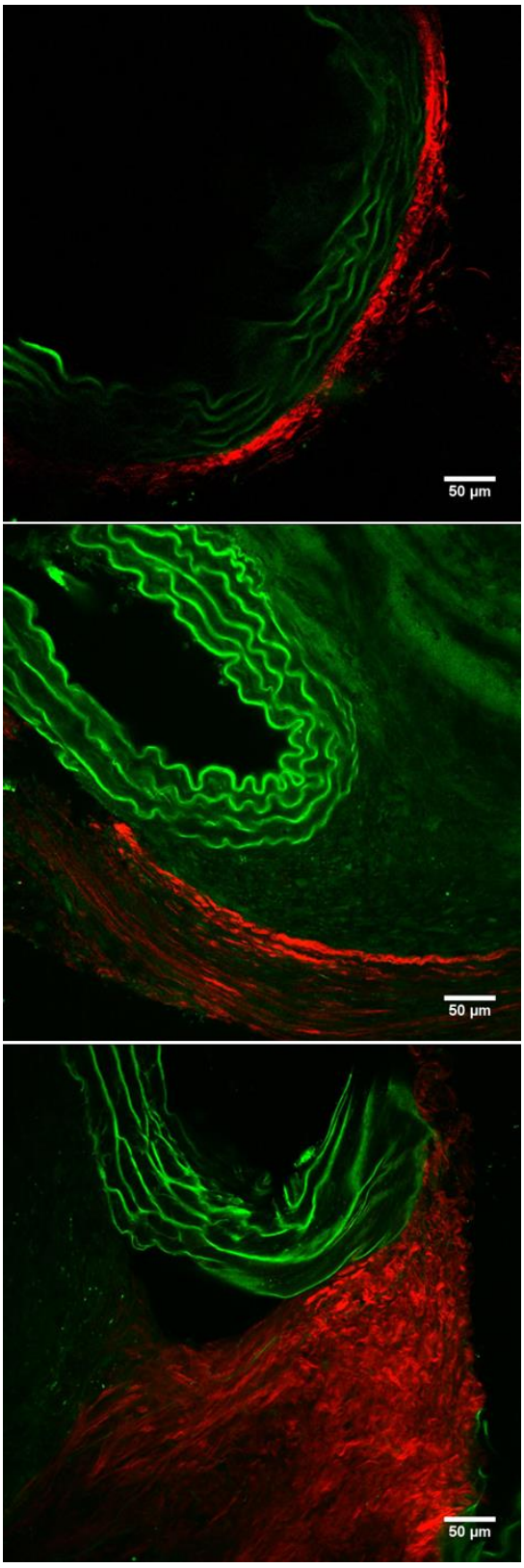
50 µm
50 µm
50 µm

Figure 7: Representative cross-sectional multiphoton images depicting the collagen (Red) found in the adventitia and elastin sheets or lipids (Green) of the media or dissected aneurysmal sacs for control (Top), ApoE$^{-/-}$ AngII infused model at 14 days (Middle), and ApoE$^{-/-}$ AngII infused model at 28 days (Bottom).

B.10. Tables with Captions

Table 1. Fung constants fit to the experimental data of control, AngII infused wild-type mice, and ApoE$^{-/-}$ AngII infused model, along with corresponding R^2 values. Descriptions for the material parameters are in section 2.3.

	C_0 (kPa)	a_1	a_2	a_{12}	R^2
Controls					
A	366.9	0.165	2.187	3.26E-02	0.97
B	229.6	0.225	4.879	1.67E-09	0.97
C	681.6	0.229	2.078	2.60E-02	0.99
D	123.6	0.0566	7.630	3.78E-01	0.95
E	128.8	0.480	5.445	1.86E-10	0.90
F	1713.3	0.00523	0.0607	2.22E-03	0.93
g	2391.0	0.0750	0.285	1.37E-02	0.97
h	5482.5	0.0328	0.115	4.43E-03	0.98
Wild-type AngII 14 days					
a	3838.0	0.0301	0.113	7.10E-04	0.96
b	2285.2	0.0328	0.213	1.90E-03	0.98
c	1297.7	1.17E-09	1.129	4.23E-02	0.95
d	5915.0	0.0243	0.123	2.51E-03	0.98
Wild-type AngII 28 days					
a	240.2	0.206	2.078	1.99E-02	0.91
b	886.8	0.177	0.409	4.20E-03	0.95
c	231.8	0.319	2.854	3.22E-10	0.98
d	200.9	0.437	3.185	1.03E-09	0.98
ApoE$^{-/-}$ AngII 14 days					
a	12.9	9.245	12.802	3.60E-01	0.85
b	356.2	1.900	0.881	4.90E-01	0.84
c	554.1	0.271	0.353	0.000714	0.96

ApoE$^{-/-}$ AngII 28 days					
a	11.2	12.317	19.74	8.05E+01	0.95
b	174.7	0.233	1.254	1.02E-09	0.95
c	297.2	4.865	1.556	7.43E-01	0.73

APPENDIX C: ANIMAL SUBJECTS APPROVAL

All animal use and experimental procedures for mouse testing were performed according to the approved protocols of the University of Arizona Institutional Animal Care and Use Committee ((UA protocols #06-045 & 06-064 to Tom Doetschman and his collaborators).

APPENDIX D: MATLAB CODES

ApoEmouse_complete_data_analyzer_circ_biax_test

Pathname:

Contents


```
clc

clear all
close all

filename = input('Mat File Name: ', 's');
FreeLength = input('Input the free length of the aorta: ');
no_tests = input('Input the number of Circ Pressure Tests: ');
%no_axial_tests = 1; %input('Input the number of Axial Pressure Tests: ');
```

determin the original aortic thickness

```
    [image1,PathName] = uigetfile('*.*', 'Pick a file', 'MultiSelect', 'on');
    curr_dir = pwd;
    cd(PathName);

    imread(image1);

    image2 = uigetfile('*.*', 'Pick a file', 'MultiSelect', 'on');
    imread(image2);

    imshow(image1)
    [x1 y1]=ginput(2);
    [x2 y2]=ginput(2);
    [x3 y3]=ginput(2);

    imshow(image2)
    [x4 y4]=ginput(2);
```

```
distance = [sqrt((x1(1,1)-x1(2,1))^2+(y1(1,1)-y1(2,1))^2) ...
        sqrt((x2(1,1)-x2(2,1))^2+(y2(1,1)-y2(2,1))^2) ...
        sqrt((x3(1,1)-x3(2,1))^2+(y3(1,1)-y3(2,1))^2)];

d_ave = mean(distance);

d4=sqrt((x4(1,1)-x4(2,1))^2+(y4(1,1)-y4(2,1))^2);

original_thickness = (1000*d_ave)/d4; %microns
aortic_thickness = original_thickness/1e3; %mm

%Determin opening angle
%image3 = uigetfile('*.*', 'Pick a file', 'MultiSelect', 'on');
%imread(image3);
%imshow(image3)
%[x5 y5]=ginput(3);

%A = [[x5(2,1) x5(1,1)];[y5(2,1) y5(1,1)]]
%B = [[x5(3,1) x5(1,1)];[y5(3,1) y5(1,1)]]
%Opening_angle =
```

import files for axial tests and take outer radius, pressure, load, and displacement data from test files

```
%     [filename1, pathname, filterindex] = uigetfile('*.*', 'Pick the Axial files ending in 3',
'MultiSelect', 'on'); %#ok<NASGU>
%     [filename2, pathname] = uigetfile('*.*', 'Pick the Axial files ending in 2',
'MultiSelect', 'on'); %#ok<NASGU>
%     [filename3, pathname] = uigetfile('*.*', 'Pick the Axial files ending in 1',
'MultiSelect', 'on'); %#ok<NASGU>
%
%     for i = 1:no_axial_tests
%     %outer radius
%         fileToRead=[]; %#ok<NASGU>
%         fileToRead=filename1{1,i};
%         importfile(fileToRead)
%         axial_test{1,i}.data1=data(:,8);
%
%     %pressure and load
%         fileToRead=filename2{1,i};
%         importfile(fileToRead)
%         axial_test{1,i}.data2=data(:,4);
%         axial_test{1,i}.data3=data(:,2);
```

```
%
%    %position
%       fileToRead=filename3{1,i};
%       importfile(fileToRead)
%       axial_test{1,i}.data4=data(:,2);
%       axial_test{1,i}.data4(1:4)= 0;
%       axial_test{1,i}.delta = max(axial_test{1,i}.data4);
%
%    end
```

import files for circ test and take outer radius, pressure, load, and displacement data from test files

```
    %outer radius
    [filename1, pathname] = uigetfile('*.*', 'Pick a Circ file ending in 3', 'MultiSelect',
'on'); %#ok<NASGU>
    fileToRead=[]; %#ok<NASGU>
    fileToRead=filename1;
    importfile(fileToRead)
    data1=data(:,8);

    %pressure and load
    [filename2, pathname] = uigetfile('*.*', 'Pick a Circ file ending in 2', 'MultiSelect',
'on'); %#ok<NASGU>
    fileToRead=filename2;
    importfile(fileToRead)
    data2=data(:,4);
    data3=data(:,2);

    %position
    [filename3, pathname] = uigetfile('*.*', 'Pick a Circ file ending in 1', 'MultiSelect',
'on');
    fileToRead=filename3;
    importfile(fileToRead)
    data4=data(:,2);
    data4(1:4)= 0;
    delta = max(data4);

    cd(curr_dir);
```

Determination of Hoop Stress/Green Strain test windows selected manually

```
    %shows figure to determine indices for the test
    figure(2)
```

```
    plot(data1(:,1))
    hold on
    plot(data2(:,1))

    %determines the mins and maxes of the test selected
    Input_array = input('Input points for pressure and outer radius measurements (array):
');
        %for roughly picking the test window and then determining the start and end points
        %radius_min_indices = find(data1 ==
min(data1(Input_array(1,1):Input_array(1,2),1)));
        %radius_max_indices = find(data1 ==
        %max(data1(Input_array(1,1):Input_array(1,2),1)));
```

Circumferential Stress Strain Determination

```
    for i = 1:no_tests
        circ_test{1,i}.Axial_Strain_Point = (1/2)*(((FreeLength+0.2*(i-
1)*delta)/FreeLength).^2-1);
        %calculate the Green Strain and Hoop Stress
        circ_test{1,i}.outer_radius = (data1(Input_array(1,(2*i-1)):Input_array(1,2*i),1));
        circ_test{1,i}.pressure = (data2(Input_array(1,(2*i-1)):Input_array(1,2*i),1));

        %calculate thickness at each axial strain step
        circ_test{1,i}.aortic_thickness = aortic_thickness - ((0.2*(i-
1)*delta*aortic_thickness)/(2*FreeLength));

        circ_test{1,i}.initial_radius =  min(circ_test{1,i}.outer_radius);
        circ_test{1,i}.original_radius = data1(Input_array(1));

        circ_test{1,i}.thickness = circ_test{1,i}.aortic_thickness - ...
                                (1/2)*((circ_test{1,i}.outer_radius-circ_test{1,i}.initial_radius)/ ...
                                 circ_test{1,i}.initial_radius)*circ_test{1,i}.aortic_thickness;

        circ_test{1,i}.Green_strain = (1/2)*(((circ_test{1,i}.outer_radius-
(circ_test{1,i}.thickness/2)).^2 ...
                                -(circ_test{1,i}.original_radius-(aortic_thickness/2))^2)/ ...
                                ((circ_test{1,i}.original_radius-(aortic_thickness/2))^2));

        circ_test{1,i}.inner_radius = circ_test{1,i}.outer_radius-circ_test{1,i}.thickness;
        circ_test{1,i}.pressure_Pa = 133.28*circ_test{1,i}.pressure;
        %circ_test{1,i}.hoop_stress
=(circ_test{1,i}.pressure_Pa.*circ_test{1,i}.inner_radius)./circ_test{1,i}.thickness; %thin
wall assumption
```

```
        circ_test{1,i}.hoop_stress =
(circ_test{1,i}.pressure_Pa.*(circ_test{1,i}.inner_radius).^2)./(circ_test{1,i}.outer_radius
.^2-circ_test{1,i}.inner_radius.^2)...

.*(1+circ_test{1,i}.outer_radius.^2./(circ_test{1,i}.inner_radius+circ_test{1,i}.aortic_thic
kness/2).^2); %thick walled vessel

        %determine the axial load at each strain step
        circ_test{1,i}.Current_Xsec_Area = pi*((circ_test{1,i}.outer_radius'/1e3).^2 ...
                        -(circ_test{1,i}.outer_radius'/1e3 -
circ_test{1,i}.aortic_thickness/1e6).^2); %meters squared
        circ_test{1,i}.Axial_load = 9.81*(data3(Input_array(1,(2*i-
1)):Input_array(1,2*i),1)/1e3); %newtons
        circ_test{1,i}.Axial_Stress =
(circ_test{1,i}.Axial_load'./circ_test{1,i}.Current_Xsec_Area)';

        %Remove outliers and fit the stress/strain
        circ_test{1,i}.Green_log = circ_test{1,i}.Green_strain<.55;
        circ_test{1,i}.new_circ_strain =
circ_test{1,i}.Green_strain(circ_test{1,i}.Green_log);
        circ_test{1,i}.new_circ_stress =
circ_test{1,i}.hoop_stress(circ_test{1,i}.Green_log);


        circ_test{1,i}.p_circ =
polyfit(circ_test{1,i}.new_circ_strain,circ_test{1,i}.new_circ_stress,3);
        circ_test{1,i}.d_circ = polyder(circ_test{1,i}.p_circ);
        circ_test{1,i}.Circ_mtm =
polyval(circ_test{1,i}.d_circ,max(circ_test{1,i}.new_circ_strain));
        circ_test{1,i}.Circ_max_strain = max(circ_test{1,i}.new_circ_strain);
    end
```

Axial Stress Strain Determination

```
    %determine time points for each axial displacement


    for k = 1:no_tests
        %determine time points for each axial displacement
        axial_test{1,k}.loc = (data4(Input_array(1,(2*k-1)):Input_array(1,2*k),1));


        %calculate the Green Strain and Hoop Stress
%         circ_test{1,i}.outer_radius = (data1(Input_array(1,(2*i-1)):Input_array(1,2*i),1));
```

```
%       circ_test{1,i}.pressure = (data2(Input_array(1,(2*i-1)):Input_array(1,2*i),1));


      axial_test{1,k}.Axial_Green_Strain = (1/2) * (((FreeLength +
axial_test{1,k}.loc(:))/FreeLength).^2 - 1);

      %determine stress during each axial displacement and filter data by removing
outliers
      axial_test{1,k}.Axial_outer_radius = data1(Input_array(1,(2*k-
1)):Input_array(1,2*k),1); %mm
      axial_test{1,k}.Axial_original_radius = data1(Input_array(1));
%axial_test{1,1}.Axial_outer_radius(1); %mm
      axial_test{1,k}.Axial_original_thickness = original_thickness;
      axial_test{1,k}.Axial_initial_thickness = original_thickness -
(1/2)*(((axial_test{1,k}.Axial_outer_radius(1)-
axial_test{1,k}.Axial_original_radius)/axial_test{1,k}.Axial_original_radius)*original_th
ickness); %microns
      axial_test{1,k}.Axial_thickness = axial_test{1,k}.Axial_initial_thickness -
(1/2)*((data4(Input_array(1,(2*k-
1)):Input_array(1,2*k),1)*axial_test{1,k}.Axial_initial_thickness)/FreeLength);
%microns
      axial_test{1,k}.Circ_Strain_Temp = (1/2) * (((axial_test{1,k}.Axial_outer_radius -
axial_test{1,k}.Axial_thickness(1,:)*1e-3)/(axial_test{1,k}.Axial_original_radius -
axial_test{1,k}.Axial_original_thickness*1e-3)).^2-1);

      %remove outliers
      axial_test{1,k}.Circ_Strain_Point = axial_test{1,k}.Circ_Strain_Temp;
         for n = 2:length(axial_test{1,k}.Circ_Strain_Temp)
            if abs(axial_test{1,k}.Circ_Strain_Temp(n)-
axial_test{1,k}.Circ_Strain_Point(n-1)) > 0.2; %#ok<ALIGN>
                  axial_test{1,k}.Circ_Strain_Point(n) = axial_test{1,k}.Circ_Strain_Point(n-
1);
            end
         end


      %axial_test{1,k}.Current_Xsec_Area = pi*((axial_test{1,k}.Axial_fitdata'/1e3).^2
...
                              %-(axial_test{1,k}.Axial_fitdata'/1e3 -
axial_test{1,k}.Axial_thickness/1e6).^2); %meters squared
      axial_test{1,k}.Current_Xsec_Area =
pi*((axial_test{1,k}.Axial_outer_radius/1e3).^2 ...
```

```
                        -(axial_test{1,k}.Axial_outer_radius/1e3 -
axial_test{1,k}.Axial_thickness/1e6).^2); %meters squared
      axial_test{1,k}.Axial_Load = 9.81*(data3(Input_array(1,(2*k-
1)):Input_array(1,2*k),1)/1e3); %newtons
      axial_test{1,k}.pressure = (data2(Input_array(1,(2*k-1)):Input_array(1,2*k),1));
      axial_test{1,k}.pressure_Pa = 133.28*axial_test{1,k}.pressure;
      axial_test{1,k}.Axial_Stress =
axial_test{1,k}.Axial_Load./axial_test{1,k}.Current_Xsec_Area;
          %+ (axial_test{1,k}.pressure_Pa * pi *(axial_test{1,k}.Axial_outer_radius/1e3
- axial_test{1,k}.Axial_thickness/1e6).^2)

      %Remove outliers and fit the stress/strain
      axial_test{1,k}.Axial_Green_log = axial_test{1,k}.Axial_Green_Strain<.6;
      axial_test{1,k}.Axial_new_strain =
axial_test{1,k}.Axial_Green_Strain(axial_test{1,k}.Axial_Green_log);
      axial_test{1,k}.Axial_new_stress =
axial_test{1,k}.Axial_Stress(axial_test{1,k}.Axial_Green_log);

      axial_test{1,k}.p_axial =
polyfit(axial_test{1,k}.Axial_new_strain,axial_test{1,k}.Axial_new_stress,3);
      axial_test{1,k}.d_axial = polyder(axial_test{1,k}.p_axial);

axial_test{1,k}.Axial_mtm=polyval(axial_test{1,k}.d_axial,max(axial_test{1,k}.Axial_n
ew_strain));
      axial_test{1,k}.Axial_Physio_strain=max(axial_test{1,k}.Axial_new_strain);

   end

%    axial_test{1,7}.difference = diff(data4);
%    axial_test{1,7}.loc = find(axial_test{1,7}.difference>0);
%
%    %determine strain for each axial displacement
%    axial_test{1,7}.Axial_Green_Strain = (1/2) * (((FreeLength +
data4(axial_test{1,7}.loc(:)))/FreeLength).^2 - 1);
%
%    %determine stress during each axial displacement
%    axial_test{1,7}.Axial_outer_radius = data1(axial_test{1,7}.loc(:)); %mm
%       %filter data by removing outliers then fit to a line
%       for i = 1:length(axial_test{1,7}.Axial_outer_radius)-1
%          if abs(axial_test{1,7}.Axial_outer_radius(i)-
axial_test{1,7}.Axial_outer_radius(i+1))>1
%             axial_test{1,7}.Axial_outer_radius(i) =
axial_test{1,7}.Axial_outer_radius(i-1); %#ok<AGROW>
```

```
%           end
%       end
%    axial_test{1,7}.Axial_polyfit =
polyfit([1:length(axial_test{1,7}.Axial_outer_radius)]',axial_test{1,7}.Axial_outer_radiu
s,1);
%    axial_test{1,7}.Axial_fitdata =
polyval(axial_test{1,7}.Axial_polyfit,1:length(axial_test{1,7}.Axial_outer_radius));
%    axial_test{1,7}.Axial_original_radius = min(axial_test{1,7}.Axial_fitdata); %mm
%
%    axial_test{1,7}.Axial_thickness = original_thickness -
(1/2)*(data1(axial_test{1,7}.loc(:))*original_thickness/FreeLength); %microns
%    axial_test{1,7}.Current_Xsec_Area = pi*((axial_test{1,7}.Axial_fitdata'/1e3).^2 ...
%                                -(axial_test{1,7}.Axial_fitdata'/1e3 -
axial_test{1,7}.Axial_thickness/1e6).^2); %meters squared
%    axial_test{1,7}.Axial_Load = 9.81*(data3(axial_test{1,7}.loc(:))/1e3); %newtons
%    axial_test{1,7}.Axial_Stress =
axial_test{1,7}.Axial_Load./axial_test{1,7}.Current_Xsec_Area;
%
%    %Remove outliers and fit the stress/strain
%    axial_test{1,7}.Axial_Green_log = axial_test{1,7}.Axial_Green_Strain<.9;
%    axial_test{1,7}.Axial_new_strain =
axial_test{1,7}.Axial_Green_Strain(axial_test{1,7}.Axial_Green_log);
%    axial_test{1,7}.Axial_new_stress =
axial_test{1,7}.Axial_Stress(axial_test{1,7}.Axial_Green_log);
%
%    axial_test{1,7}.p_axial =
polyfit(axial_test{1,7}.Axial_new_strain,axial_test{1,7}.Axial_new_stress,3);
%    axial_test{1,7}.d_axial = polyder(axial_test{1,7}.p_axial);
%
axial_test{1,7}.Axial_mtm=polyval(axial_test{1,7}.d_axial,max(axial_test{1,7}.Axial_n
ew_strain));
%    axial_test{1,7}.Axial_Physio_strain=max(axial_test{1,7}.Axial_new_strain);
```

Create figures and show desired outputs

```
%Plot circ stress/strain with fit
figure(3)
for i = 1:no_tests
    plot3(circ_test{1,i}.Axial_Strain_Point*ones(size(circ_test{1,i}.new_circ_strain)),...
        circ_test{1,i}.new_circ_strain,circ_test{1,i}.new_circ_stress,'bx','Markersize',10)
    hold on
    plot3(circ_test{1,i}.Axial_Strain_Point*ones(size(circ_test{1,i}.new_circ_strain)),...
```

```
circ_test{1,i}.new_circ_strain,polyval(circ_test{1,i}.p_circ,circ_test{1,i}.new_circ_strain
),'-r','LineWidth',2.5)
        hold on
    end
    %Set Text properties and Label axes
    xlabel('Axial Strain (E_z_z)','FontSize',16);
    ylabel('Circ Strain (E_\theta_\theta)','FontSize',16);
    set(gca,'YTick',0:0.2:1)
    zlabel('Hoop Stress (S_\theta_\theta, Pa)','FontSize',16);
    title(filename,'FontSize',20)
    axis([-0.1 0.5 -0.1 0.5 0 1e5])
    grid on

    saveas(3,[filename '_Circ figure.fig'])

    %Plot axial stress/strain with fit
    figure(4)
    for i = 1:no_tests

plot3(axial_test{1,i}.Circ_Strain_Point,axial_test{1,i}.Axial_new_strain,axial_test{1,i}.
Axial_new_stress,'bx','Markersize',10)
        hold on
%
plot3(axial_test{1,i}.Circ_Strain_Point,axial_test{1,i}.Axial_new_strain,polyval(axial_te
st{1,i}.p_axial,axial_test{1,i}.Axial_new_strain),'-r','LineWidth',2.5)
%         hold on
    end
%
plot3(axial_test{1,7}.Axial_new_strain,axial_test{1,7}.Axial_new_strain,axial_test{1,7}.
Axial_new_stress,'bx','Markersize',10)
%         hold on

    %Set Text properties and Label axes
    xlabel('Circ Strain (E_\theta_\theta)','FontSize',16);
    ylabel('Axial Strain (E_z_z)','FontSize',16);
    set(gca,'YTick',0:0.2:1)
    zlabel('Axial Stress (S_z_z, Pa)','FontSize',16);
    title(filename,'FontSize',20)
    axis([-0.1 0.5 -0.1 0.5 0 1e6])
    grid on
```

```
saveas(4,[filename '_Axial figure.fig'])
%save mat file
save ([filename], 'circ_test', 'axial_test', 'original_thickness', 'Input_array')
```

Published with MATLAB® R2015a

Constitutive_Combined_fit

Pathname:

Contents

Load and initialize data

```
clc

clear all
close all

%Let user select desired data to load and read
[filename, filepath]=uigetfile('.mat','Select data to be fitted');
load([filepath filename])

global totalSSR;
%Set recursive error limit for later fitting of data initially use 1e-6
Set=1e-6;

%Set number of weights to be considered at incriments of .02 to give 51
%weights between 0-1

% weight_res=.02;
% num_res=1/weight_res+1;
% weight_res=num_res;
%Predefine number of axial and circumferential tests
%no_test_ax=5;
no_test_circ= input('Input the number of Circ Pressure Tests: ');
Data_Structure=cell(1,2);
```

Create S and E matrices based off of Axial tests

```
%Define empty E and S data storage matrices
%aa-axial
%cc-circumferential

Eaa_Dat=[];
```

```
Ecc_Dat=[];
Saa_Dat=[];
Scc_Dat=[];

%Define x_mesh vector to be utilized in later surface plotting
%x1_mesh=zeros(1,no_test_ax);
%Read and Define various stress-strain values based upon input data loaded
%at begining of program
for i=1:no_test_circ
   %Construct vector of Eaa, Saa data points for fitting with fixed Ecc
   Eaa_Dat=[Eaa_Dat;axial_test{1,i}.Axial_new_strain(:,1)];
%#ok<*AGROW>

   Saa_temp=axial_test{1,i}.Axial_new_stress(:,1)./(1 +
2*(axial_test{1,i}.Axial_new_strain(:,1)));
   Saa_Dat=[Saa_Dat;Saa_temp];

   Ecc_Point=zeros(length(axial_test{1,i}.Axial_new_stress(:,1)),1);
   Ecc_Point(:,1)=axial_test{1,i}.Circ_Strain_Point;
   Ecc_Dat=[Ecc_Dat;Ecc_Point];
   %x1_mesh(i)=axial_test{1,i}.Circ_Strain_Point(:);

%    axial_test{1,i}.pressure=axial_test{1,i}.data2(axial_test{1,i}.loc(:));
%#ok<*SAGROW>
%    axial_test{1,i}.pressure(:)=133.28.*abs(axial_test{1,i}.pressure(:));
%#ok<SAGROW>
%    Scc_temp=(axial_test{1,i}.pressure.*(axial_test{1,i}.Axial_outer_radius.*1e3-
axial_test{1,i}.Axial_thickness)./axial_test{1,i}.Axial_thickness)./(1 +
2*(axial_test{1,i}.Circ_Strain_Point));
    Scc_temp=axial_test{1,i}.Axial_new_stress;

   if length(Scc_temp)~=length(axial_test{:,i}.Axial_new_stress(:,1))
      Scc_temp=Scc_temp(1:length(axial_test{:,i}.Axial_new_stress(:,1)),1);
   end
   Scc_Dat=[Scc_Dat;Scc_temp];
end
%Store aa and cc data into data structure for organizational purposes
Data_Structure{1,1}.S=[Saa_Dat Scc_Dat];
Data_Structure{1,1}.E=[Eaa_Dat Ecc_Dat];
```

Create S and E matrices based off of Circ tests

```
%To be completed once method of obtained Axial Stress from Circumferential
%data sets is determined
```

```
Eaa_Dat=[];
Ecc_Dat=[];
Saa_Dat=[];
Scc_Dat=[];

for i=1:no_test_circ
   %Construct vectors for Ecc, Saa, Scc, for fixed Eaa
   Ecc_Dat=[Ecc_Dat;circ_test{1,i}.new_circ_strain];

   Scc_temp=circ_test{1,i}.new_circ_stress./(1 + 2*(circ_test{1,i}.new_circ_strain));
   Scc_Dat=[Scc_Dat;Scc_temp];

   Eaa_Point=zeros(length(circ_test{1,i}.new_circ_strain),1);
   Eaa_Point(:,1)=circ_test{1,i}.Axial_Strain_Point;
   Eaa_Dat=[Eaa_Dat;Eaa_Point];

   if length(circ_test{:,i}.Axial_Stress)~=length(circ_test{:,i}.new_circ_strain)

circ_test{1,i}.Axial_Stress=circ_test{:,i}.Axial_Stress(1:length(circ_test{1,i}.new_circ_s
train),1);
   end
   Saa_temp=circ_test{1,i}.Axial_Stress./(1 + 2*(circ_test{1,i}.Axial_Strain_Point));
   Saa_Dat=[Saa_Dat;Saa_temp];

end

Data_Structure{1,2}.S=[Saa_Dat Scc_Dat];
Data_Structure{1,2}.E=[Eaa_Dat Ecc_Dat];
```

Generate iterative Fung fit based off of relative error

```
%Create vector of percentage weights to be utilized by fitting loop to
%account for varying importance of different directionality in the
%determination of appropriate constants in fung constituitive model

%weight_vect=linspace(0,1,weight_res)';
%create matrix for storage of constants for the fung model for the various
%weights used
A=ones(1,4);
%opt_sto=zeros(length(weight_vect),1);
%E=[Data_Structure{1,1}.E(:,1);Data_Structure{1,2}.E(:,2)];
%S=[Data_Structure{1,1}.S(:,1);Data_Structure{1,2}.S(:,2)];
```

```
E11=Data_Structure{1,2}.E(:,2); %Circumferential
E22=Data_Structure{1,1}.E(:,1); %Axial
S11=Data_Structure{1,2}.S(:,2); %Circumferential
S22=Data_Structure{1,1}.S(:,1); %Axial
E11 = interp1(linspace(0,1,length(E11)),E11,linspace(0,1,length(E22)))';
S11 = interp1(linspace(0,1,length(S11)),S11,linspace(0,1,length(S22)))';

A0=A;

A=fminsearch(@findtotalSSR,A0,[],E11,E22,S11,S22);

Data_Adjust=input('Are you inputting constants from SigmaStat? 1, yes, 0, no: ');

%Adjust Data if necessary
if Data_Adjust==1
   A=A0;
   A=input('input the coefficient values acquired from sigma stat: ');
else
   A=A;
end

%cd(filepath) %change directory for file saving
```

Create Comparison plot for Axial Data fit

```
figure(1)

%Generate y_mesh to be used for plotting surface
% y_mesh=linspace(0,1.05.*max(Data_Structure{1,1}.E(:,1)),20)';
%Plot original axial data as 3-D line plot
L= [min(Data_Structure{1,1}.E(:,2)) max(Data_Structure{1,1}.E(:,2))];
l=diff(L)/50; %circumferential
m=Data_Structure{1,1}.E(length(Data_Structure{1,1}.E(:,1)),1)/50; %axial
[J,K] =
meshgrid(min(Data_Structure{1,1}.E(:,2)):l:max(Data_Structure{1,1}.E(:,2)),0:m:Data_
Structure{1,1}.E(length(Data_Structure{1,1}.E(:,1)),1));

j_mesh=J; %circumferential
k_mesh=K; %axial

Saa_eq_surf=zeros(size(j_mesh));

for i=1:length(j_mesh(:,1))
```

```
    Q=A(1,2).*k_mesh(i,:).^2+A(1,3).*j_mesh(i,:).^2+
2*A(1,4).*k_mesh(i,:).*j_mesh(i,:);
    S11_eq=A(1,1).*(A(1,2).*k_mesh(i,:)+A(1,4).*j_mesh(i,:)).*exp(Q);

    Saa_eq_surf(i,:)=S11_eq;
end
surf(j_mesh,k_mesh,Saa_eq_surf)
hold on
plot3(Data_Structure{1,1}.E(:,2),Data_Structure{1,1}.E(:,1),Data_Structure{1,1}.S(:,1),'
bo')
% x=[];
% y=[];
% Saa_eq_surf=[];
% Scc_eq_surf=[];
% for i=1:no_test_ax
%     Ecc_Point=zeros(length(axial_test{1,i}.Axial_new_stress(:,1)),1);
%     Ecc_Point(:,1)=x1_mesh(i);
%
%
plot3(Ecc_Point(:,1),axial_test{1,i}.Axial_new_strain(:,1),axial_test{1,i}.Axial_new_stre
ss(:,1),'ob')
%     hold on
%     x=[x Ecc_Point(:,1)];
%      y=[y axial_test{1,i}.Axial_new_strain(:,1)];
%      S_eq=Fung_eq(A,[],[y(:,i) x(:,i)]);
%      Saa_eq_surf(:,i)=S_eq(:,1);
%      Scc_eq_surf(:,i)=S_eq(:,2);
% end
% surf(x,y,Saa_eq_surf)

ylabel('E_z_z','FontSize',14),xlabel('E_\theta_\theta','FontSize',14),zlabel('S_z_z','FontSiz
e',14)
xlim([-0.1 .5]),ylim([0 .5]),zlim([0 1e6])
grid on
h = figure(1);
saveas(h,strcat(filename,'_Axial.fig'),'fig')
```

Plot circ data

```
figure(2)

d=max(Data_Structure{1,2}.E(:,1))/50; %axial
f=max(Data_Structure{1,2}.E(:,2))/50; %circumferential
```

```
[X,Y] =
meshgrid(0:f:max(Data_Structure{1,2}.E(:,2)),0:d:max(Data_Structure{1,2}.E(:,1)));
%d=Data_Structure{1,2}.E(length(Data_Structure{1,2}.E(:,1)),1)/50; %axial
%f=Data_Structure{1,2}.E(length(Data_Structure{1,2}.E(:,1)),2)/50; %circumferential
%[X,Y] =
meshgrid(0:f:Data_Structure{1,2}.E(length(Data_Structure{1,2}.E(:,1)),2),0:d:Data_Stru
cture{1,2}.E(length(Data_Structure{1,2}.E(:,1)),1));

x_mesh=X; %circumferential
y_mesh=Y; %axial

Scc_eq_surf=zeros(size(x_mesh));

%S22_eq2=A(1,1)*(A(1,3).*x_mesh+A(1,4).*y_mesh)*exp(A(1,2).*y_mesh.^2+A(1,3).
*x_mesh.^2+ 2*A(1,4).*y_mesh.*x_mesh);

for i=1:length(x_mesh(:,1))
   Q=A(1,2).*y_mesh(i,:).^2+A(1,3).*x_mesh(i,:).^2+
2*A(1,4).*y_mesh(i,:).*x_mesh(i,:);
   S22_eq=A(1,1).*(A(1,3).*x_mesh(i,:)+A(1,4).*y_mesh(i,:)).*exp(Q);
   %S_eq=findtotalSSR(A,[],x_mesh(i,:),y_mesh(i,:),S11,S22)
   %S_eq=Fung_eq(A,[],[x_mesh(i,:)' y_mesh(i,:)']);
   Scc_eq_surf(i,:)=S22_eq;
end
surf(y_mesh,x_mesh,Scc_eq_surf)
hold on
plot3(Data_Structure{1,2}.E(:,1),Data_Structure{1,2}.E(:,2),Data_Structure{1,2}.S(:,2),'
bo')
xlabel('E_z_z','FontSize',14),ylabel('E_\theta_\theta','FontSize',14),zlabel('S_\theta_\theta'
,'FontSize',14)
xlim([0 .5]),ylim([-0.1 .5]),zlim([0 1e5])
grid on

h = figure(2);
saveas(h,strcat(filename,'_Circ.fig'),'fig')
```

Compute Axial and Circ Stiffnesses

```
S11_Epeak = Data_Structure{1,1}.E(length(Data_Structure{1,1}.E),:);

S22_Epeak = Data_Structure{1,2}.E(length(Data_Structure{1,2}.E),:);
```

```
Axial_Stiffness = A(1,1) * (A(1,2)*S11_Epeak(1,1) + A(1,4)*S11_Epeak(1,2)) *
(2*A(1,2)*S11_Epeak(1,1) + 2*A(1,4)*S11_Epeak(1,2))...
   *exp(A(1,2)*S11_Epeak(1,1)^2 + A(1,3)*S11_Epeak(1,2)^2 +
2*A(1,4)*S11_Epeak(1,1)*S11_Epeak(1,2))...
   +(A(1,1)*A(1,2))*exp(A(1,2)*S11_Epeak(1,1)^2 + A(1,3)*S11_Epeak(1,2)^2 +
2*A(1,4)*S11_Epeak(1,1)*S11_Epeak(1,2));
Circ_Stiffness = A(1,1) * (A(1,3)*S22_Epeak(1,2) + A(1,4)*S22_Epeak(1,1)) *
(2*A(1,3)*S22_Epeak(1,2) + 2*A(1,4)*S22_Epeak(1,1))...
   *exp(A(1,2)*S22_Epeak(1,1)^2 + A(1,3)*S22_Epeak(1,2)^2 +
2*A(1,4)*S22_Epeak(1,1)*S22_Epeak(1,2))...
   +(A(1,1)*A(1,3))*exp(A(1,2)*S22_Epeak(1,1)^2 + A(1,3)*S22_Epeak(1,2)^2 +
2*A(1,4)*S22_Epeak(1,1)*S22_Epeak(1,2));
Peak_Axial_Strain = S11_Epeak(1,1);
Peak_Circ_Strain = S22_Epeak(1,2);

S_Peak_Axial_fit=A(1,1)*(A(1,2)*y_mesh(51,51)+A(1,4)*x_mesh(51,51))*(2*A(1,2)*y
_mesh(51,51)+A(1,4)*x_mesh(51,51))*exp(A(1,2)*y_mesh(51,51)^2+A(1,3)*x_mesh(5
1,51)^2+ 2*A(1,4)*y_mesh(51,51)*x_mesh(51,51));
S_Peak_Circ_fit=A(1,1)*(A(1,3)*x_mesh(51,51)+A(1,4)*y_mesh(51,51))*(2*A(1,3)*x_
mesh(51,51)+A(1,4)*y_mesh(51,51))*exp(A(1,2)*y_mesh(51,51)^2+A(1,3)*x_mesh(51,
51)^2+ 2*A(1,4)*y_mesh(51,51)*x_mesh(51,51));


% Axial_Stiffness =
A(1,1)*(A(1,2)*Data_Structure{1,1}.E(length(Data_Structure{1,1}.E),1)+A(1,4)*Data_
Structure{1,1}.E(length(Data_Structure{1,1}.E),2))*(2*A(1,2)*Data_Structure{1,1}.E(le
ngth(Data_Structure{1,1}.E),1) ...
%
+2*A(1,4)*Data_Structure{1,1}.E(length(Data_Structure{1,1}.E),2))*exp(A(1,2)*Data_
Structure{1,1}.E(length(Data_Structure{1,1}.E),1)^2 +
A(1,3)*Data_Structure{1,1}.E(length(Data_Structure{1,1}.E),2)^2 ...
%           +
2*A(1,4)*Data_Structure{1,1}.E(length(Data_Structure{1,1}.E),1)*Data_Structure{1,1}.
E(length(Data_Structure{1,1}.E),2));
% Circ_Stiffness =
A(1,1)*(A(1,3)*max(E22)+A(1,4)*max(E11))*(2*A(1,3)*max(E22)+2*A(1,4)*max(E11
))*exp(A(1,2)*max(E11)^2 + A(1,3)*max(E22)^2 + 2*A(1,4)*max(E11)*max(E22));

save (filename)
```

Published with MATLAB® R2015a

Importfile

Pathname:

```
function importfile(fileToRead)
%IMPORTFILE1(FILETOREAD1)
%  Imports data from the specified file
%  FILETOREAD1:  file to read

%  Auto-generated by MATLAB on 25-Mar-2010 14:52:45

DELIMITER = '\t';
HEADERLINES = 22;

% Import the file
newData1 = importdata(fileToRead, DELIMITER, HEADERLINES);

% Create new variables in the base workspace from those fields.
vars = fieldnames(newData1);
for i = 1:length(vars)
    assignin('base', vars{i}, newData1.(vars{i}));
end
```

Published with MATLAB® R2015a

findtotalSSR

Pathname:

```
function totalSSR=findtotalSSR(a,E11,E22,S11,S22)



C1=a(1);a1=a(2);a2=a(3);a12=a(4);
% Q=a1.*E11.^2+a2.*E22.^2+ 2*a12.*E11.*E22;
%
% S11_eq=C1.*(a1.*E11+a12.*E22).*exp(Q);
% S22_eq=C1.*(a2.*E22+a12.*E11).*exp(Q);

%If coupled fitting does not produce acceptable fits, comment out Q and
%stress equations and uncomment the uncoupled equations below

S11_eq=C1.*((a1.*E11).*exp(0.5*a1.*E11.^2)+(a12.*E22).*exp(a12.*(E11.*E22)));
S22_eq=C1.*((a2.*E22).*exp(0.5*a2.*E22.^2)+(a12.*E11).*exp(a12.*(E11.*E22)));

SSR1= sum((S11_eq - S11).^2);
SSR2= sum((S22_eq - S22).^2);

global totalSSR %#ok<REDEF>

totalSSR=SSR1+SSR2;

end
```

Published with MATLAB® R2015a

Norm_Dist_Fit

Pathname:

```
%Normal Distribution Fitting Tool
%Greg Johnson 1/15/10

clear all
clc

filename = uigetfile('*.*', 'Pick a file', 'MultiSelect', 'on');
load(filename)
k = input('Input the number slides in the stack: ');

tot_angles=[];
for i=1:k
   angles=Data(1,i).Meas.Orientation.Angles;
   tot_angles=[tot_angles angles']; %#ok<AGROW>
end
%Var to be used Ang2_13days490ng_70mmHg_angles
Data1=tot_angles;
%User Determine if Data needs to be adjusted
Data_Adjust=input('Does Data need to be adjusted? 1, yes, 0, no: ');

%Adjust Data if necessary
if Data_Adjust==1
   %Determine angles above 90 deg to be adjusted
   ang_above=Data1>=90;
   %Adjust Data
   Data1(ang_above)=Data1(ang_above)-180;
   bins=[-90 -80];
else
   bins=[0 10];
end

%Generate histogram Data
for i=1:18
   temp=Data1>=bins(1)&Data1<bins(2);
   histo_dat(i)=length(nonzeros(temp)); %#ok<AGROW>
   bins=bins+10;
end
%Normalize histo_dat
histo_dat=histo_dat/sum(histo_dat);
%generate total bins
```

```
if Data_Adjust==1
   bin_plot=-85:10:85;
else
   bin_plot=5:10:175;
end


%plot histogram
hold on
figure(3)
bar(bin_plot,histo_dat)
xlabel('Angle (^0)','FontSize',16),...
ylabel('% Occurances','FontSize',16),...
ylim([0 0.5])
saveas(3,[filename '_histogram.fig'])

FWHM = fwhm(bin_plot,histo_dat)
Angle = mean(Data1)

save ([filename '.mat'], 'FWHM', 'Angle')
```

Published with MATLAB® R2015a

Importfile

Pathname:

```
function importfile(fileToRead)
%IMPORTFILE(FILETOREAD1)
%  Imports data from the specified file
%  FILETOREAD1:  file to read

%  Auto-generated by MATLAB on 17-May-2010 15:27:58

% Import the file
Data = load('-mat', fileToRead);

% Create new variables in the base workspace from those fields.
vars = fieldnames(Data);
for i = 1:length(vars)
    assignin('base', vars{i}, Data.(vars{i}));
end
```

Published with MATLAB® R2015a

Fwhm

Pathname:

```
function importfile(fileToRead)
%IMPORTFILE(FILETOREAD1)
%  Imports data from the specified file
%  FILETOREAD1:  file to read

%  Auto-generated by MATLAB on 17-May-2010 15:27:58

% Import the file
Data = load('-mat', fileToRead);

% Create new variables in the base workspace from those fields.
vars = fieldnames(Data);
for i = 1:length(vars)
    assignin('base', vars{i}, Data.(vars{i}));
end
```

Published with MATLAB® R2015a

Constitutive_Combined_fit_Holzapfel_with_mesh

Pathname:

Contents

Load and initialize data

```
clc

clear all
close all

%Let user select desired data to load and read
[filename, filepath]=uigetfile('.mat','Select data to be fitted');
load([filepath filename])

global totalSSR A E11 E22 S11 S22 lb ub
global S11m S22m

%Set recursive error limit for later fitting of data initially use 1e-6
Set=1e-6;

%Set number of weights to be considered at incriments of .02 to give 51
%weights between 0-1

% weight_res=.02;
% num_res=1/weight_res+1;
% weight_res=num_res;
%Predefine number of axial and circumferential tests
%no_test_ax=5;
no_test_circ= input('Input the number of Circ Pressure Tests: ');
Data_Structure=cell(1,2);
```

Create S and E matrices based off of Axial tests

```
%Define empty E and S data storage matrices
%aa-axial
%cc-circumferential
```

```
Eaa_Dat=[];
Ecc_Dat=[];
Saa_Dat=[];
Scc_Dat=[];

%Define x_mesh vector to be utilized in later surface plotting
%x1_mesh=zeros(1,no_test_ax);
%Read and Define various stress-strain values based upon input data loaded
%at begining of program
for i=1:no_test_circ
   %Construct vector of Eaa, Saa data points for fitting with fixed Ecc
   Eaa_Dat=[Eaa_Dat;axial_test{1,i}.Axial_new_strain(:,1)];
%#ok<*AGROW>

   Saa_temp=axial_test{1,i}.Axial_new_stress(:,1)./(1 +
2*(axial_test{1,i}.Axial_new_strain(:,1)));
   Saa_Dat=[Saa_Dat;Saa_temp];

   Ecc_Point=zeros(length(axial_test{1,i}.Axial_new_stress(:,1)),1);
   Ecc_Point(:,1)=axial_test{1,i}.Circ_Strain_Point;
   Ecc_Dat=[Ecc_Dat;Ecc_Point];
   %x1_mesh(i)=axial_test{1,i}.Circ_Strain_Point(:);

%    axial_test{1,i}.pressure=axial_test{1,i}.data2(axial_test{1,i}.loc(:));
%#ok<*SAGROW>
%    axial_test{1,i}.pressure(:)=133.28.*abs(axial_test{1,i}.pressure(:));
%#ok<SAGROW>
%    Scc_temp=(axial_test{1,i}.pressure.*(axial_test{1,i}.Axial_outer_radius.*1e3-
axial_test{1,i}.Axial_thickness)./axial_test{1,i}.Axial_thickness)./(1 +
2*(axial_test{1,i}.Circ_Strain_Point));
    Scc_temp=axial_test{1,i}.Axial_new_stress;

   if length(Scc_temp)~=length(axial_test{:,i}.Axial_new_stress(:,1))
      Scc_temp=Scc_temp(1:length(axial_test{:,i}.Axial_new_stress(:,1)),1);
   end
   Scc_Dat=[Scc_Dat;Scc_temp];
end
%Store aa and cc data into data structure for organizational purposes
Data_Structure{1,1}.S=[Saa_Dat Scc_Dat];
Data_Structure{1,1}.E=[Eaa_Dat Ecc_Dat];
```

Create S and E matrices based off of Circ tests

```
%To be completed once method of obtained Axial Stress from Circumferential
%data sets is determined

Eaa_Dat=[];
Ecc_Dat=[];
Saa_Dat=[];
Scc_Dat=[];

for i=1:no_test_circ
   %Construct vectors for Ecc, Saa, Scc, for fixed Eaa
   Ecc_Dat=[Ecc_Dat;circ_test{1,i}.new_circ_strain];

   Scc_temp=circ_test{1,i}.new_circ_stress./(1 + 2*(circ_test{1,i}.new_circ_strain));
   Scc_Dat=[Scc_Dat;Scc_temp];

   Eaa_Point=zeros(length(circ_test{1,i}.new_circ_strain),1);
   Eaa_Point(:,1)=circ_test{1,i}.Axial_Strain_Point;
   Eaa_Dat=[Eaa_Dat;Eaa_Point];

   if length(circ_test{:,i}.Axial_Stress)~=length(circ_test{:,i}.new_circ_strain)

circ_test{1,i}.Axial_Stress=circ_test{:,i}.Axial_Stress(1:length(circ_test{1,i}.new_circ_s
train),1);
   end
   Saa_temp=circ_test{1,i}.Axial_Stress./(1 + 2*(circ_test{1,i}.Axial_Strain_Point));
   Saa_Dat=[Saa_Dat;Saa_temp];

end

Data_Structure{1,2}.S=[Saa_Dat Scc_Dat];
Data_Structure{1,2}.E=[Eaa_Dat Ecc_Dat];
```

Generate iterative Fung fit based off of relative error

```
%Create vector of percentage weights to be utilized by fitting loop to
%account for varying importance of different directionality in the
%determination of appropriate constants in fung constituitive model

%weight_vect=linspace(0,1,weight_res)';
%create matrix for storage of constants for the fung model for the various
%weights used
A=ones(1,6);
```

```
%opt_sto=zeros(length(weight_vect),1);
%E=[Data_Structure{1,1}.E(:,1);Data_Structure{1,2}.E(:,2)];
%S=[Data_Structure{1,1}.S(:,1);Data_Structure{1,2}.S(:,2)];

E11=Data_Structure{1,2}.E(:,2); %Circumferential
E22=Data_Structure{1,1}.E(:,1); %Axial
S11=Data_Structure{1,2}.S(:,2); %Circumferential
S22=Data_Structure{1,1}.S(:,1); %Axial
E11 = interp1(linspace(0,1,length(E11)),E11,linspace(0,1,length(E22)))';
S11 = interp1(linspace(0,1,length(S11)),S11,linspace(0,1,length(S22)))';

lb=[1e6    1e8      0.0        0.0       0.0       0.0];
ub=[1e9    1e10     1500       0.333     90.0      1e12];
A0=(mean([lb',ub'],2))';

Data_Adjust=input('Are you inputting constants from previous tests? 1, yes, 0, no: ');
%input previously obtained constants
if Data_Adjust==1
   A=input('input the coefficient values acquired from previous tests: ');
else
   A=A0;
end


% options = optimset('TolX',1e-3);%('MaxFunEvals',1e9);
options=optimset('Display','iter','TolX',1e-4,'TolFun',1e-4); %Refer to help fminsearch
for this

% A=fmincon(@findtotalSSR,A0,[],[],[],[],lb,ub,[],options,E11,E22,S11,S22);
if Data_Adjust==1
   C10=A(1);
   k1=A(2);
   k2=A(3);
   kappa=A(4);
   theta=A(5);
   D=A(6);
   K=1.0/D;
%K=1.2848E+12;
   C11=2*E11+1;
   C22=2*E22+1;

   for q=1:length(E11)
```

```
    Third = 1.0/3.0;

      F11(q) = sqrt(2*E11(q)+1);
      F22(q) = sqrt(2*E22(q)+1);
      F33(q) = 1.0/(F11(q)*F22(q));
      C33(q) = F33(q)*F33(q);

      detC(q) = C11(q)*C22(q)*C33(q);
      detN13(q)=(detC(q))^(-1.0/3.0);
      TRC(q) = C11(q) + C22(q) + C33(q);
      sqrtdetC(q) = sqrt(detC(q));
      INVC11(q) = C22(q)*C33(q)/detC(q);
      INVC22(q) = C11(q)*C33(q)/detC(q);

%     detC(q)=C11(q)*C22(q);
%     INVC11(q)=C22(q)/detC(q);
%     INVC22(q)=C11(q)/detC(q);
%     TRC(q)=C11(q)+C22(q);

      NThirdTRC(q)=TRC(q)/(-3.0);
      NThirdLamda2(q)=(-
1.0/3.0)*(cosd(theta)*cosd(theta)*C11(q)+sind(theta)*sind(theta)*C22(q));
      I1(q)=detN13(q)*TRC(q);
      I4(q)=detN13(q)*(cosd(theta)*cosd(theta)*C11(q)+sind(theta)*sind(theta)*C22(q));
      EAlpha(q)=kappa*(I1(q)-3)+(1-3*kappa)*(I4(q)-1);

      S11m(q)=K*sqrtdetC(q)*(sqrtdetC(q)-1.0/sqrtdetC(q))*INVC11(q) +
2*C10*detN13(q)*(NThirdTRC(q)*INVC11(q)+1)+2*k1*exp(k2*EAlpha(q)*EAlpha(q)
)*EAlpha(q)*(kappa*detN13(q)*(NThirdTRC(q)*INVC11(q)+1)+(1-
3*kappa)*detN13(q)*(NThirdLamda2(q)*INVC11(q)+cosd(theta)*cosd(theta)));
      S22m(q)=K*sqrtdetC(q)*(sqrtdetC(q)-1.0/sqrtdetC(q))*INVC22(q) +
2*C10*detN13(q)*(NThirdTRC(q)*INVC22(q)+1)+2*k1*exp(k2*EAlpha(q)*EAlpha(q)
)*EAlpha(q)*(kappa*detN13(q)*(NThirdTRC(q)*INVC22(q)+1)+(1-
3*kappa)*detN13(q)*(NThirdLamda2(q)*INVC22(q)+sind(theta)*sind(theta)));

   end

SSR1= sum((S11m - S11).^2);
SSR2= sum((S22m - S22).^2);

else
   % A=fminsearch(@findtotalSSR,A0,[],E11,E22,S11,S22);
   [A,fval,exitflag,output]=fminsearchbnd(@findtotalSSRHolzapfel,A,lb,ub,options);
```

```
   %Data_Adjust=input('Are you inputting constants from SigmaStat? 1, yes, 0, no: ');
end

%Adjust Data if necessary
% if Data_Adjust==1
%    A=A0;
%    A=input('input the coefficient values acquired from sigma stat: ');
% else
%    A=A;
% end

%cd(filepath) %change directory for file saving

% to calculate R2
SS=[S11;S22];
SSm=[S11m;S22m];
R2=rsquare(SS,SSm)
```

Create Comparison plot for Axial Data fit

```
figure(1)

%Generate y_mesh to be used for plotting surface
% y_mesh=linspace(0,1.05.*max(Data_Structure{1,1}.E(:,1)),20)';
%Plot original axial data as 3-D line plot
L= [min(Data_Structure{1,1}.E(:,2)) max(Data_Structure{1,1}.E(:,2))];
l=diff(L)/50; %circumferential
m=Data_Structure{1,1}.E(length(Data_Structure{1,1}.E(:,1)),1)/50; %axial
[J,F] =
meshgrid(min(Data_Structure{1,1}.E(:,2)):l:max(Data_Structure{1,1}.E(:,2)),0:m:Data_
Structure{1,1}.E(length(Data_Structure{1,1}.E(:,1)),1));

j_mesh=J; %circumferential
k_mesh=F; %axial

Saa_eq_surf_fit=zeros(size(j_mesh));

for i=1:length(j_mesh(:,1))
   for q=1:length(j_mesh(:,1))

      Third = 1.0/3.0;

      F11(q) = sqrt(2*E11(q)+1);
```

```
        F22(q) = sqrt(2*E22(q)+1);
        F33(q) = 1.0/(F11(q)*F22(q));
        C33(q) = F33(q)*F33(q);

        detC(q) = C11(q)*C22(q)*C33(q);
        detN13(q)=(detC(q))^(-1.0/3.0);
        TRC(q) = C11(q) + C22(q) + C33(q);
        sqrtdetC(q) = sqrt(detC(q));
        INVC11(q) = C22(q)*C33(q)/detC(q);
        INVC22(q) = C11(q)*C33(q)/detC(q);

%     detC(q)=C11(q)*C22(q);
%     INVC11(q)=C22(q)/detC(q);
%     INVC22(q)=C11(q)/detC(q);
%     TRC(q)=C11(q)+C22(q);

        NThirdTRC(q)=TRC(q)/(-3.0);
        NThirdLamda2(q)=(-
1.0/3.0)*(cosd(theta)*cosd(theta)*C11(q)+sind(theta)*sind(theta)*C22(q));
        I1(q)=detN13(q)*TRC(q);
        I4(q)=detN13(q)*(cosd(theta)*cosd(theta)*C11(q)+sind(theta)*sind(theta)*C22(q));
        EAlpha(q)=kappa*(I1(q)-3)+(1-3*kappa)*(I4(q)-1);

        S11m_mesh(q)=K*sqrtdetC(q)*(sqrtdetC(q)-1.0/sqrtdetC(q))*INVC11(q) +
2*C10*detN13(q)*(NThirdTRC(q)*INVC11(q)+1)+2*k1*exp(k2*EAlpha(q)*EAlpha(q)
)*EAlpha(q)*(kappa*detN13(q)*(NThirdTRC(q)*INVC11(q)+1)+(1-
3*kappa)*detN13(q)*(NThirdLamda2(q)*INVC11(q)+cosd(theta)*cosd(theta)));
      % S22m_mesh(q)=K*sqrtdetC(q)*(sqrtdetC(q)-1.0/sqrtdetC(q))*INVC22(q) +
2*C10*detN13(q)*(NThirdTRC(q)*INVC22(q)+1)+2*k1*exp(k2*EAlpha(q)*EAlpha(q)
)*EAlpha(q)*(kappa*detN13(q)*(NThirdTRC(q)*INVC22(q)+1)+(1-
3*kappa)*detN13(q)*(NThirdLamda2(q)*INVC22(q)+sind(theta)*sind(theta)));

%     Q=A(1,2).*k2_mesh(i,n).^2+A(1,3).*j2_mesh(i,n).^2+
2*A(1,4).*k2_mesh(i,n).*j2_mesh(i,n);
%     S11_eq=A(1,1).*(A(1,2).*k2_mesh(i,n)+A(1,4).*j2_mesh(i,n)).*exp(Q);
%
%     Saa_eq_surf(i,:)=S11_eq;
%     S11m=S11m;


  Saa_eq_surf_fit(q,i)=S11m_mesh(q);
    end
end
```

```
%Smooth the surfaces
Saa_eq_surf_smooth=zeros(size(j_mesh));
for i=1:length(j_mesh(:,1))

    Saa_eq_surf_smooth(:,i)= smooth(Saa_eq_surf_fit(:,i));

end
surf(j_mesh,k_mesh,Saa_eq_surf_smooth)
hold on
plot3(Data_Structure{1,1}.E(:,2),Data_Structure{1,1}.E(:,1),Data_Structure{1,1}.S(:,1),'
bo')
% x=[];
% y=[];
% Saa_eq_surf=[];
% Scc_eq_surf=[];
% for i=1:no_test_ax
%     Ecc_Point=zeros(length(axial_test{1,i}.Axial_new_stress(:,1)),1);
%     Ecc_Point(:,1)=x1_mesh(i);
%
%
plot3(Ecc_Point(:,1),axial_test{1,i}.Axial_new_strain(:,1),axial_test{1,i}.Axial_new_stre
ss(:,1),'ob')
%     hold on
%     x=[x Ecc_Point(:,1)];
%      y=[y axial_test{1,i}.Axial_new_strain(:,1)];
%      S_eq=Fung_eq(A,[],[y(:,i) x(:,i)]);
%      Saa_eq_surf(:,i)=S_eq(:,1);
%      Scc_eq_surf(:,i)=S_eq(:,2);
% end
% surf(x,y,Saa_eq_surf)

ylabel('E_z_z','FontSize',14),xlabel('E_\theta_\theta','FontSize',14),zlabel('S_z_z','FontSiz
e',14)
xlim([-0.1 .5]),ylim([0 .5]),zlim([0 1e6])
grid on
h = figure(1);
saveas(h,strcat(filename,'_Axial.fig'),'fig')
```

Plot circ data

```
figure(2)
```

```
%Plot original axial data as 3-D line plot
L2= [min(Data_Structure{1,2}.E(:,1)) max(Data_Structure{1,2}.E(:,1))];
l2=diff(L2)/50; %circumferential
m2=Data_Structure{1,1}.E(length(Data_Structure{1,2}.E(:,1)),1)/50; %circumferential
[J2,K2] =
meshgrid(min(Data_Structure{1,2}.E(:,1)):l2:max(Data_Structure{1,2}.E(:,1)),0:m2:Dat
a_Structure{1,2}.E(length(Data_Structure{1,2}.E(:,1)),1));

j2_mesh=J2; %circumferential
k2_mesh=K2; %axial

Saa_eq_surf2=zeros(size(j2_mesh));

for i=1:length(j_mesh(:,1))
   for q=1:length(j_mesh(:,1))

      Third = 1.0/3.0;

      F11(q) = sqrt(2*E11(q)+1);
      F22(q) = sqrt(2*E22(q)+1);
      F33(q) = 1.0/(F11(q)*F22(q));
      C33(q) = F33(q)*F33(q);

      detC(q) = C11(q)*C22(q)*C33(q);
      detN13(q)=(detC(q))^(-1.0/3.0);
      TRC(q) = C11(q) + C22(q) + C33(q);
      sqrtdetC(q) = sqrt(detC(q));
      INVC11(q) = C22(q)*C33(q)/detC(q);
      INVC22(q) = C11(q)*C33(q)/detC(q);

%     detC(q)=C11(q)*C22(q);
%     INVC11(q)=C22(q)/detC(q);
%     INVC22(q)=C11(q)/detC(q);
%     TRC(q)=C11(q)+C22(q);

      NThirdTRC(q)=TRC(q)/(-3.0);
      NThirdLamda2(q)=(-
1.0/3.0)*(cosd(theta)*cosd(theta)*C11(q)+sind(theta)*sind(theta)*C22(q));
      I1(q)=detN13(q)*TRC(q);
      I4(q)=detN13(q)*(cosd(theta)*cosd(theta)*C11(q)+sind(theta)*sind(theta)*C22(q));
      EAlpha(q)=kappa*(I1(q)-3)+(1-3*kappa)*(I4(q)-1);
```

```
      %S11m_mesh(q)=K*sqrtdetC(q)*(sqrtdetC(q)-1.0/sqrtdetC(q))*INVC11(q) +
2*C10*detN13(q)*(NThirdTRC(q)*INVC11(q)+1)+2*k1*exp(k2*EAlpha(q)*EAlpha(q)
)*EAlpha(q)*(kappa*detN13(q)*(NThirdTRC(q)*INVC11(q)+1)+(1-
3*kappa)*detN13(q)*(NThirdLamda2(q)*INVC11(q)+cosd(theta)*cosd(theta)));
       S22m_mesh(q)=K*sqrtdetC(q)*(sqrtdetC(q)-1.0/sqrtdetC(q))*INVC22(q) +
2*C10*detN13(q)*...

(NThirdTRC(q)*INVC22(q)+1)+2*k1*exp(k2*EAlpha(q)*EAlpha(q))*EAlpha(q)*...
          (kappa*detN13(q)*(NThirdTRC(q)*INVC22(q)+1)+(1-3*kappa)*detN13(q)*...
          (NThirdLamda2(q)*INVC22(q)+sind(theta)*sind(theta)));

%     Q=A(1,2).*k2_mesh(i,n).^2+A(1,3).*j2_mesh(i,n).^2+
2*A(1,4).*k2_mesh(i,n).*j2_mesh(i,n);
%     S11_eq=A(1,1).*(A(1,2).*k2_mesh(i,n)+A(1,4).*j2_mesh(i,n)).*exp(Q);
%
%     Saa_eq_surf(i,:)=S11_eq;
%     S11m=S11m;


  Saa_eq_surf2(q,i)=-S22m_mesh(q);
    end
end

%Smooth the surfaces
Saa_eq_surf_smooth2=zeros(size(j_mesh));
for i=1:length(j_mesh(:,1))

       Saa_eq_surf_smooth2(:,i)= smooth(Saa_eq_surf2(:,i));

end
% for i=1:length(j2_mesh(:,1))
%     for n=1:length(j2_mesh(:,1))
%
%    S22m=S22m;
%
%     Saa_eq_surf2(i,n)=-S22m(i);
%     end
% end
surf(j2_mesh,k2_mesh,Saa_eq_surf_smooth2)
hold on
%
plot3(Data_Structure{1,1}.E(:,2),Data_Structure{1,1}.E(:,1),Data_Structure{1,1}.S(:,1),'
bo')
```

```
% d=max(Data_Structure{1,2}.E(:,1))/50; %axial
% f=max(Data_Structure{1,2}.E(:,2))/50; %circumferential
% [X,Y] =
meshgrid(0:f:max(Data_Structure{1,2}.E(:,2)),0:d:max(Data_Structure{1,2}.E(:,1)));
% %d=Data_Structure{1,2}.E(length(Data_Structure{1,2}.E(:,1)),1)/50; %axial
% %f=Data_Structure{1,2}.E(length(Data_Structure{1,2}.E(:,1)),2)/50;
%circumferential
% %[X,Y] =
meshgrid(0:f:Data_Structure{1,2}.E(length(Data_Structure{1,2}.E(:,1)),2),0:d:Data_Stru
cture{1,2}.E(length(Data_Structure{1,2}.E(:,1)),1));
%
% x_mesh=X; %circumferential
% y_mesh=Y; %axial
%
% Scc_eq_surf=zeros(size(x_mesh));
%
%
%S22_eq2=A(1,1)*(A(1,3).*x_mesh+A(1,4).*y_mesh)*exp(A(1,2).*y_mesh.^2+A(1,3).
*x_mesh.^2+ 2*A(1,4).*y_mesh.*x_mesh);
%
% for i=1:length(x_mesh(:,1))
%    for n=1:length(x_mesh(:,1))
% %     Q=A(1,2).*y_mesh(i,:).^2+A(1,3).*x_mesh(i,:).^2+
2*A(1,4).*y_mesh(i,:).*x_mesh(i,:);
% %     S22_eq=A(1,1).*(A(1,3).*x_mesh(i,:)+A(1,4).*y_mesh(i,:)).*exp(Q);
% %     S_eq=findtotalSSR(A,[],x_mesh(i,:),y_mesh(i,:),S11,S22)
% %     S_eq=Fung_eq(A,[],[x_mesh(i,:)' y_mesh(i,:)']);
%     S22m=S22m';
%
%     Scc_eq_surf(i,n)=S22m(i);
%    end
%
% end
% surf(y_mesh,x_mesh,Scc_eq_surf)
% hold on
plot3(Data_Structure{1,2}.E(:,1),Data_Structure{1,2}.E(:,2),Data_Structure{1,2}.S(:,2),'
bo')
xlabel('E_z_z','FontSize',14),ylabel('E_\theta_\theta','FontSize',14),zlabel('S_\theta_\theta'
,'FontSize',14)
xlim([0 .5]),ylim([-0.1 .5]),zlim([0 1e5])
grid on
h = figure(2);
```

```
saveas(h,strcat(filename,'_Circ.fig'),'fig')
```

Compute Axial and Circ Stiffnesses

```
S11_Epeak = Data_Structure{1,1}.E(length(Data_Structure{1,1}.E),:);

S22_Epeak = Data_Structure{1,2}.E(length(Data_Structure{1,2}.E),:);

Axial_Stiffness = A(1,1) * (A(1,2)*S11_Epeak(1,1) + A(1,4)*S11_Epeak(1,2)) *
(2*A(1,2)*S11_Epeak(1,1) + 2*A(1,4)*S11_Epeak(1,2))...
   *exp(A(1,2)*S11_Epeak(1,1)^2 + A(1,3)*S11_Epeak(1,2)^2 +
2*A(1,4)*S11_Epeak(1,1)*S11_Epeak(1,2))...
   +(A(1,1)*A(1,2))*exp(A(1,2)*S11_Epeak(1,1)^2 + A(1,3)*S11_Epeak(1,2)^2 +
2*A(1,4)*S11_Epeak(1,1)*S11_Epeak(1,2));
Circ_Stiffness = A(1,1) * (A(1,3)*S22_Epeak(1,2) + A(1,4)*S22_Epeak(1,1)) *
(2*A(1,3)*S22_Epeak(1,2) + 2*A(1,4)*S22_Epeak(1,1))...
   *exp(A(1,2)*S22_Epeak(1,1)^2 + A(1,3)*S22_Epeak(1,2)^2 +
2*A(1,4)*S22_Epeak(1,1)*S22_Epeak(1,2))...
   +(A(1,1)*A(1,3))*exp(A(1,2)*S22_Epeak(1,1)^2 + A(1,3)*S22_Epeak(1,2)^2 +
2*A(1,4)*S22_Epeak(1,1)*S22_Epeak(1,2));
Peak_Axial_Strain = S11_Epeak(1,1);
Peak_Circ_Strain = S22_Epeak(1,2);

S_Peak_Axial_fit=A(1,1)*(A(1,2)*y_mesh(51,51)+A(1,4)*x_mesh(51,51))*(2*A(1,2)*y
_mesh(51,51)+A(1,4)*x_mesh(51,51))*exp(A(1,2)*y_mesh(51,51)^2+A(1,3)*x_mesh(5
1,51)^2+ 2*A(1,4)*y_mesh(51,51)*x_mesh(51,51));
S_Peak_Circ_fit=A(1,1)*(A(1,3)*x_mesh(51,51)+A(1,4)*y_mesh(51,51))*(2*A(1,3)*x_
mesh(51,51)+A(1,4)*y_mesh(51,51))*exp(A(1,2)*y_mesh(51,51)^2+A(1,3)*x_mesh(51,
51)^2+ 2*A(1,4)*y_mesh(51,51)*x_mesh(51,51));


% Axial_Stiffness =
A(1,1)*(A(1,2)*Data_Structure{1,1}.E(length(Data_Structure{1,1}.E),1)+A(1,4)*Data_
Structure{1,1}.E(length(Data_Structure{1,1}.E),2))*(2*A(1,2)*Data_Structure{1,1}.E(le
ngth(Data_Structure{1,1}.E),1) ...
%
+2*A(1,4)*Data_Structure{1,1}.E(length(Data_Structure{1,1}.E),2))*exp(A(1,2)*Data_
Structure{1,1}.E(length(Data_Structure{1,1}.E),1)^2 +
A(1,3)*Data_Structure{1,1}.E(length(Data_Structure{1,1}.E),2)^2 ...
%          +
2*A(1,4)*Data_Structure{1,1}.E(length(Data_Structure{1,1}.E),1)*Data_Structure{1,1}.
E(length(Data_Structure{1,1}.E),2));
```

```
% Circ_Stiffness =
A(1,1)*(A(1,3)*max(E22)+A(1,4)*max(E11))*(2*A(1,3)*max(E22)+2*A(1,4)*max(E11
))*exp(A(1,2)*max(E11)^2 + A(1,3)*max(E22)^2 + 2*A(1,4)*max(E11)*max(E22));

save (filename)Published with MATLAB® R2015a
```

Coefficient_Read_Write_D

Pathname:

```
%Coefficient Reader for Hozafel Parameters
%Greg Johnson
%10-19-2009

clc
clear all
close all

%save original cd to variable base_cd for use later on
base_cd=cd;

%Specify worksheet to load
worksheet=input('Enter Worksheet to load: ','s');

%Load Excel File
[exceldata exceltext]=xlsread('Final material parameters.xls',worksheet);

%Retrieve important data points to be used in analysis
Emax=exceldata(:,12:13);
S=exceldata(:,17);
Coefficients=exceldata(:,19:24);

C10=Coefficients(:,1).*1e-6;
K1=Coefficients(:,2).*1e-6;
K2=Coefficients(:,3);
k=Coefficients(:,4);
theta=Coefficients(:,5);
K=Coefficients(:,6);
n=length(S);
%Retrieve sample and specimen strings from excel file
Specimens={};
Samples={};
Specimens(:,1)=exceltext(2:n+1,2);
Samples(:,1)=exceltext(2:n+1,3);

E11eq=zeros(n,1);
E22eq=zeros(n,1);
IM11=zeros(n,1);
IM22=zeros(n,1);
S11eq=zeros(n,1);
```

```
S22eq=zeros(n,1);
%Find underscores in Samples to be used later
u=strfind(Samples,'_');

%Change directory to biaxial data folders
cd 'Y:\Darren Haskett\AHA BGIA 08 09\Biaxial Testing'
%Store root cd to be used
root_cd=cd;

R2a=zeros(n,1);R2b=zeros(n,1);
R2=zeros(n,1); %#ok<NASGU>
%Begin loop of Biax_Post_Processing
for Sample=1:n
    adjusted_u=cell2mat(u(Sample));
    Specimen_temp=cell2mat(Specimens(Sample));
    Sample_temp=cell2mat(Samples(Sample));
    if length(adjusted_u)>3
        Sample_Label=Sample_temp(adjusted_u(length(adjusted_u)-
2)+1:length(Sample_temp));
    else
        Sample_Label=Sample_temp(adjusted_u(length(adjusted_u)-
1)+1:length(Sample_temp));
    end
    cd([root_cd,'\',Specimen_temp,'\',Sample_temp])

%%%%%%%%%%%%%%%%%%%%%%%%%%%%%%%%%%%%%%%%%%%%%%%%%%%%%%%%%%%%%%%%%%%%%%%
%
    %%%%%%%%%%%%%%%%%%%%%%%%%%%%Begin Biax_Post_Processing
Code%%%%%%%%%%%%%%%%%%%%%%%%%%%%
    %Biax Data Analysis
    %Created by Greg Johnson
    %8/8/08

    %Enter specimen information
    Sample_Name=Sample_Label;
    String_Label=[Sample_Name '_'];
    %Imputs data from files into a 3 dimensional array

    Data=[];
    Data(:,:)=importdata([String_Label '120_120Nm\' String_Label '120_120Nm_10
.bx']);
```

```
    %sets size of Strain matrix as well as zeros out first page of matrix
    Strain=zeros(size(Data(:,2:3)));
    Load_Cyclex=0;
    Load_Cycley=0;

        %Sets parameters to be used in While loop to default values
        j=1;
        Increasing=1;
        while Increasing>0      %While loop determines ending y load time
            Increasing=Data(j+1,9)-Data(j,9);   %Determines if load on cells is increasing
            Load_Cyclex=Load_Cyclex+1;        %#ok<AGROW> %Increments the place
holder for end of Loading data
            j=j+1;
            if j<15      %Prevents early stopping of Determining Load Time
              Increasing=1;
            end
        end


    Data(:,9:10)=Data(:,9:10)./1000;

    %Obtain strain values from stretch data

    Strain(:,1)=.5.*(Data(:,2).^2-1); %#ok<AGROW>
    Strain(:,2)=.5.*(Data(:,3).^2-1); %#ok<AGROW>

    %zero out Stress and Strain data

    if Data(8,2)-Data(1,2)<0
        Strain(:,1)=Strain(:,1)-Strain(1,1);
    elseif Data(8,2)-Data(1,2)>0
        Strain(:,1)=Strain(:,1)-min(Strain(1:Load_Cyclex,1));
    end
    Data(:,9)=Data(:,9)-min(Data(1:Load_Cyclex,9));

    if Data(8,3)-Data(1,3)<0
        Strain(:,2)=Strain(:,2)-Strain(1,2); %#ok<AGROW>
    elseif Data(8,3)-Data(1,3)>0
        Strain(:,2)=Strain(:,2)-min(Strain(1:Load_Cyclex,2)); %#ok<AGROW>
    end
    Data(:,10)=Data(:,10)-min(Data(1:Load_Cyclex,10)); %#ok<AGROW>

    figure(Sample)
```

```
    plot(Strain(1:Load_Cyclex,1),Data(1:Load_Cyclex,9),'or','MarkerFaceColor','r')
    xlabel('E','Fontsize',16),ylabel('S (kPa)','Fontsize',16)
    hold on
    plot(Strain(1:Load_Cyclex,2),Data(1:Load_Cyclex,10),'ob','MarkerFaceColor','w')
    hold on
    legend('\theta','L','Location','SE')
    axis([-.04 .4 0 140])


    %%%%%%%%%%%%%%%%%%%%%%%%%%%%%%End
Biax_Post_Processing Code%%%%%%%%%%%%%%%%%%%%%%

%%%%%%%%%%%%%%%%%%%%%%%%%%%%%%%%%%%%%%%%%%%
%%%%%%%%%%%%%%%%%%%%%%%%%%%%%%%%%%%%%%

        E11=Data(1:Load_Cyclex,2);
        E11=(E11(:,1).^2-1);
        E22=Data(1:Load_Cyclex,3);
        E22=(E22(:,1).^2-1);
        S11=Data(1:Load_Cyclex,9);
        S22=Data(1:Load_Cyclex,10);


    [S11m S22m]=fit_fun_D([],E11,E22,[],[],...
        C10(Sample),K1(Sample),K2(Sample),k(Sample),theta(Sample),K(Sample));

    if max(S11m)>S(Sample)

        E11log=E11(S11m<S(Sample));

    %Use linear interpolation of data to find appropriate strains in E11
        E11eq(Sample)=((E11(length(E11log)+1)-E11(length(E11log)))/...
                (S11m(length(E11log)+1)-S11m(length(E11log))))*...
                (S(Sample)-S11m(length(E11log)))+E11(length(E11log));
    end
    if max(S22m)>S(Sample)

        E22log=E22(S22m<S(Sample));

    %Use linear interpolation of data to find appropriate strains in E22
        E22eq(Sample)=((E22(length(E22log)+1)-E22(length(E22log)))/...
                 (S22m(length(E22log)+1)-S22m(length(E22log))))*...
                 (S(Sample)-S22m(length(E22log)))+E22(length(E22log));
```

```
    end
    %Determine Incremental Modulus
    if E11eq(Sample)~=0&&E22eq(Sample)~=0

        %Determine IM11 and IM22 from averaged slope
        IM11(Sample)=(S11m(length(E11log)+1)-S11m(length(E11log)-1))/...
                (E11(length(E11log)+1)-E11(length(E11log)-1));
        IM22(Sample)=(S22m(length(E22log)+1)-S22m(length(E22log)-1))/...
                (E22(length(E22log)+1)-E22(length(E22log)-1));

        [S11eq S22eq]=fit_fun_D([],E11eq(Sample),E22eq(Sample),[],[],...
           C10(Sample),K1(Sample),K2(Sample),k(Sample),theta(Sample),K(Sample));

        %l_poly11=zeros(1,2);
        %l_poly11(1)=IM11(Sample);
        %l_poly11(2)=S11eq-IM11(Sample)*E11eq(Sample);
        %poly11=polyval(l_poly11,[E11(length(E11log)-1) E11eq(Sample)
E11(length(E11log)+1)]);

        %l_poly22=zeros(1,2);
        %l_poly22(1)=IM22(Sample);
        %l_poly22(2)=S22eq-IM22(Sample)*E22eq(Sample);
        %poly22=polyval(l_poly22,[E22(length(E22log)-1) E22eq(Sample)
E22(length(E22log)+1)]);

        hold on
        plot(E11,S11m,'r--',E22,S22m,'b--')
        %plot([E11(length(E11log)-1) E11eq(Sample) E11(length(E11log)+1)],poly11,'k-
',...
        %    [E22(length(E22log)-1) E22eq(Sample) E22(length(E22log)+1)],poly22,'k-')
        axis([-.04 .4 0 140])
        saveas(gcf,'EquiBiax_Fit.jpg')
    else
        hold on
        plot(E11,S11m,'r-',E22,S22m,'b-')
        axis([-.04 .4 0 140])
    end

    SSR=sum((S11m-S11).^2)+sum((S22m-S22).^2);
    SST=sum((S11-mean(S11)).^2)+sum((S22-mean(S22)).^2);
%    R2(Sample)=1-SSR/SST;
    R2a(Sample) = 1 - (sum((S11m-S11).^2))/(sum((S11-mean(S11)).^2));
    R2b(Sample) = 1 - (sum((S22m-S22).^2))/(sum((S22-mean(S22)).^2));
```

```
   clear Data Strain S11m S22m
end
R2=[R2a R2b];
cd(base_cd)
%Preallocate sizes of final matrixes


%for i=1:length(S)
%    E11=linspace(0,.4,400);
%    E22=linspace(0,.4,400);

%    [S11m S22m]=fit_fun_D([],E11,E22,[],[],C10(i),K1(i),K2(i),k(i),theta(i),K(i));

    %Change to appropriate scale for S11m and S22m
%    E11log=E11(S22m<S(i));
%    E22log=E22(S22m<S(i));

   %Use linear interpolation of data to find appropriate strains in E11
%    E11eq(i)=((E11(length(E11log)+1)-E11(length(E11log)))/...
%            (S11m(length(E11log)+1)-S11m(length(E11log))))*...
%            (S(i)-S11m(length(E11log)))+E11(length(E11log));

   %Use linear interpolation of data to find appropriate strains in E22
%   E22eq(i)=((E22(length(E22log)+1)-E22(length(E22log)))/...
%           (S22m(length(E22log)+1)-S22m(length(E22log))))*...
%           (S(i)-S22m(length(E22log)))+E11(length(E22log));

   %Determine Incrimental Modulus
%   IM11(i)=(S11m(length(E11log)+5)-S11m(length(E11log)-5))/...
%       (E11(length(E11log)+5)-E11(length(E11log)-5));
%   IM22(i)=(S22m(length(E22log)+5)-S22m(length(E22log)-5))/...
%       (E22(length(E22log)+5)-E22(length(E22log)-5));
   %Plot fit data along with experimental data

%   figure(i)
%   hold on
%   plot(E11,S11m,'r-',E22,S22m,'b-')
%   axis([-.04 .4 0 140])

%   clear E11 E22 E11log S11m S22m
%end
```

```
ESdata=zeros(n+3,4);
%Compile data into 1 variable
ESdata(1:n,:)=[IM11 IM22 E11eq E22eq];
%Compute mean of data
for i=1:4
   ESdata(n+1,i)=mean(nonzeros(ESdata(1:n,i)));
   %Compute Standard Error of Data
   ESdata(n+2,i)=std(nonzeros(ESdata(1:n,i)))/sqrt(length(nonzeros(ESdata(1:n,i))));
   %Determine new n value for statistics
   ESdata(n+3,i)=length(nonzeros(ESdata(1:n,i)));
end
Bargraph_data=ESdata(n+1:n+3,:)';

%Use Transpose to make copying and pasteing easier
%ESdata=ESdata';
```

Published with MATLAB® R2015a

findtotalSSRHolzapfel

Pathname:

```
function totalSSR=findtotalSSRHolzapfel(a,x,y)%,E11,E22,S11,S22)
global E11 E22 S11 S22
global S11m S22m
%a = A0;
%C1=a(1);a1=a(2);a2=a(3);a12=a(4);
% Q=a1.*E11.^2+a2.*E22.^2+ 2*a12.*E11.*E22;
%
% S11_eq=C1.*(a1.*E11+a12.*E22).*exp(Q);
% S22_eq=C1.*(a2.*E22+a12.*E11).*exp(Q);

%If coupled fitting does not produce acceptable fits, comment out Q and
%stress equations and uncomment the uncoupled equations below

%S11_eq=C1.*((a1.*E11).*exp(0.5*a1.*E11.^2)+(a12.*E22).*exp(a12.*(E11.*E22)));
%S22_eq=C1.*((a2.*E22).*exp(0.5*a2.*E22.^2)+(a12.*E11).*exp(a12.*(E11.*E22)));

C10=a(1);
k1=a(2);
k2=a(3);
kappa=a(4);
theta=a(5);
D=a(6);
K=1.0/D;
%K=1.2848E+12;
IAGUI

C11=2*E11+1;
C22=2*E22+1;

for q=1:length(E11)
    Third = 1.0/3.0;

    F11(q) = sqrt(2*E11(q)+1);
    F22(q) = sqrt(2*E22(q)+1);
    F33(q) = 1.0/(F11(q)*F22(q));
    C33(q) = F33(q)*F33(q);

    detC(q) = C11(q)*C22(q)*C33(q);
    detN13(q)=(detC(q))^(-1.0/3.0);
    TRC(q) = C11(q) + C22(q) + C33(q);
    sqrtdetC(q) = sqrt(detC(q));
```

```
    INVC11(q) = C22(q)*C33(q)/detC(q);
    INVC22(q) = C11(q)*C33(q)/detC(q);

%     detC(q)=C11(q)*C22(q);
%     INVC11(q)=C22(q)/detC(q);
%     INVC22(q)=C11(q)/detC(q);
%     TRC(q)=C11(q)+C22(q);

    NThirdTRC(q)=TRC(q)/(-3.0);
    NThirdLamda2(q)=(-
1.0/3.0)*(cosd(theta)*cosd(theta)*C11(q)+sind(theta)*sind(theta)*C22(q));
    I1(q)=detN13(q)*TRC(q);
    I4(q)=detN13(q)*(cosd(theta)*cosd(theta)*C11(q)+sind(theta)*sind(theta)*C22(q));
    EAlpha(q)=kappa*(I1(q)-3)+(1-3*kappa)*(I4(q)-1);

    S11m(q)=K*sqrtdetC(q)*(sqrtdetC(q)-1.0/sqrtdetC(q))*INVC11(q) +
2*C10*detN13(q)*(NThirdTRC(q)*INVC11(q)+1)+2*k1*exp(k2*EAlpha(q)*EAlpha(q)
)*EAlpha(q)*(kappa*detN13(q)*(NThirdTRC(q)*INVC11(q)+1)+(1-
3*kappa)*detN13(q)*(NThirdLamda2(q)*INVC11(q)+cosd(theta)*cosd(theta)));
    S22m(q)=K*sqrtdetC(q)*(sqrtdetC(q)-1.0/sqrtdetC(q))*INVC22(q) +
2*C10*detN13(q)*(NThirdTRC(q)*INVC22(q)+1)+2*k1*exp(k2*EAlpha(q)*EAlpha(q)
)*EAlpha(q)*(kappa*detN13(q)*(NThirdTRC(q)*INVC22(q)+1)+(1-
3*kappa)*detN13(q)*(NThirdLamda2(q)*INVC22(q)+sind(theta)*sind(theta)));

end

SSR1= sum((S11m' - S11).^2);
SSR2= sum((S22m' - S22).^2);

global totalSSR %#ok<REDEF>

totalSSR=SSR1+SSR2;

end
```

Published with MATLAB® R2015a

fit_power_model_for_microbiax_mouse_data

Pathname:

```
function [calib_p,calib_obj] = fit_power_model_for_microbiax_mouse_data()
clear all
close all
clc

num_index=0;
%Let user select desired data to load and read
data = matfile(uigetfile('.mat','Select data to be fitted'));
E11 = data.E11;
S11 = data.S11;
E22 = data.E22;
S22 = data.S22;

E11m = linspace(min(E11),max(E11),length(E11));
E11m = E11m.';
E22m = linspace(min(E22),max(E22),length(E22));
E22m = E22m.';
% S11m = interp1(linspace(0,1,length(S11)),S11,linspace(0,1,length(S22)));
% S11m = S11m.';
% S22m = interp1(linspace(0,1,length(S11)),S11,linspace(0,1,length(S22)));
% S22m = S22m.';

curr_dir = pwd;

cd(curr_dir);


% no_test_circ= input('Input the number of Circ Pressure Tests: ');
% Data_Structure=cell(1,2);
%
% If data has not already been previously further post processed with E11/22 and S11/22
defined
% then uncomment the next section and derive the values for 2PK and Green strains
%
% %%  Create S and E matrices based off of Axial tests
%
% %Define empty E and S data storage matrices
% %aa-axial
% %cc-circumferential
%
% Eaa_Dat=[];
```

```
% Ecc_Dat=[];
% Saa_Dat=[];
% Scc_Dat=[];
%
% %Define x_mesh vector to be utilized in later surface plotting
% %x1_mesh=zeros(1,no_test_ax);
% %Read and Define various stress-strain values based upon input data loaded
% %at begining of program
% for i=1:no_test_circ
%     %Construct vector of Eaa, Saa data points for fitting with fixed Ecc
%     Eaa_Dat=[Eaa_Dat;axial_test{1,i}.Axial_new_strain(:,1)];
%#ok<*AGROW>
%
%     Saa_temp=axial_test{1,i}.Axial_new_stress(:,1)./(1 +
2*(axial_test{1,i}.Axial_new_strain(:,1)));
%     Saa_Dat=[Saa_Dat;Saa_temp];
%
%     Ecc_Point=zeros(length(axial_test{1,i}.Axial_new_stress(:,1)),1);
%     Ecc_Point(:,1)=axial_test{1,i}.Circ_Strain_Point;
%     Ecc_Dat=[Ecc_Dat;Ecc_Point];
%     %x1_mesh(i)=axial_test{1,i}.Circ_Strain_Point(:);
%
% %     axial_test{1,i}.pressure=axial_test{1,i}.data2(axial_test{1,i}.loc(:));
%#ok<*SAGROW>
% %     axial_test{1,i}.pressure(:)=133.28.*abs(axial_test{1,i}.pressure(:));
%#ok<SAGROW>
% %     Scc_temp=(axial_test{1,i}.pressure.*(axial_test{1,i}.Axial_outer_radius.*1e3-
axial_test{1,i}.Axial_thickness)./axial_test{1,i}.Axial_thickness)./(1 +
2*(axial_test{1,i}.Circ_Strain_Point));
%      Scc_temp=axial_test{1,i}.Axial_new_stress;
%
%     if length(Scc_temp)~=length(axial_test{:,i}.Axial_new_stress(:,1))
%         Scc_temp=Scc_temp(1:length(axial_test{:,i}.Axial_new_stress(:,1)),1);
%     end
%     Scc_Dat=[Scc_Dat;Scc_temp];
% end
% %Store aa and cc data into data structure for organizational purposes
% Data_Structure{1,1}.S=[Saa_Dat Scc_Dat];
% Data_Structure{1,1}.E=[Eaa_Dat Ecc_Dat];
%
% %% Create S and E matrices based off of Circ tests
%
% %To be completed once method of obtained Axial Stress from Circumferential
```

```
% %data sets is determined
%
% Eaa_Dat=[];
% Ecc_Dat=[];
% Saa_Dat=[];
% Scc_Dat=[];
%
% for i=1:no_test_circ
%     %Construct vectors for Ecc, Saa, Scc, for fixed Eaa
%     Ecc_Dat=[Ecc_Dat;circ_test{1,i}.new_circ_strain];
%
%     Scc_temp=circ_test{1,i}.new_circ_stress./(1 + 2*(circ_test{1,i}.new_circ_strain));
%     Scc_Dat=[Scc_Dat;Scc_temp];
%
%     Eaa_Point=zeros(length(circ_test{1,i}.new_circ_strain),1);
%     Eaa_Point(:,1)=circ_test{1,i}.Axial_Strain_Point;
%     Eaa_Dat=[Eaa_Dat;Eaa_Point];
%
%     if length(circ_test{:,i}.Axial_Stress)~=length(circ_test{:,i}.new_circ_strain)
%
circ_test{1,i}.Axial_Stress=circ_test{:,i}.Axial_Stress(1:length(circ_test{1,i}.new_circ_s
train),1);
%     end
%     Saa_temp=circ_test{1,i}.Axial_Stress./(1 + 2*(circ_test{1,i}.Axial_Strain_Point));
%     Saa_Dat=[Saa_Dat;Saa_temp];
%
% end
%
% Data_Structure{1,2}.S=[Saa_Dat Scc_Dat];
% Data_Structure{1,2}.E=[Eaa_Dat Ecc_Dat];
%
% E11=Data_Structure{1,2}.E(:,2); %Circumferential
% E22=Data_Structure{1,1}.E(:,1); %Axial
% S11=Data_Structure{1,2}.S(:,2); %Circumferential
% S22=Data_Structure{1,1}.S(:,1); %Axial


%%For fitting it is important to have good initial guesses so if possible
%%use previously obtained constants other wise some best initial guesses
%%will be used instead


Data_Adjust=input('Are you inputting constants from previous tests? 1, yes, 0, no: ');
```

```
%input previously obtained constants
if Data_Adjust==1
   x0 = input('input the coefficient values acquired from previous tests: ');
else
   x0 =
[1.79E+07          5.00E+08          3.939827724       0.100905549       38.43873606
          4.97E+10];
end

% LastResults(:,:)=FittingResults(:,:);


   lb=[1e6    1e8      0.0        0.0       0.0];
   ub=[1e9    1e10     1500       0.333     90.0];

   %     OptPt = LastResults(counter_specimen,2:8)
%          SampleRegionLB = 0.8*OptPt;
%          SampleRegionLB = SampleRegionLB.';
%          nn=20;
%          RandMatrix = rand(nn,7);
%          x0(1,:) = OptPt;

% %looking for the initial range
%    lb=[1e6     1e8       0.001      0.0     40.0];
%    ub=[1e8     1e10      1000       0.5     50.0];
%    nn=50;
%    RandMatrix = rand(nn,5);
%    for i = 1 : nn
%      x0(i, :) = lb + RandMatrix(i,:).*(ub-lb);
%    end


   [n,m] = size(x0);
   xx = zeros(n,m);
   options = optimset('MaxFunEvals',1e9);
% from each starting point, find corresponding optimum
   for j = 1:n %Should it be m
      clear x fval exitflag
      [x,fval,exitflag] = fmincon(@fit_obj_D,x0(j,:),[],[],[],[], ...
                          lb,ub,[],options,E11,E22,S11,S22);
      xx(j,:) = x;
      yy(j) = fval;
   end
```

```
% find global optimum from a set of local optimums
   index = find(yy==min(yy));
% calibrated model parameters P and corresponding objective function
   calib_p = xx(index(1),:)
   calib_obj = yy(index(1))

% to calculate R2
[S11m, S22m] = fit_fun_D(calib_p,E11,E22,S11,S22);
R2 = 1 - (sum((S11m-S11).^2) + sum((S22m-S22).^2))/(sum((S11-mean(S11)).^2) +
sum((S22-mean(S22)).^2))
% to plot smooth curves
[S11m, S22m] = fit_fun_D(calib_p,E11m,E22m,S11,S22);
%save FittingResults S11m S22m

% %2D, single protocol
% plot(E11,S11,'ro',E22,S22,'bo');
% plot(E11,S11m,'r-',E22,S22m,'b-','LineWidth',2);

% %2D, mutilple protocols
num_index=0;
hold on;
for i = 1 : length(data)
%     data=load(FILENAME);
%     Stress11=data(:,9);
%     Stress22=data(:,10);
%     lamda1=data(:,2);
%     lamda2=data(:,3);
%     [maxvalue,index1]=max(Stress11);
%     [maxvalue,index2]=max(Stress22);
%     index=min(index1, index2);
   figure(1);
   plot(E11((1):(index)),S11((1):(index)),'ro');
   plot(E11m((1):(index)),S11m((1):(index)),'r-','LineWidth',2);
   xlabel('E_1_1');
   ylabel('S_1_1');
   hold on;
   figure(2);
   plot(E22((1):(index)),S22((1):(index)),'bo');
   hold on;
   plot(E22m((1):(index)),S22m((1):(index)),'b-','LineWidth',2);
   xlabel('E_2_2');
   ylabel('S_2_2');
```

```
   num_index=index;
end

  %Smoothing done to data to produce cleaner graphical representations of
    %fitted results
%     if((E11(1+num_index) == 0)&& (E11(num_index+index) < 0) )
%
E11m((1+num_index):(num_index+index))=linspace(max(E11((1+num_index):(num_in
dex+index))), min(E11((1+num_index):(num_index+index))),index);
%     else
%
E11m((1+num_index):(num_index+index))=linspace(min(E11((1+num_index):(num_ind
ex+index))), max(E11((1+num_index):(num_index+index))),index);
%     end
%
%     if((E22(1+num_index) == 0)&& (E22(num_index+index) < 0) )
%
E22m((1+num_index):(num_index+index))=linspace(max(E22((1+num_index):(num_in
dex+index))), min(E22((1+num_index):(num_index+index))),index);
%     else
%
E22m((1+num_index):(num_index+index))=linspace(min(E22((1+num_index):(num_ind
ex+index))), max(E22((1+num_index):(num_index+index))),index);
%     end
%
%
%     num_index=num_index+index;
```

Published with MATLAB® R2015a

fit_fun_D

Pathname:

```
% the function to be calibrated ------------------------ user defined
 % here x represents model parameters P

function [S11m, S22m] =fit_fun_D(x,E11,E22,S11,S22)
C10=x(1);
k1=x(2);
k2=x(3);
kappa=x(4);
theta=x(5);
D=x(6);
K=1.0/D;
%K=1.2848E+12;

C11=2*E11+1;
C22=2*E22+1;

for q=1:length(E11)
   Third = 1.0/3.0;

   F11(q) = sqrt(2*E11(q)+1);
   F22(q) = sqrt(2*E22(q)+1);
   F33(q) = 1.0/(F11(q)*F22(q));
   C33(q) = F33(q)*F33(q);

   detC(q) = C11(q)*C22(q)*C33(q);
   detN13(q)=(detC(q))^(-1.0/3.0);
   TRC(q) = C11(q) + C22(q) + C33(q);
   sqrtdetC(q) = sqrt(detC(q));
   INVC11(q) = C22(q)*C33(q)/detC(q);
   INVC22(q) = C11(q)*C33(q)/detC(q);

%    detC(q)=C11(q)*C22(q);
%    INVC11(q)=C22(q)/detC(q);
%    INVC22(q)=C11(q)/detC(q);
%    TRC(q)=C11(q)+C22(q);

   NThirdTRC(q)=TRC(q)/(-3.0);
   NThirdLamda2(q)=(-
1.0/3.0)*(cosd(theta)*cosd(theta)*C11(q)+sind(theta)*sind(theta)*C22(q));
   I1(q)=detN13(q)*TRC(q);
   I4(q)=detN13(q)*(cosd(theta)*cosd(theta)*C11(q)+sind(theta)*sind(theta)*C22(q));
```

```
    EAlpha(q)=kappa*(I1(q)-3)+(1-3*kappa)*(I4(q)-1);

    S11m(q)=K*sqrtdetC(q)*(sqrtdetC(q)-1.0/sqrtdetC(q))*INVC11(q) +
2*C10*detN13(q)*(NThirdTRC(q)*INVC11(q)+1)+2*k1*exp(k2*EAlpha(q)*EAlpha(q)
)*EAlpha(q)*(kappa*detN13(q)*(NThirdTRC(q)*INVC11(q)+1)+(1-
3*kappa)*detN13(q)*(NThirdLamda2(q)*INVC11(q)+cosd(theta)*cosd(theta)));
    S22m(q)=K*sqrtdetC(q)*(sqrtdetC(q)-1.0/sqrtdetC(q))*INVC22(q) +
2*C10*detN13(q)*(NThirdTRC(q)*INVC22(q)+1)+2*k1*exp(k2*EAlpha(q)*EAlpha(q)
)*EAlpha(q)*(kappa*detN13(q)*(NThirdTRC(q)*INVC22(q)+1)+(1-
3*kappa)*detN13(q)*(NThirdLamda2(q)*INVC22(q)+sind(theta)*sind(theta)));

end

S11m = S11m.';
S22m = S22m.';

end
```

Published with MATLAB® R2015a

fit_obj_D

Pathname:

```
function y = fit_obj_D(x,E11,E22,S11,S22,S11m,S22m)

[S11m, S22m] = fit_fun_D(x,E11,E22,S11,S22);
% % % objective function -- least square
y1=sum((S11m-S11).^2)/(mean(S11).^2);
y2=sum((S22m-S22).^2)/(mean(S22).^2);

y=y1+y2;
```

Published with MATLAB® R2015a

Fminsearchbnd

Pathname:

```
function [x,fval,exitflag,output]=fminsearchbnd(fun,x0,LB,UB,options,varargin)
% FMINSEARCHBNDNEW: FMINSEARCH, but with bound constraints by
transformation
%
% Changes from fminsearchbnd:
% 1) in options structure, user may pass an 'output function' and 'plot function' to
fminsearch.
% Original fminsearchbnd handled the output function via a nested wrapper function.  I
have extended
% this to the plot function too.
% 2) I have moved the 'intrafun' and 'xtransform' functions and wrappers to be nested
functions
% (INSIDE the fminsearchbnd function), so they do not need to pass the params structure
around
% (into fminsearch) - but have access to it directly.  This maintains the integrity of the
varargin,
% which the user may be passing thru fminsearch to their optmization funciton
(fminsearchbnd had
% passed the params structure to fminsearch, thus ruining any varargin that the user
passed in).
% This also obviates the params.(whatever) structure the author had, so I've eliminated it
so things
% are simpler.
% 3) I have created a test example so the user can see not only how fminseachbnd works,
but also how
% the OutputFn and PrintFns functions work, which were heretofore poorly documented
by MathWorks.
% Many thanks to the original author, John D'Errico, for excellent work - very useful!
%
%   Modifications by: Ken Purchase
%             Email: kpurchase at yahoo
%              Date: 2007-Nov-29
%
%
% usage: x=FMINSEARCHBND(fun,x0)
% usage: x=FMINSEARCHBND(fun,x0,LB)
% usage: x=FMINSEARCHBND(fun,x0,LB,UB)
% usage: x=FMINSEARCHBND(fun,x0,LB,UB,options)
% usage: x=FMINSEARCHBND(fun,x0,LB,UB,options,p1,p2,...)
% usage: [x,fval,exitflag,output]=FMINSEARCHBND(fun,x0,...)
%
```

```
% arguments:
%  fun, x0, options - see the help for FMINSEARCH
%
%  LB - lower bound vector or array, must be the same size as x0
%
%       If no lower bounds exist for one of the variables, then
%       supply -inf for that variable.
%
%       If no lower bounds at all, then LB may be left empty.
%
%       Variables may be fixed in value by setting the corresponding
%       lower and upper bounds to exactly the same value.
%
%  UB - upper bound vector or array, must be the same size as x0
%
%       If no upper bounds exist for one of the variables, then
%       supply +inf for that variable.
%
%       If no upper bounds at all, then UB may be left empty.
%
%       Variables may be fixed in value by setting the corresponding
%       lower and upper bounds to exactly the same value.
%
% Notes:
%
%  If options is supplied, then TolX will apply to the transformed
%  variables. All other FMINSEARCH parameters should be unaffected.
%
%  Variables which are constrained by both a lower and an upper
%  bound will use a sin transformation. Those constrained by
%  only a lower or an upper bound will use a quadratic
%  transformation, and unconstrained variables will be left alone.
%
%  Variables may be fixed by setting their respective bounds equal.
%  In this case, the problem will be reduced in size for FMINSEARCH.
%
%  The bounds are inclusive inequalities, which admit the
%  boundary values themselves, but will not permit ANY function
%  evaluations outside the bounds. These constraints are strictly
%  followed.
%
%  If your problem has an EXCLUSIVE (strict) constraint which will
%  not admit evaluation at the bound itself, then you must provide
```

```
%  a slightly offset bound. An example of this is a function which
%  contains the log of one of its parameters. If you constrain the
%  variable to have a lower bound of zero, then FMINSEARCHBND may
%  try to evaluate the function exactly at zero.
%
%
% Example:
% rosen = @(x) (1-x(1)).^2 + 105*(x(2)-x(1).^2).^2;
%
% fminsearch(rosen,[3 3])     % unconstrained
% ans =
%    1.0000    1.0000
%
% fminsearchbnd(rosen,[3 3],[2 2],[])     % constrained
% ans =
%    2.0000    4.0000
%
% See test_main.m for other examples of use.
%
%
% See also: fminsearch, fminspleas
%
%
% Author: John D'Errico
% E-mail: woodchips@rochester.rr.com
% Release: 4
% Release date: 7/23/06

% size checks
xsize = size(x0);
x0 = x0(:);
xLength=length(x0);

if (nargin<3) || isempty(LB)
  LB = repmat(-inf,xLength,1);
else
  LB = LB(:);
end
if (nargin<4) || isempty(UB)
  UB = repmat(inf,xLength,1);
else
  UB = UB(:);
end
```

```
if (xLength~=length(LB)) || (xLength~=length(UB))
  error 'x0 is incompatible in size with either LB or UB.'
end

% set default options if necessary
if (nargin<5) || isempty(options)
  options = optimset('fminsearch');
end


% 0 --> unconstrained variable
% 1 --> lower bound only
% 2 --> upper bound only
% 3 --> dual finite bounds
% 4 --> fixed variable
BoundClass = zeros(xLength,1);
for i=1:xLength
  k = isfinite(LB(i)) + 2*isfinite(UB(i));
  BoundClass(i) = k;
  if (k==3) && (LB(i)==UB(i))
    BoundClass(i) = 4;
  end
end

% transform starting values into their unconstrained
% surrogates. Check for infeasible starting guesses.
x0u = x0;
k=1;
for i = 1:xLength
  switch BoundClass(i)
    case 1
      % lower bound only
      if x0(i)<=LB(i)
        % infeasible starting value. Use bound.
        x0u(k) = 0;
      else
        x0u(k) = sqrt(x0(i) - LB(i));
      end

      % increment k
      k=k+1;
    case 2
```

```
    % upper bound only
    if x0(i)>=UB(i)
      % infeasible starting value. use bound.
      x0u(k) = 0;
    else
      x0u(k) = sqrt(UB(i) - x0(i));
    end

    % increment k
    k=k+1;
  case 3
    % lower and upper bounds
    if x0(i)<=LB(i)
      % infeasible starting value
      x0u(k) = -pi/2;
    elseif x0(i)>=UB(i)
      % infeasible starting value
      x0u(k) = pi/2;
    else
      x0u(k) = 2*(x0(i) - LB(i))/(UB(i)-LB(i)) - 1;
      % shift by 2*pi to avoid problems at zero in fminsearch
      % otherwise, the initial simplex is vanishingly small
      x0u(k) = 2*pi+asin(max(-1,min(1,x0u(k))));
    end

    % increment k
    k=k+1;
  case 0
    % unconstrained variable. x0u(i) is set.
    x0u(k) = x0(i);

    % increment k
    k=k+1;
  case 4
    % fixed variable. drop it before fminsearch sees it.
    % k is not incremented for this variable.
  end

end
% if any of the unknowns were fixed, then we need to shorten
% x0u now.
if k<=xLength
  x0u(k:xLength) = [];
```

```
end

% were all the variables fixed?
if isempty(x0u)
  % All variables were fixed. quit immediately, setting the
  % appropriate parameters, then return.

  % undo the variable transformations into the original space
  x = xtransform(x0u);

  % final reshape
  x = reshape(x,xsize);

  % stuff fval with the final value
  fval = feval(fun,x,varargin);
  keyboard;
  % fminsearchbnd was not called
  exitflag = 0;

  output.iterations = 0;
  output.funcount = 1;
  output.algorithm = 'no call (all variables fixed)';
  output.message = 'All variables were held fixed by the applied bounds';

  % return with no call at all to fminsearch
  return
end


% Add the wrapper function to the user function right here inline:
    intrafun = @(x, varargin) fun(xtransform(x), varargin{:});

% Added code:  Add wrappers to output function(s) and plot function(s) - you can
specify multiple
% output and/or print functions if you use a cell array of function handles.
    if ~isempty(options)
        % Add a wrapper to the output function(s)
        % fetch the output function and put it(them) into a cell array:
        OutputFcn =
createCellArrayOfFunctions(optimget(options,'OutputFcn',struct('OutputFcn',[]),'fast'),'O
utputFcn');
        for ii = 1:length(OutputFcn)
            %stop = firstOutputFunction(OutStructure, optimValues, state, varargin)
```

```
        OutputFcn{ii} = @(x, varargin) OutputFcn{ii}(xtransform(x), varargin{:});
      end
      % store the "wrapped" output function back into the options.
      options = optimset(options, 'OutputFcn', OutputFcn);

      % Add a wrapper to the plot function(s)
      % fetch the plot function and put it(them) into a cell array:
      PlotFcn =
createCellArrayOfFunctions(optimget(options,'PlotFcns',struct('PlotFcns',[]),'fast'),'PlotF
cns');
      for ii = 1:length(PlotFcn)
        %stop = firstOutputFunction(OutStructure, optimValues, state, varargin)
        PlotFcn{ii} = @(x, varargin) PlotFcn{ii}(xtransform(x), varargin{:});
      end
      % store the "wrapped" output function back into the options.
      options = optimset(options, 'PlotFcns', PlotFcn);
      % Add a wrapper to the print function(s)
   end



% now we can call fminsearch, but with our own
% intra-objective function.
%   keyboard;
[xu,fval,exitflag,output] = fminsearch(intrafun,x0u,options,varargin);
output.algorithm = [output.algorithm ' bounded using fminsearchbnd'];

% undo the variable transformations into the original space
x = xtransform(xu);

% final reshape
x = reshape(x,xsize);


   % ===================================
   % ========= begin NESTED subfunctions =========
   % ===================================
      function xtrans = xtransform(x)
      % converts unconstrained variables into their original domains

      xtrans = zeros(xsize); %zeros(xLength, 1);   % I changed this to make it same
dimension as the x in fminsearch
                             % was zeros(1, params.xLength)
```

```
    % k allows some variables to be fixed, thus dropped from the
    % optimization.
    k=1;
    for i = 1:xLength
      switch BoundClass(i)
        case 1
          % lower bound only
          xtrans(i) = LB(i) + x(k).^2;

          k=k+1;
        case 2
          % upper bound only
          xtrans(i) = UB(i) - x(k).^2;

          k=k+1;
        case 3
          % lower and upper bounds
          xtrans(i) = (sin(x(k))+1)/2;
          xtrans(i) = xtrans(i)*(UB(i) - LB(i)) + LB(i);
          % just in case of any floating point problems
          xtrans(i) = max(LB(i),min(UB(i),xtrans(i)));

          k=k+1;
        case 4
          % fixed variable, bounds are equal, set it at either bound
          xtrans(i) = LB(i);
        case 0
          % unconstrained variable.
          xtrans(i) = x(k);

          k=k+1;
      end
    end

    end % sub function xtransform end



end % mainline end
```

Published with MATLAB® R2015a

APPENDIX E: SIGMASTAT CODE

SigmaFit

Pathname:

```
jsv4D
[Parameters]
C1=100000
a1=1
a2=0.1
a12=0.00001

[Variables]
Dir=col(1)
S=col(4)
E11=col(2)
E22=col(3)

[Equation]
Stress=if(Dir=1,eqn1(E11,E22),eqn2(E11,E22))
eqn1(E11,E22)=C1*(a1*E11+a12*E22)*exp(a1*E11^2+a2*E22^2+2*a12*E11*E22)
eqn2(E11,E22)=C1*(a2*E22+a12*E11)*exp(a1*E11^2+a2*E22^2+2*a12*E11*E22)
Fit Stress to S


[Constraints]
C1>0
a1>0
a2>0
a12>0

[Options]
```

SigmaFit uncoupled

Pathname:

```
jsv4D
[Parameters]
C1=100000
a1=1
a2=0.1
a12=0.00001

[Variables]
Dir=col(1)
S=col(4)
E11=col(2)
E22=col(3)

[Equation]
Stress=if(Dir=1,eqn1(E11,E22),eqn2(E11,E22))
eqn1(E11,E22)=C1*((a1*E11)*exp(0.5*a1*E11^2)+(a12*E22)*exp(a12*(E11*E22)))
eqn2(E11,E22)=C1*((a2*E22)*exp(0.5*a2*E22^2)+(a12*E11)*exp(a12*(E11*E22)))
Fit Stress to S


[Constraints]
C1>0
a1>0
a2>0
a12>0

[Options]
```

sigmaFit holzapfel

Pathname:

```
jsv4D
[Parameters]
C10=100000
k1=1
k2=0.1
kappa=
theta=
K=

[Variables]
Dir=col(1)
S=col(4)
E11=col(2)
E22=col(3)

[Equation]
Stress=if(Dir=1,eqn1(E11,E22),eqn2(E11,E22))
eqn1(E11,E22)=K*sqrt((2*E11+1)*(2*E22+1)*(1/(sqrt(2*E11+1)*sqrt(2*E22+1))))*(sq
rt((2*E11+1)*(2*E22+1)*(1/(sqrt(2*E11+1)*sqrt(2*E22+1))))-
1.0/sqrt((2*E11+1)*(2*E22+1)*(1/(sqrt(2*E11+1)*sqrt(2*E22+1)))))*((2*E22+1)*(1/(s
qrt(2*E11+1)*sqrt(2*E22+1)))/sqrt((2*E11+1)*(2*E22+1)*(1/(sqrt(2*E11+1)*sqrt(2*E2
2+1)))))+2*C10*(sqrt((2*E11+1)*(2*E22+1)*(1/(sqrt(2*E11+1)*sqrt(2*E22+1))))^(-
1/3))*((((2*E11+1)+(2*E22+1)+(1/(sqrt(2*E11+1)*sqrt(2*E22+1))))/-
3)*((2*E22+1)*(1/(sqrt(2*E11+1)*sqrt(2*E22+1)))/sqrt((2*E11+1)*(2*E22+1)*(1/(sqrt(
2*E11+1)*sqrt(2*E22+1)))))+1)+2*k1*exp(k2*kappa*(((2*E11+1)*(2*E22+1)*(1/(sqrt(
2*E11+1)*sqrt(2*E22+1))))^(-
1.0/3.0)*((2*E11+1)+(2*E22+1)+(1/(sqrt(2*E11+1)*sqrt(2*E22+1))))-3)+(1-
3*kappa)*(((2*E11+1)*(2*E22+1)*(1/(sqrt(2*E11+1)*sqrt(2*E22+1))))^(-
1.0/3.0)*(cosd(theta)*cosd(theta)*C11(q)+sind(theta)*sind(theta)*(2*E22+1))-
1)*kappa*(((2*E11+1)*(2*E22+1)*(1/(sqrt(2*E11+1)*sqrt(2*E22+1))))^(-
1.0/3.0)*((2*E11+1)+(2*E22+1)+(1/(sqrt(2*E11+1)*sqrt(2*E22+1))))-3)+(1-
3*kappa)*(((2*E11+1)*(2*E22+1)*(1/(sqrt(2*E11+1)*sqrt(2*E22+1))))^(-
1.0/3.0)*(cosd(theta)*cosd(theta)*C11(q)+sind(theta)*sind(theta)*(2*E22+1))-
1))*kappa*(((2*E11+1)*(2*E22+1)*(1/(sqrt(2*E11+1)*sqrt(2*E22+1))))^(-
1.0/3.0)*((2*E11+1)+(2*E22+1)+(1/(sqrt(2*E11+1)*sqrt(2*E22+1))))-3)+(1-
3*kappa)*(((2*E11+1)*(2*E22+1)*(1/(sqrt(2*E11+1)*sqrt(2*E22+1))))^(-
1.0/3.0)*(cosd(theta)*cosd(theta)*C11(q)+sind(theta)*sind(theta)*(2*E22+1))-
1)*(kappa*((2*E11+1)*(2*E22+1)*(1/(sqrt(2*E11+1)*sqrt(2*E22+1))))^(-
1.0/3.0)*((((2*E11+1)+(2*E22+1)+(1/(sqrt(2*E11+1)*sqrt(2*E22+1))))/-
3)*((2*E22+1)*(1/(sqrt(2*E11+1)*sqrt(2*E22+1))/((2*E11+1)*(2*E22+1)*(1/(sqrt(2*E
11+1)*sqrt(2*E22+1)))))+1)+(1-
```

```
3*kappa)*((2*E11+1)*(2*E22+1)*(1/(sqrt(2*E11+1)*sqrt(2*E22+1))))^(-1.0/3.0)*((-
1.0/3.0)*(cosd(theta)*cosd(theta)*(2*E11+1)+sind(theta)*sind(theta)*(2*E22+1))*((2*E
22+1)*(1/(sqrt(2*E11+1)*sqrt(2*E22+1)))/((2*E11+1)*(2*E22+1)*(1/(sqrt(2*E11+1)*s
qrt(2*E22+1)))))+cosd(theta)*cosd(theta)))
eqn2(E11,E22)=K*sqrt((2*E11+1)*(2*E22+1)*(1/(sqrt(2*E11+1)*sqrt(2*E22+1))))*(sq
rt((2*E11+1)*(2*E22+1)*(1/(sqrt(2*E11+1)*sqrt(2*E22+1))))-
1.0/sqrt((2*E11+1)*(2*E22+1)*(1/(sqrt(2*E11+1)*sqrt(2*E22+1)))))*((2*E11+1)*(1/(s
qrt(2*E11+1)*sqrt(2*E22+1)))/sqrt((2*E11+1)*(2*E22+1)*(1/(sqrt(2*E11+1)*sqrt(2*E2
2+1)))))+2*C10*(sqrt((2*E11+1)*(2*E22+1)*(1/(sqrt(2*E11+1)*sqrt(2*E22+1))))^(-
1/3))*((((2*E11+1)+(2*E22+1)+(1/(sqrt(2*E11+1)*sqrt(2*E22+1))))/-
3)*((2*E11+1)*(1/(sqrt(2*E11+1)*sqrt(2*E22+1)))/sqrt((2*E11+1)*(2*E22+1)*(1/(sqrt(
2*E11+1)*sqrt(2*E22+1)))))+1)+2*k1*exp(k2*kappa*(((2*E11+1)*(2*E22+1)*(1/(sqrt(
2*E11+1)*sqrt(2*E22+1))))^(-
1.0/3.0)*((2*E11+1)+(2*E22+1)+(1/(sqrt(2*E11+1)*sqrt(2*E22+1))))-3)+(1-
3*kappa)*(((2*E11+1)*(2*E22+1)*(1/(sqrt(2*E11+1)*sqrt(2*E22+1))))^(-
1.0/3.0)*(cosd(theta)*cosd(theta)*C11(q)+sind(theta)*sind(theta)*(2*E22+1))-
1)*kappa*(((2*E11+1)*(2*E22+1)*(1/(sqrt(2*E11+1)*sqrt(2*E22+1))))^(-
1.0/3.0)*((2*E11+1)+(2*E22+1)+(1/(sqrt(2*E11+1)*sqrt(2*E22+1))))-3)+(1-
3*kappa)*(((2*E11+1)*(2*E22+1)*(1/(sqrt(2*E11+1)*sqrt(2*E22+1))))^(-
1.0/3.0)*(cosd(theta)*cosd(theta)*C11(q)+sind(theta)*sind(theta)*(2*E22+1))-
1))*kappa*(((2*E11+1)*(2*E22+1)*(1/(sqrt(2*E11+1)*sqrt(2*E22+1))))^(-
1.0/3.0)*((2*E11+1)+(2*E22+1)+(1/(sqrt(2*E11+1)*sqrt(2*E22+1))))-3)+(1-
3*kappa)*(((2*E11+1)*(2*E22+1)*(1/(sqrt(2*E11+1)*sqrt(2*E22+1))))^(-
1.0/3.0)*(cosd(theta)*cosd(theta)*C11(q)+sind(theta)*sind(theta)*(2*E22+1))-
1)*(kappa*((2*E11+1)*(2*E22+1)*(1/(sqrt(2*E11+1)*sqrt(2*E22+1))))^(-
1.0/3.0)*((((2*E11+1)+(2*E22+1)+(1/(sqrt(2*E11+1)*sqrt(2*E22+1))))/-
3)*((2*E11+1)*(1/(sqrt(2*E11+1)*sqrt(2*E22+1))/((2*E11+1)*(2*E22+1)*(1/(sqrt(2*E
11+1)*sqrt(2*E22+1)))))+1)+(1-
3*kappa)*((2*E11+1)*(2*E22+1)*(1/(sqrt(2*E11+1)*sqrt(2*E22+1))))^(-1.0/3.0)*((-
1.0/3.0)*(cosd(theta)*cosd(theta)*(2*E11+1)+sind(theta)*sind(theta)*(2*E22+1))*((2*E
11+1)*(1/(sqrt(2*E11+1)*sqrt(2*E22+1)))/((2*E11+1)*(2*E22+1)*(1/(sqrt(2*E11+1)*s
qrt(2*E22+1)))))+sind(theta)*sind(theta)))
Fit Stress to S


[Constraints]
C10>0
k1>0
k2>0
kappa>0
theta>0
K>0

[Options]
```

sigmaFit holzapfel 2nd try

Pathname:

```
jsv4D
[Parameters]
C10=100000
k1=100000
k2=0.001
kappa=0.00000025
theta=0.0000001
D=100


[Variables]
Dir=col(1)
S=col(4)
E11=col(2)
E22=col(3)

[Equation]
Stress=if(Dir=1,eqn1(E11,E22),eqn2(E11,E22))
K=1/D
C11=2*E11+1
C22=2*E22+1

F11 = sqrt(2*E11+1)
F22 = sqrt(2*E22+1)
F33 = 1.0/(F11*F22)
C33 = F33*F33

detC = C11*C22*C33
detN13=(detC)^(-1.0/3.0)
TRC = C11 + C22 + C33
sqrtdetC = sqrt(detC)
INVC11 = C22*C33/detC
INVC22 = C11*C33/detC

NThirdTRC=TRC/(-3.0)
NThirdLamda2=(-1.0/3.0)*(cos(theta)*cos(theta)*C11+sin(theta)*sin(theta)*C22)
I1=detN13*TRC
I4=detN13*(cos(theta)*cos(theta)*C11+sin(theta)*sin(theta)*C22)
EAlpha=kappa*(I1-3)+(1-3*kappa)*(I4-1)
```

```
eqn1(E11,E22)=K*sqrtdetC*(sqrtdetC-1.0/sqrtdetC)*INVC11 +
2*C10*detN13*(NThirdTRC*INVC11+1)+2*k1*exp(k2*EAlpha*EAlpha)*EAlpha*(ka
ppa*detN13*(NThirdTRC*INVC11+1)+(1-
3*kappa)*detN13*(NThirdLamda2*INVC11+cos(theta)*cos(theta)))
eqn2(E11,E22)=K*sqrtdetC*(sqrtdetC-1.0/sqrtdetC)*INVC22 +
2*C10*detN13*(NThirdTRC*INVC22+1)+2*k1*exp(k2*EAlpha*EAlpha)*EAlpha*(ka
ppa*detN13*(NThirdTRC*INVC22+1)+(1-
3*kappa)*detN13*(NThirdLamda2*INVC22+sin(theta)*sin(theta)))
```

Fit Stress to S

```
[Constraints]
C10<1000000000
C10>0
k1<1000000000
k1>0
k2<1000000000
k2>0
kappa<0.333
kappa>0
theta<90
theta>0
D>0

[Options]
```